Active Phase Double Crystal Monochromator for JET (Diagnostic System KS1)[+]

C. Andelfinger, J. Fink, G. Fußmann, H. Krause
H. Röhr, H.-B. Schilling, U. Schumacher

P. Becker, H. Siegert [++]

P. Abel, J. Keul [+++]

IPP 1/225 March 1984

MAX-PLANCK-INSTITUT FÜR PLASMAPHYSIK

8046 GARCHING BEI MÜNCHEN

MAX-PLANCK-INSTITUT FÜR PLASMAPHYSIK

GARCHING BEI MÜNCHEN

Active Phase Double Crystal Monochromator for JET (Diagnostic System KS1)[+]

C. Andelfinger, J. Fink, G. Fußmann, H. Krause,
H. Röhr, H.-B. Schilling, U. Schumacher

P. Becker, H. Siegert [++]

P. Abel, J. Keul [+++]

IPP 1/225 March 1984

[+] This work was done under Contract No. JE 2/9017
"Detailed Design of the Broadband X-Ray Crystal Diagnostic System for JET"

[++] Physikalisch-Technische Bundesanstalt
3300 Braunschweig

[+++] Arthur Pfeiffer Vakuumtechnik Wetzlar GmbH
6334 Asslar

Die nachstehende Arbeit wurde im Rahmen des Vertrages zwischen dem Max-Planck-Institut für Plasmaphysik und der Europäischen Atomgemeinschaft über die Zusammenarbeit auf dem Gebiete der Plasmaphysik durchgeführt.

IPP 1/225

C. Andelfinger, J. Fink,
G. Fußmann, H. Krause,
H. Röhr, H.-B. Schilling,
U. Schumacher

P. Becker, H. Siegert

P. Abel, J. Keul

Active Phase Double Crystal Monochromator for JET (Diagnostic System KS1)

Abstract

The determination of the impurity concentrations in JET plasmas by absolute radiation measurements in a wide spectral range can be done with a double crystal monochromator device in parallel mode, which is able to operate during all experimental phases of JET. The report describes the engineering design and tests for a double crystal monochromator that fulfills the conditions of parallel orientation of the two crystals during fast wavelength scan, of shielding against neutrons and gamma rays by its folded optical pathway and of sufficient spectral resolution for line profile measurements.

Contents

1. Introduction

One of the most important physics problems in present magnetic confinement experiments is the plasma impurity behaviour. The determination of the concentrations and the transport of impurities in high-temperature plasmas is an important task of plasma diagnostics and contributes much to the understanding of the plasma behaviour and the radiation losses.

Since at high electron temperatures as in JET plasmas most of the radiation is emitted in the soft X-ray region it is aimed at diagnosing the impurities by their appropriate X-ray spectral lines.

The main goal of the soft X-ray monochromator is to determine the main impurity concentrations of the JET plasma by absolute radiation measurements in a wide spectral range to be scanned during a time interval short compared to the plasma lifetime (discharge time). The monochromator should be able to operate during all experimental phases of JET, hence also during the D-T operation (the "active phase") of JET with its high neutron and gamma fluxes. Further information of this monochromator might be gained from spectral line ratio and profile measurements for electron and ion temperature determination.

The present report treats the basic properties of the broadband soft X-ray monochromator in section 2, followed by the discussion of the components of the monochromator and results of component tests in section 3, while section 4 presents the engineering design of the device.

Because of the similarity of this active phase double crystal monochromator (JET Diagnostic System KS1) with the spatial scan double crystal monochromator (JET Diagnostic System KS2) some sections are similar (but specifically different) to those in IPP/226.

2. Basic Properties of the Broadband Soft X-Ray Monochromator

2.1 Spectral Range and Crystal Choice

The choice of the spectral range is influenced by the plasma parameters and the main impurities of interest. We roughly expect three groups of impurities:

1) The ubiquitous elements as oxygen, nitrogen, carbon or iron, which are mostly low-Z impurities;
2) the constituents of the wall material (INCONEL 600), which are predominantly nickel, chromium, iron and - at very low concentrations - carbon, manganese, sulfur, silicon and copper with mainly intermediate Z and
3) those elements as neon or argon that might be purposely added into the JET plasma as tracer elements for plasma diagnostics.

The fractional abundances f_z of the charge states of the main INCONEL constituents chromium, iron, and nickel as functions of the electron temperature T_e for coronal equilibrium as calculated by C. Breton et al. /1/ are given in Fig. 1, those for oxygen and the possibly added elements neon and argon in Fig. 2.

These graphs are examples of the charge state distributions of some of the impurity elements to be expected. They indicate that for the plasma centre at electron temperatures of several keV the low-Z impurities are completely ionized while for the medium-Z impurities hydrogen-, helium-, lithium- or beryllium-like transitions are to be expected. The plasma boundary region with its lower temperature is dominated by lower charge state transitions.

Most of these transitions belong to spectral lines in the wavelength region of about 1 Å to about 25 Å, which is accessible by crystal spectroscopy as, e.g., proposed in the broadband crystal spectrometer design study for JET /3/. The figures 3 to 5 give examples of the relation of several typical spectral lines that are expected to be emitted from intermediate and high electron temperature plasmas of JET. Fig. 3 illustrates that the most prominent hydrogen- and helium-like lines of oxygen and many spectral lines of lower charge-state

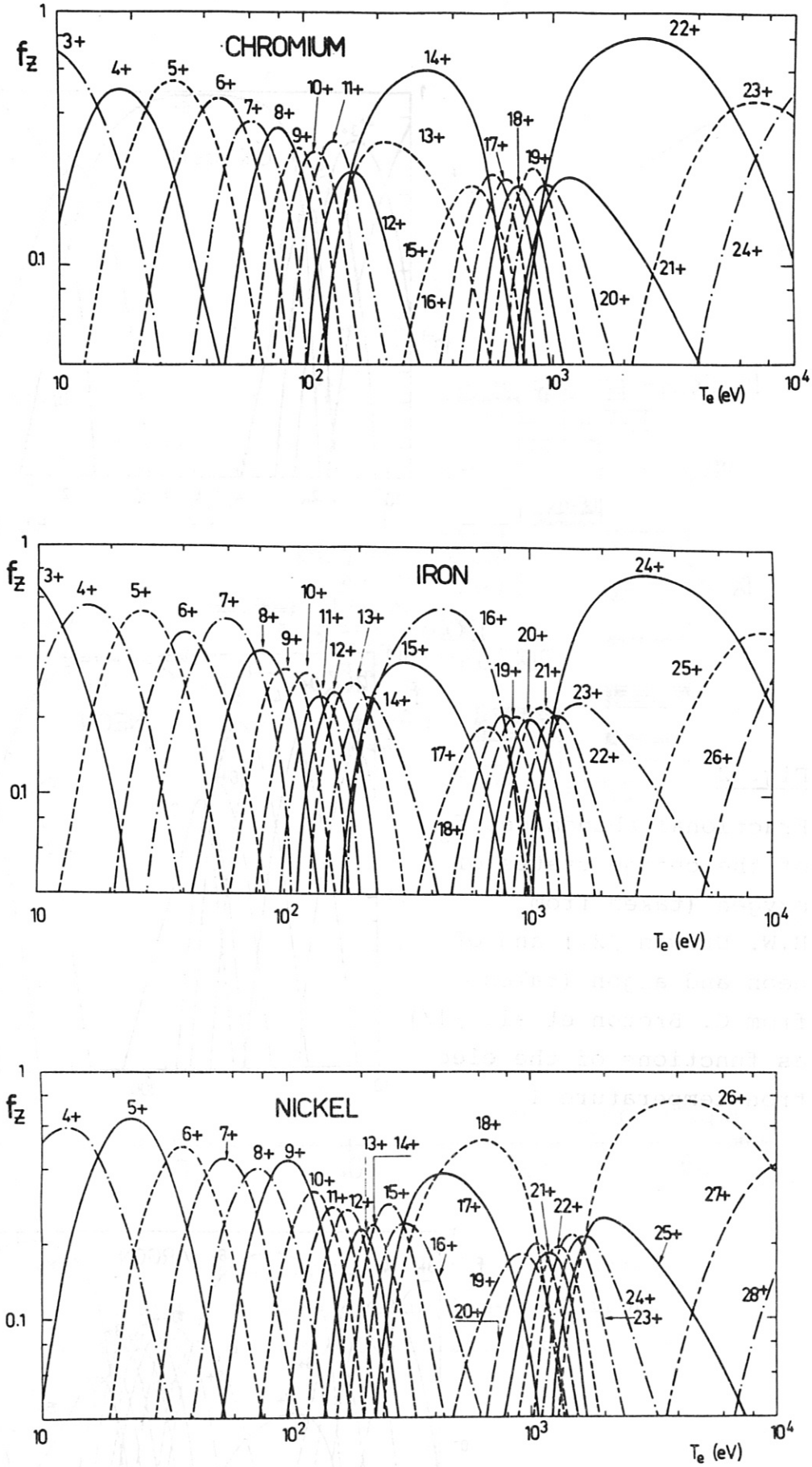

Fig. 1 Fractional abundances f_z of the charge states of chromium, iron, and nickel as functions of the electron temperature T_e (taken from C. Breton et al. /1/)

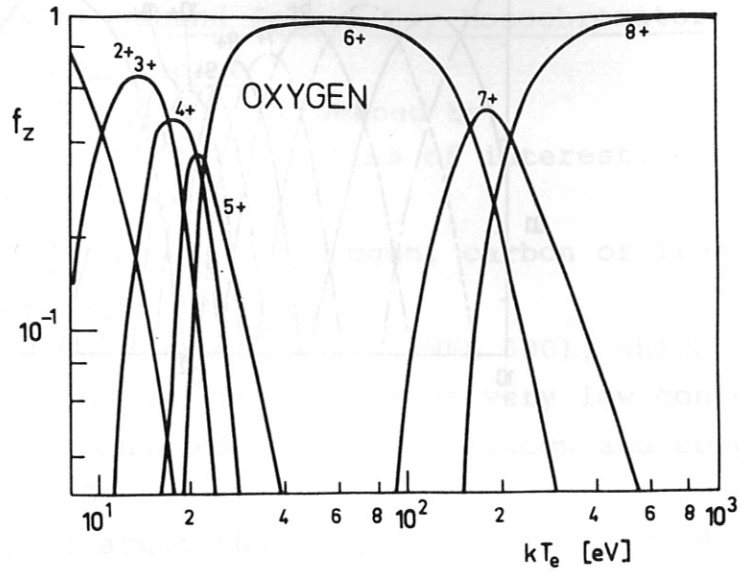

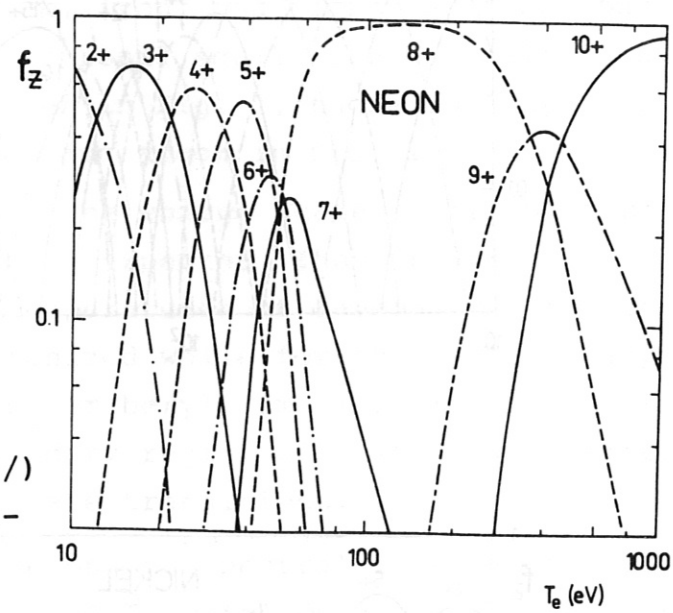

Fig. 2

Fractional abundances f_z of the charge states of oxygen (taken from H.W. Drawin /2/) and of neon and argon (taken from C. Breton et al. /1/) as functions of the electron temperature T_e

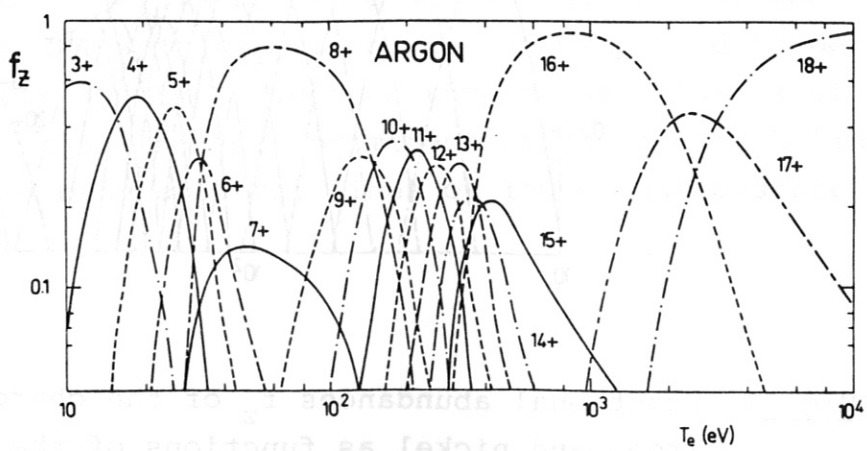

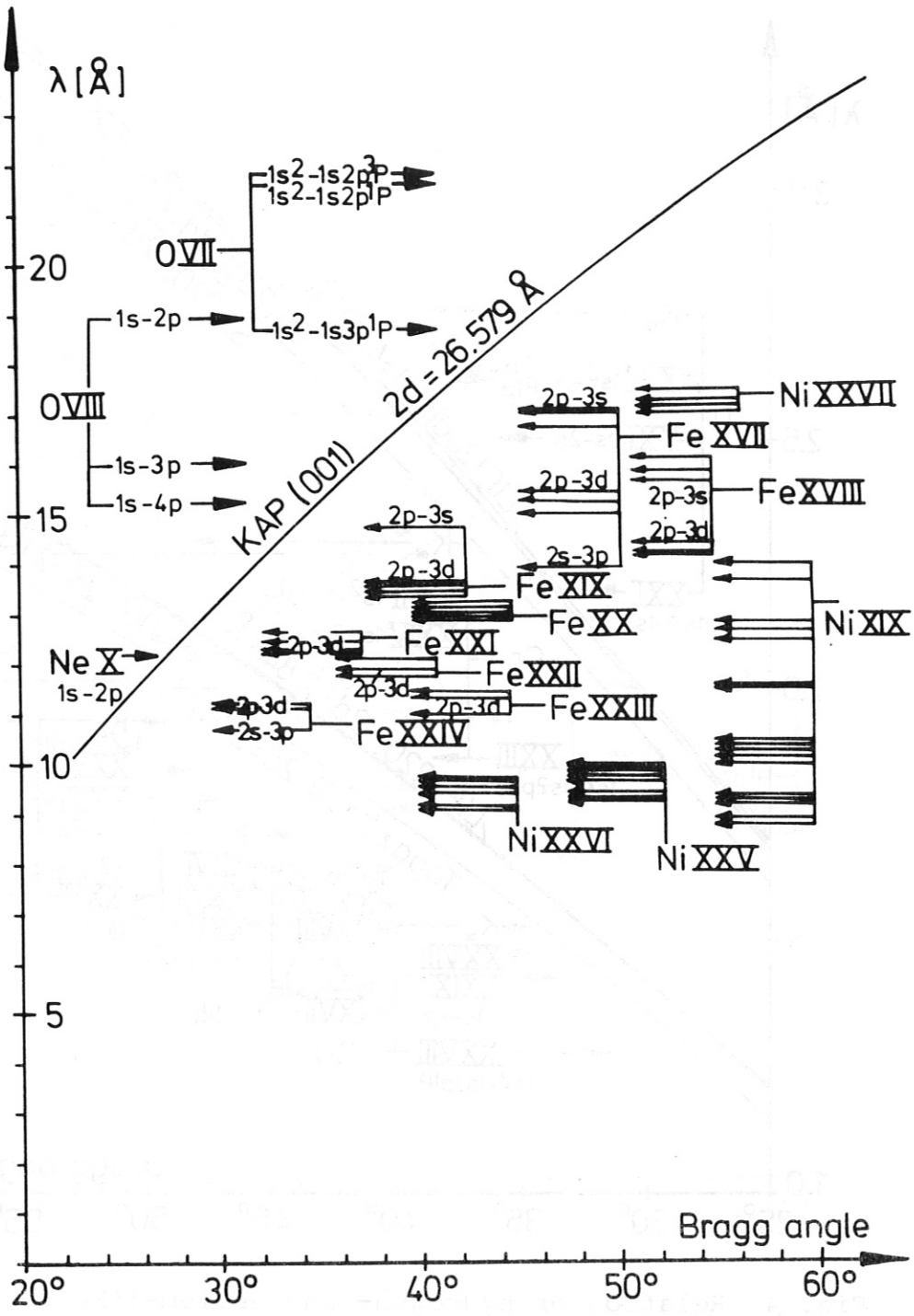

Fig. 3 Wavelength-Bragg angle relation for some oxygen and some L-spectrum lines of iron and nickel for KAP (001) first order reflection

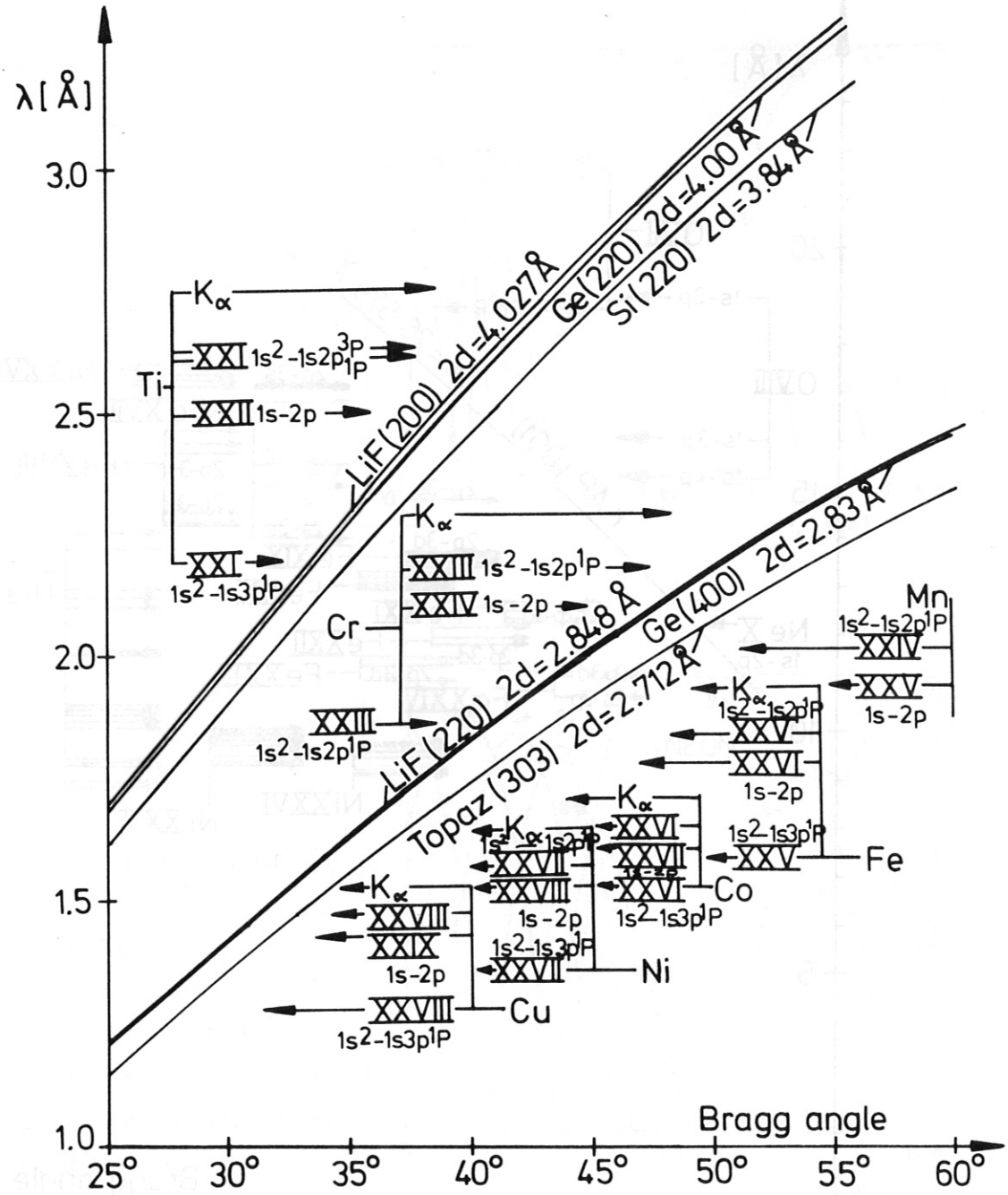

Fig. 4 Relation of hydrogen- and helium-like transitions to the Bragg angle

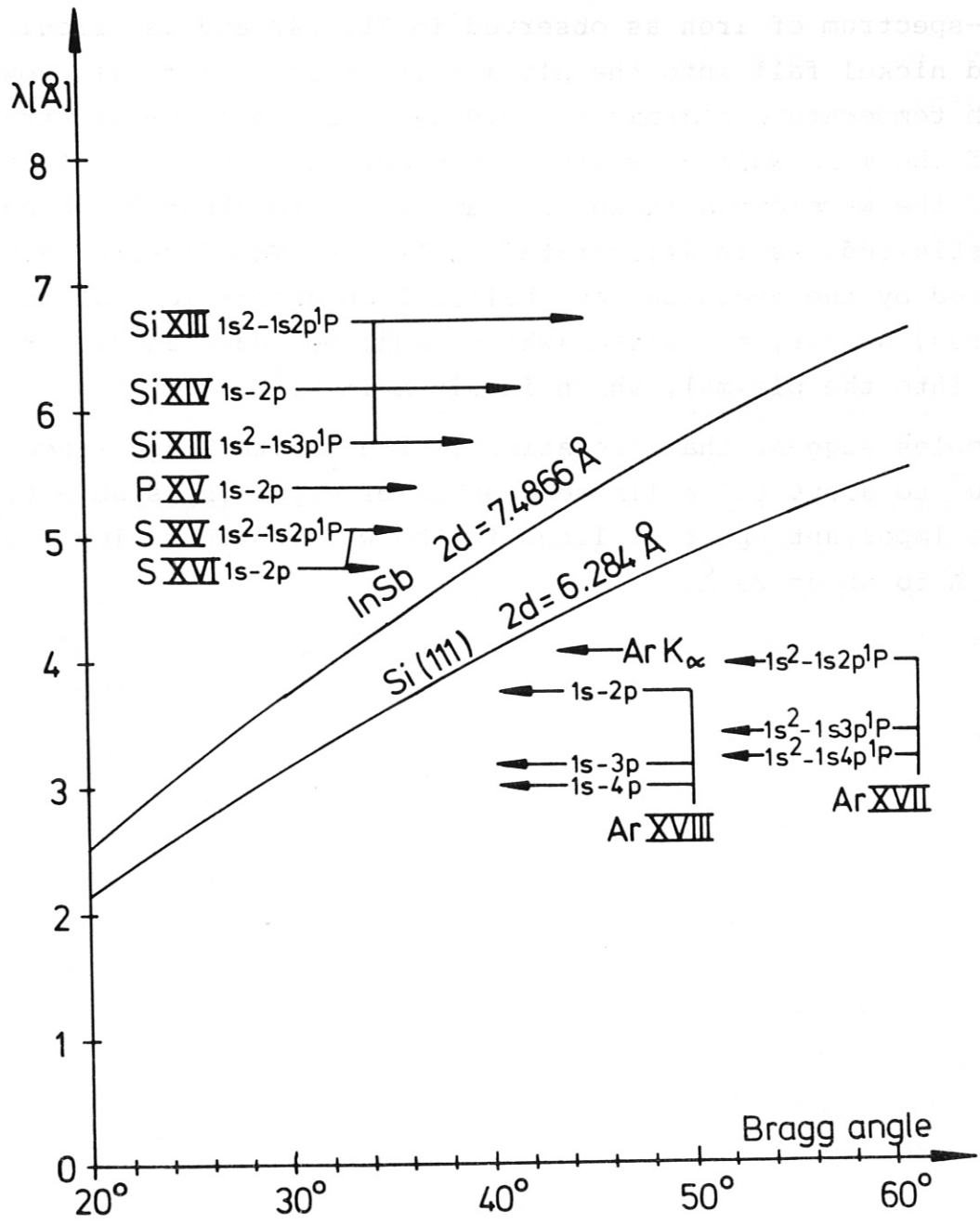

Fig. 5 Wavelength-Bragg angle relation of hydrogen- and helium-like transitions of intermediate-Z elements for first order reflection of InSb and Si(111)

iron (L-spectrum of iron as observed in PLT /4/ and as calculated /5/) and nickel fall into the ultra soft X-ray region. If, however, for high temperature plasmas the hydrogen- and helium-like transitions of the main wall constituent elements are of interest, for example, the wavelength range from about 1.3 to about 2.8 Å has to be investigated, as is illustrated in Fig. 4. The intermediate region is covered by the hydrogen- and helium-like transitions of silicon, phosphorus, sulfur, and argon (which might be added as tracer element into the plasma), which is given in Fig. 5.

The examples suggest that operating in the finite Bragg range of about 30° to about 60° a limited number of crystals is able to cover the most important spectral lines in the wavelength region from about 1 Å to about 25 Å.

For the choice of the crystals several conditions, which depend on the experimental parameters, have to be met. One is that the crystal lattice constant 2d should be such as to fulfill the Bragg condition for first order reflection in the wavelength and Bragg angle range envisaged, which asks for lattice constants ranging from about 2.5 Å to about 25 Å in order to get access to the above mentioned wavelength interval. The integral reflectivity of the crystal chosen should be as high as possible. The rocking curve angular width should not be too narrow in order to avoid non feasible mechanical accuracy. The homogeneity of the reflection properties of the large area crystals on the total surface should be given (the crystals must be available in the desired size). For active phase operation of JET the crystals should not change their reflection properties in the high neutron and hard X-ray fluxes.

Most of these conditions can easily be met. As is obvious from Figs. 3 to 5 some crystals - and there exist several alternatives to these (see /3/) - have lattice constants 2d just fitting the requirement that important spectral lines can be reflected in the Bragg angle range from about 30^{o} to 60^{o} for first order reflection. KAP (001) offers access to the hydrogen- and helium-like transitions of oxygen and e.g. to the L-spectrum lines of the Inconel 600 wall constituents nickel, iron and chromium (Fig. 3). LiF (220), Ge (400) or Topaz (303) have lattice constants that allow to reflect just the hydrogen- and helium-like transitions of the wall constituent elements (Ni, Fe, Cr, Co, Cu, Mn) within the mentioned Bragg angle interval, while LiF (200), Ge (220) or Si (220) have suitable lattice constants for the corresponding Ti-transitions (Fig. 4). For the intermediate-Z elements (Si, P, S) and for Ar, which might be arbitrarily added to the JET plasma for diagnostic reasons, InSb and Si (111) are appropriate crystals (Fig. 5).

The integral reflectivities of the crystals given as examples are relatively high (some are already listed in /3/): A. Burek /6/

gives values for the KAP (001) integral reflectivity of about $5 \cdot 10^{-5}$, while data for the integral reflectivity and the rocking curve widths, respectively, of the other crystals are found elsewhere /7,8,9,10,11/.

Concerning the rocking curve widths the crystals KAP (001) /6/ and InSb /7/ have large enough values, such that the conditions for mechanical accuracy are relatively moderate and hence crystal spectroscopy for low- and intermediate-Z elements (according to Figs. 3 and 5) can be performed without treatment of crystals. At a Bragg angle of 25^{o} the rocking curve width is of the order of one arc minute /6/. However, for crystal spectroscopy in the few Å wavelength region (Fig. 4) most of the crystals have relatively narrow rocking curve widths /7,8/ and rocking curve "widening" methods /11/ have to be applied (see chapter 3.2), in order to meet the mechanical accuracy.

This latter group of crystals contains some with limited lattice perfection /12,13,14,15/, which might result in inhomogeneities of the reflection characteristics on the crystal surface and hence are unsuitable for double crystal monochromators. Mainly natural crystals (like e.g. LiF and Topaz) show these inhomogeneities /10,15/ (see chapter 3.2 on crystal tests). By abrading techniques /11/ and choice of individual crystal pairs, however, all reflection conditions can be fulfilled.

With respect to the resistance of the crystal reflection properties against radiation damage from high neutron and hard X-ray fluxes as well as from power dissipated on the crystal very little information is available in the literature.

For crystals like quartz very high neutron fluences ($>10^{19}$ n/cm^2) are necessary to affect the X-ray reflectivity and line shape /16/. These fluences will by far not be reached at the crystal location for JET /3/. Organic crystals, however, like KAP might be influenced by high neutron fluences. Hence these crystals were tested in a reactor (see chapter 3.2 on crystal tests).

Radiation damage from X-ray energy dissipated on most of the crystal surfaces will not be expected for the JET experimental conditions

since elsewhere radiation damage started not before about 4 $kW \cdot h \cdot cm^{-2}$ integrated radiation exposure /7/. Exceptions are organic crystals like PET, EDdT, ADP, SHA, KAP or RAP /17,18/, since they are highly temperature sensitive and suffer radiation damage when exposed for long period of time to an extensive X-ray beam. However, for the JET conditions of power densities of less than 0.2 W cm^{-2} (which are comparable with the present power densities on the crystals at DORIS) no deleterious thermal effects should occur /20/.

Hence the question of radiation damage of KAP by neutrons and hard X-rays remains. However, in the active phase of JET these crystals can be replaced by Na-ß-alumina ($NaAl_{11}O_{17}$) with slightly smaller lattice constant (2d = 22.49 Å) than KAP, but high peak reflectivity and convenient rocking curve widths. Its stability to radiation is adequate and the crystals are almost perfect /18,19/.

Summarizing, for the three regions of interest, as roughly characterized by Figs. 3, 4 and 5, there exist first choices of crystals, KAP (001), LiF (220), and InSb, respectively, and alternatives, Na-ß-alumina, Ge (400), and Si (111), respectively (and many others).

2.2 General Monochromator Configuration

The double crystal device was chosen as the monochromator configuration for reasons of relatively fast wavelength scan over a wide spectral range, of efficient shielding against high neutron and hard X-ray fluxes and for fixed detector position. As proposed in /3/ the double crystal monochromator should be located outside the experimental hall, connected to the JET torus by a long vacuum tube that penetrates through the wall. Fig. 6 shows the general scheme of the monochromator. A long beam line is connected to the horizontal port No. 6 and penetrates the wall of the experimental hall through one of the plugs. The beam line is covered by a concrete collar, a shielding block, in order to reduce the direct neutron flux from port No. 6 towards the wall penetration.

The monochromator behind the wall is surrounded by shielding material. The labyrinth type beam alignment of the double crystal monochromator gives the possibility of very effective shielding against the high neutron and hard X-ray fluxes during D-T operation of JET.

As described in detail in /3/, the desired soft X-ray monochromatization is accomplished by two crystals each moving in longitudinal direction on a linear displacement table and in angular direction on a rotation table. The distance of the linear displacement tables is about 1 m. Both crystals are moved in such a way that they are always parallel to each other and that the soft X-ray beam is penetrating through a small hole in the shielding block. The outgoing beam direction is parallel to that of the incoming beam, displaced by the distance of the displacement tables. Hence the detector is at fixed position while the fast movement of the crystals allows fast wavelength scanning over a wide spectral range; a scan of a Bragg angle range from about 30^{o} to $6o^{o}$ in about 1 second is envisaged.

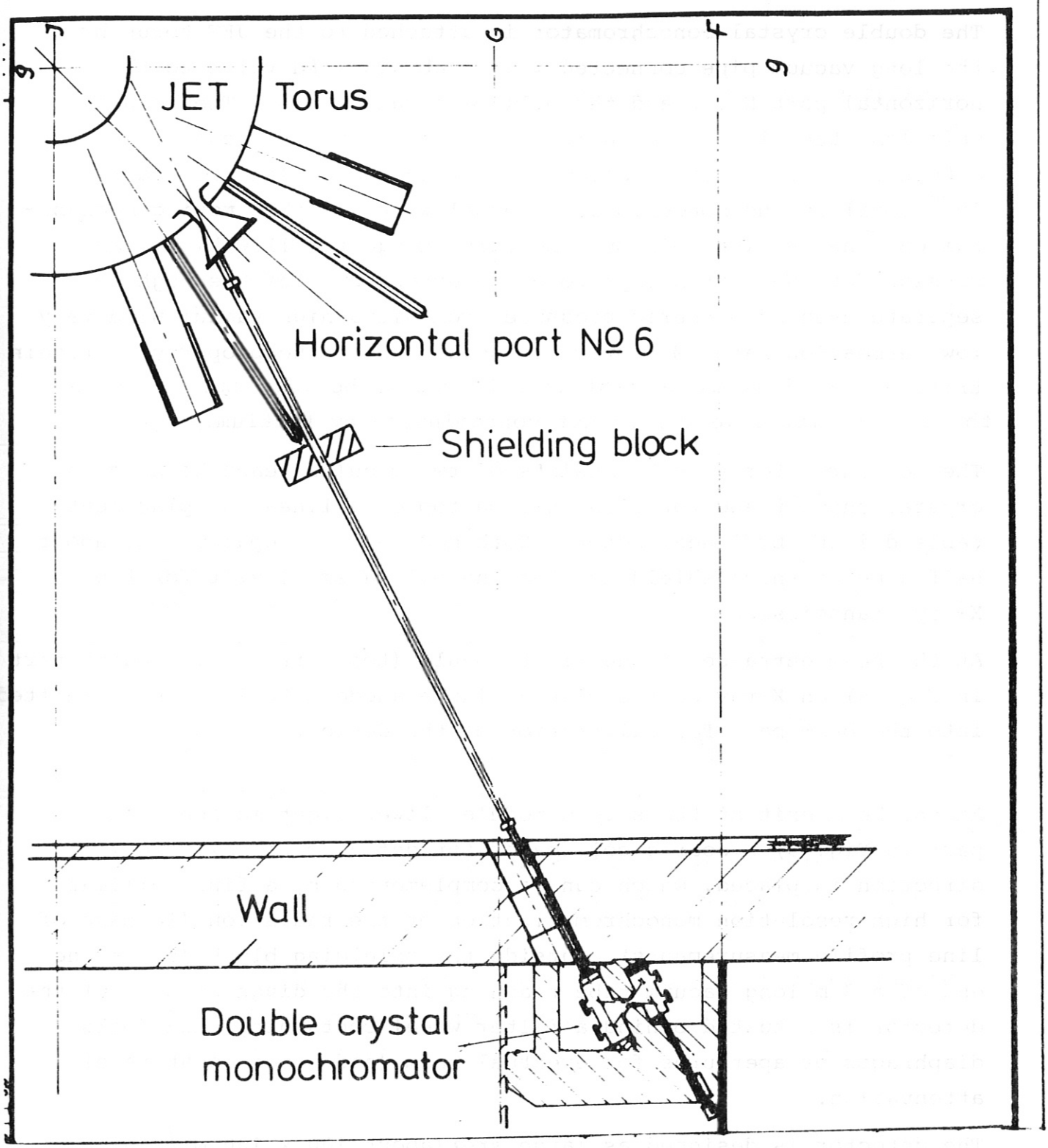

Fig. 6 Scheme of the active phase double crystal monochromator design for JET

The double crystal monochromator is attached to the JET torus by the long vacuum pipe connected via an absolute RH valve to the horizontal port No. 6 and the wall penetration tube. The volume of this long tube is separated from the monochromator vacuum vessel by a thin foil, in order to allow a moderate vacuum (in the order of 10^{-6} mbar) in the monochromator vessel with its fast moving mechanical components. The foil must be thin enough to allow high transmission for the soft X-rays to be detected, but thick enough to separate even atmospheric pressure from ultra-high vacuum with very low permeation rate. Moreover, it should have the property to retain tritium; the tritium permeation rate should be very small, so that the monochromator vessel is not contaminated by tritium.

The monochromator vessel consists of two modules, each housing one crystal support and rotation unit on top of a linear displacement table driven by linear motors. Both modules are separated by about half a meter thick shielding, leaving only a small slit for the X-ray transmission.

At the beam entrance of the first module (top left monochromator part in Fig. 6) an X-ray source with variable anode material can be shifted into the beam path for calibration of the device.

At the beam exit of the second module (lower right monochromator part in Fig. 6) a coarse collimator for defining the exit beam direction is placed, which can be complemented by a fine collimator for high resolution monochromatization of the radiation (in case of line profile measurements). Outside the shielding block (or at the end of a 3 m long vacuum tube reaching into the diagnostic area) the detector is situated behind a filter wheel containing thin foils, diaphragms or apertures for eventual beam (and hence count rate) attenuation.

The detector is designed as large area (about 100 x 100 mm^2) high count rate multi-wire proportional counter without spatial resolution, using e.g. P10 as detector gas.

3. Results of Component Tests

Due to the small rocking curve widths of some crystals the overall mechanical inaccuracies of the monochromator must be below certain limits. These limits are set either by the condition that two neighbouring spectral lines have to be clearly separated, which normally can be fulfilled with angular tolerances being less than a few arc minutes, or that line profile measurements should be possible, where inaccuracies less than 20 arc seconds are demanded.

As a result of these considerations the aim was to perform tests in two different respects:
One test group was devoted to the determination of the mechanical accuracy of all components of the design that contribute to the Bragg angle. These are the longitudinal displacement tables in quasi-static and fast motion and the rotation units with their corresponding incremental transducers. Most important is the parallelism of both crystals, to be determined especially for the control system operating.

The other group of tests was related to the optical properties of the crystals, especially their rocking curve widths and the means to change these widths towards desired values. Closely related to this question is the test of local independence of crystal reflectivity on its surface, which may strongly influence the integral reflectivity of a double crystal device if imperfect crystals /12,13,14,15/ are applied.

It is the results of these both groups of tests that determine the reliability and the range of applicability of the double crystal monochromator in question.

Further tests are related to the other components of the device, the thin foil, the X-ray calibration source, the collimator, and the detector.

3.1 Tests of mechanical components

The tests of mechanical components all aimed at determining the angular accuracy of the components to find out their influence on the Bragg angle positioning.

The test apparatus for the double crystal monochromator components to check the accuracy of the parallelism of both crystals and the control system during the fast wavelength scan consists of a Michelson interferometer with equal lengths of both optical paths. This interferometer is installed on a 1 m by 2 m large and 0.3 m thick granite block. For stable operation the interferometer is housed to reduce air convection, it uses tubes filled with helium to reduce refractive index gradient effects, and its mechanisms are optimally damped.

The interferometer is complemented by a linear displacement table (Jacob) plus motor for the spindle drive, two motors for the rotational motion, two electro-optical incremental transducers (Heidenhain ROD 700) and the corresponding control system (MANIA) as well as a laser.

The test can be performed placing a parallel glass plate into the optical path(s), in order to determine the angular motion of this plate by the measurement of the interferometer fringe shift. Using a thickness of 1.5 cm for the plate of refractive index n = 1.5 or n = 1.71736, respectively, one obtains the angular sensitivity of this interferometric device as indicated in the Fig. 7 for two different laser wavelengths, that of the He-Ne-laser at 6238 Å and that of the Argon-laser at 4880 Å, respectively. With the 6 cm glass block the sensitivity is increased by a factor of 4.

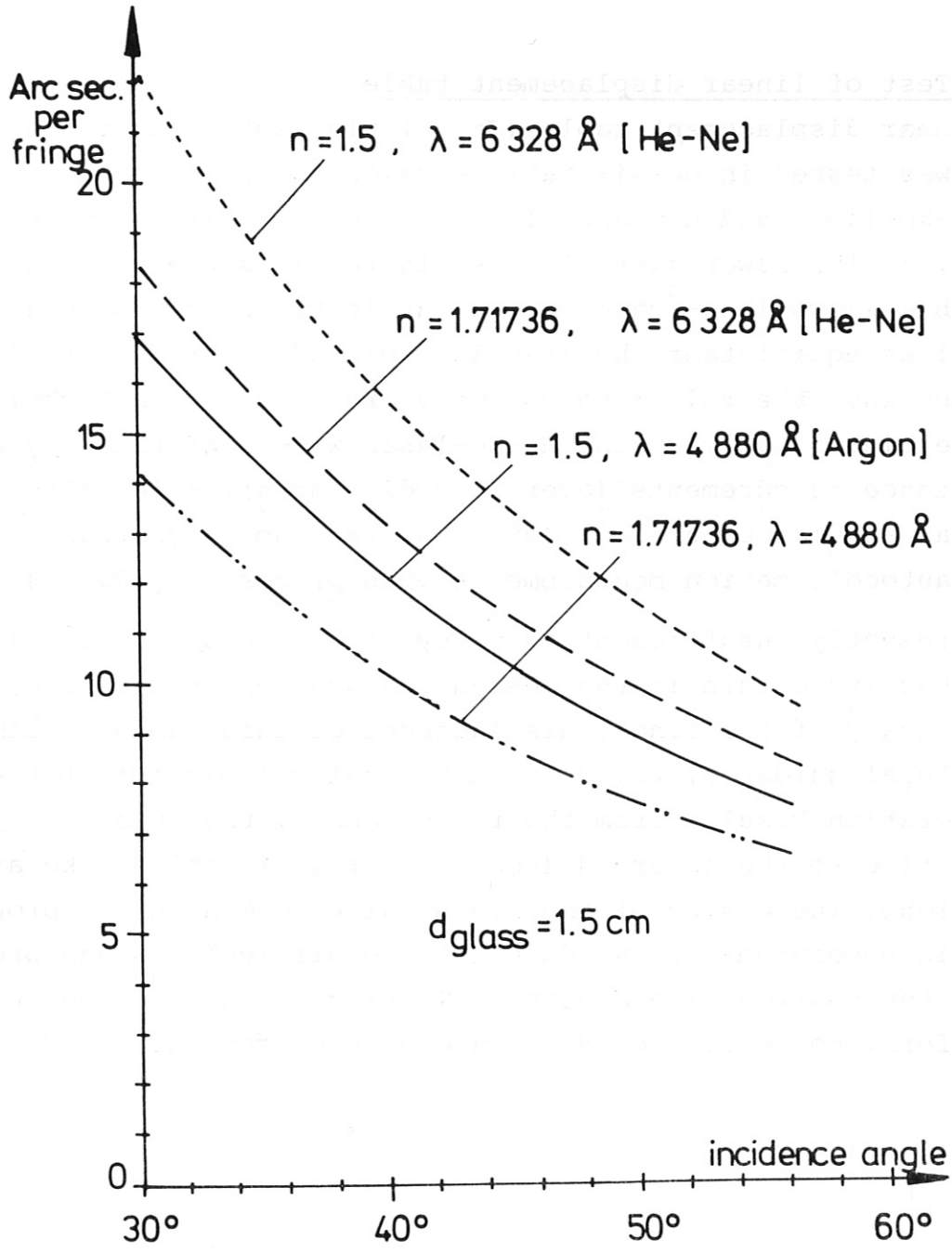

Fig. 7 Angular sensitivity of the interferometer for two different laser wavelengths versus the light incidence angle on 1.5 cm thick glass block

3.1.1 Test of linear displacement table

The linear displacement table (Jacob) plus motor for the spindle drive was tested in quasi-static version and in fast motion using the He-Ne-laser and a glass block as indicated in the upper part of Fig. 8. The lower part of this figure gives the test result. The table shows long-scale excursions in transverse angular direction as well as equidistant short-scale "spikes" related to the sphere entrance into the roller gears. These results of the Michelson interferometer applying the He-Ne-laser were confirmed by direct reflectance measurements (over long distances), which also gave the vertical angular excursions (of about the same magnitude), as well as by autocollimation measurements - as proposed by R. Deslattes /15/.

This presently insufficient accuracy of the Jacob linear displacement table has its origin in the design features of this system, since the accuracy of the linear displacement of this table is limited by the lateral guidance, which is mechanically overdetermined.A further deterioration results from the roller gears, the entering spheres giving rise to the observed (see Fig. 8) small spike-like angular deviations. The design of the linear displacement units proposed for this monochromator avoids all these difficulties and promises to get the desired high accuracy. Testing of this device in its final form, however, should be carefully performed.

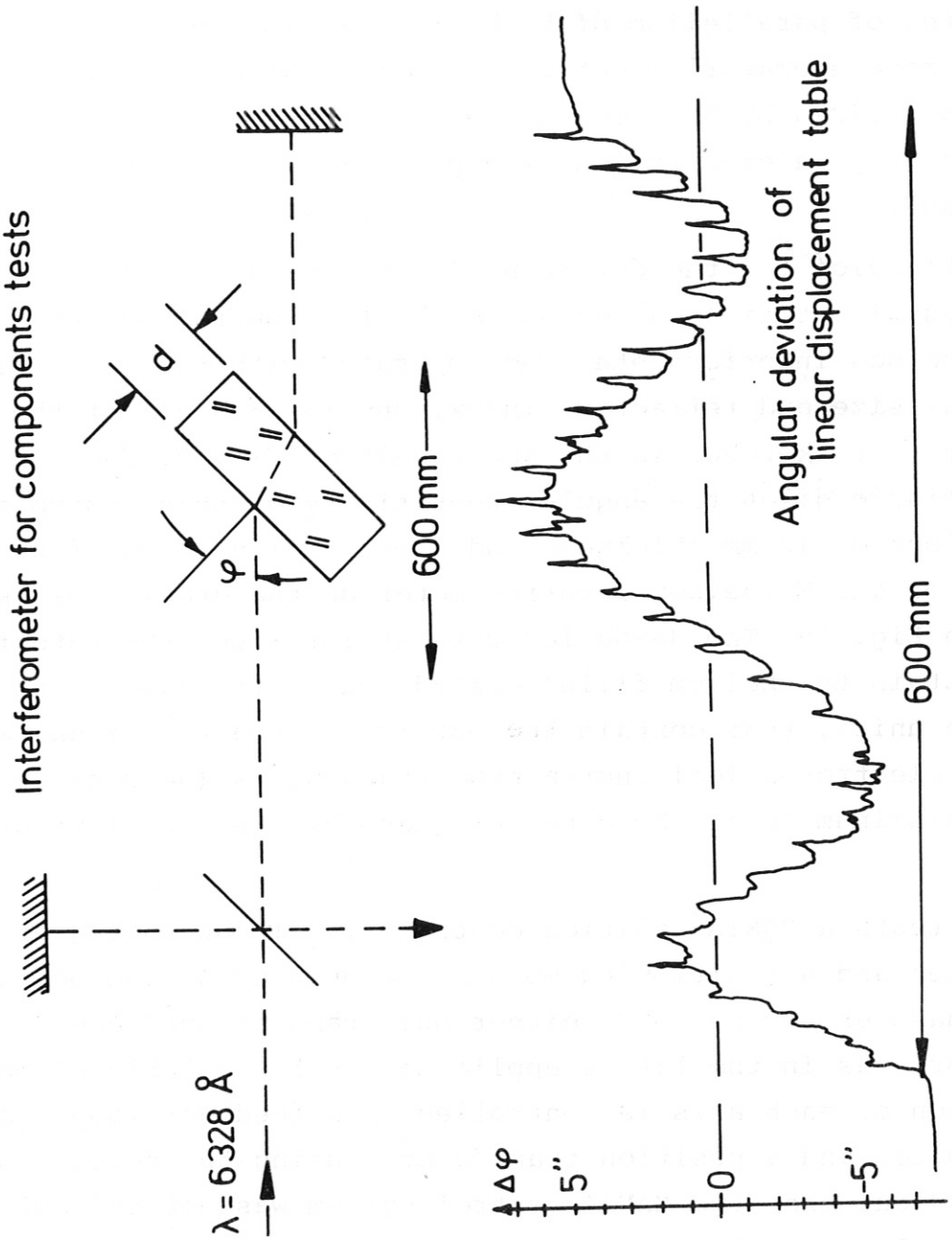

Fig. 8 Scheme of the glass block in the He-Ne-laser operated interferometer for angular deviation measurement of linear displacement table and result of angular excursions of the table during 600 mm longitudinal drive.

3.1.2 Test of crystal rotation table parallelism

The degree of parallelism of both crystals obtained in the double crystal monochromator directly determines which type of crystal - as characterized by its rocking curve width - can be applied and hence which parameter region of application of the instrument can be reached.

The test device for the determination of the angle difference of both crystal rotation tables as set by the control system is again the Michelson interferometer, now operated with two glass blocks of identical size and refractive index, one in each arm of the interferometer, as sketched in the upper half of Fig. 9. The lower part of the figure gives the angular sensitivity of this system for a glass block of 12 mm thickness and a refractive index of n = 1.5. A photo of the Michelson interferometer on the granite block is given in Fig. 10. The He-Ne-laser is at left; the two interferometer arms contain the helium filled cylindrical glass tube; both crystal rotation units, that contain the motors for the rotational motion and the electro-optical incremental transducers (Heidenhain ROD 700) in the aluminum tower, heading the glass blocks, are left of the centre.

For the tests a MANIA position control system consisting of a central controller and a positioning module has been used. The positioning module handles two motions, either one translational and one rotational motion or - as in the latter application - two rotational motions. The motion of each axis is controlled by a feedback loop consisting of the motor and a position transducer. During the tests, however, it turned out that the MANIA control system was not reliable enough for remotely controlled operation. Most of the problems were caused by the early development stage of the software delivered, such that for the control system of the double crystal monochromator the Contraves control system will be proposed .

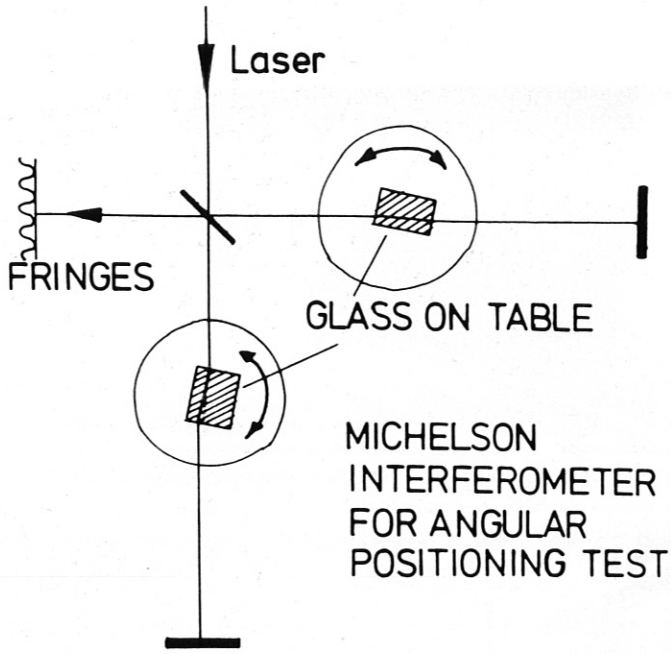

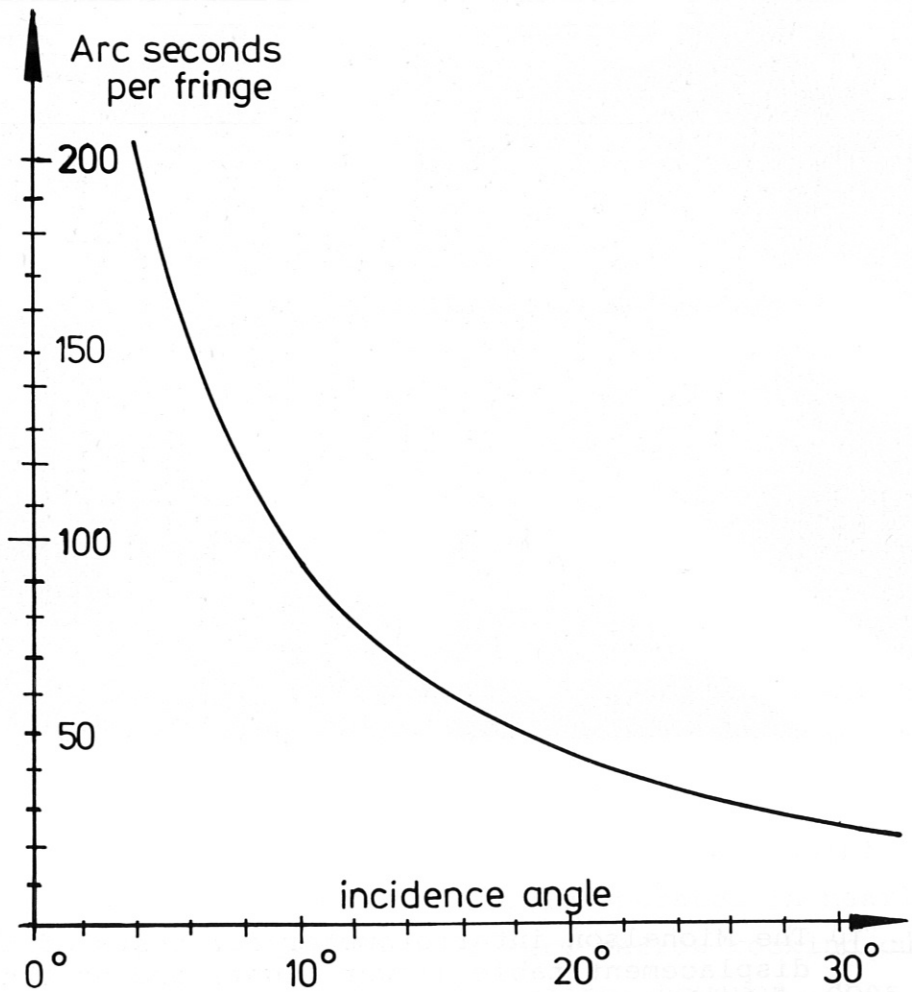

Fig. 9 Scheme of the Michelson interferometer for the measurement of angular differences of both crystal rotation units (above) and the sensitivity of this system versus the incidence angle of 6238 Å laser light.

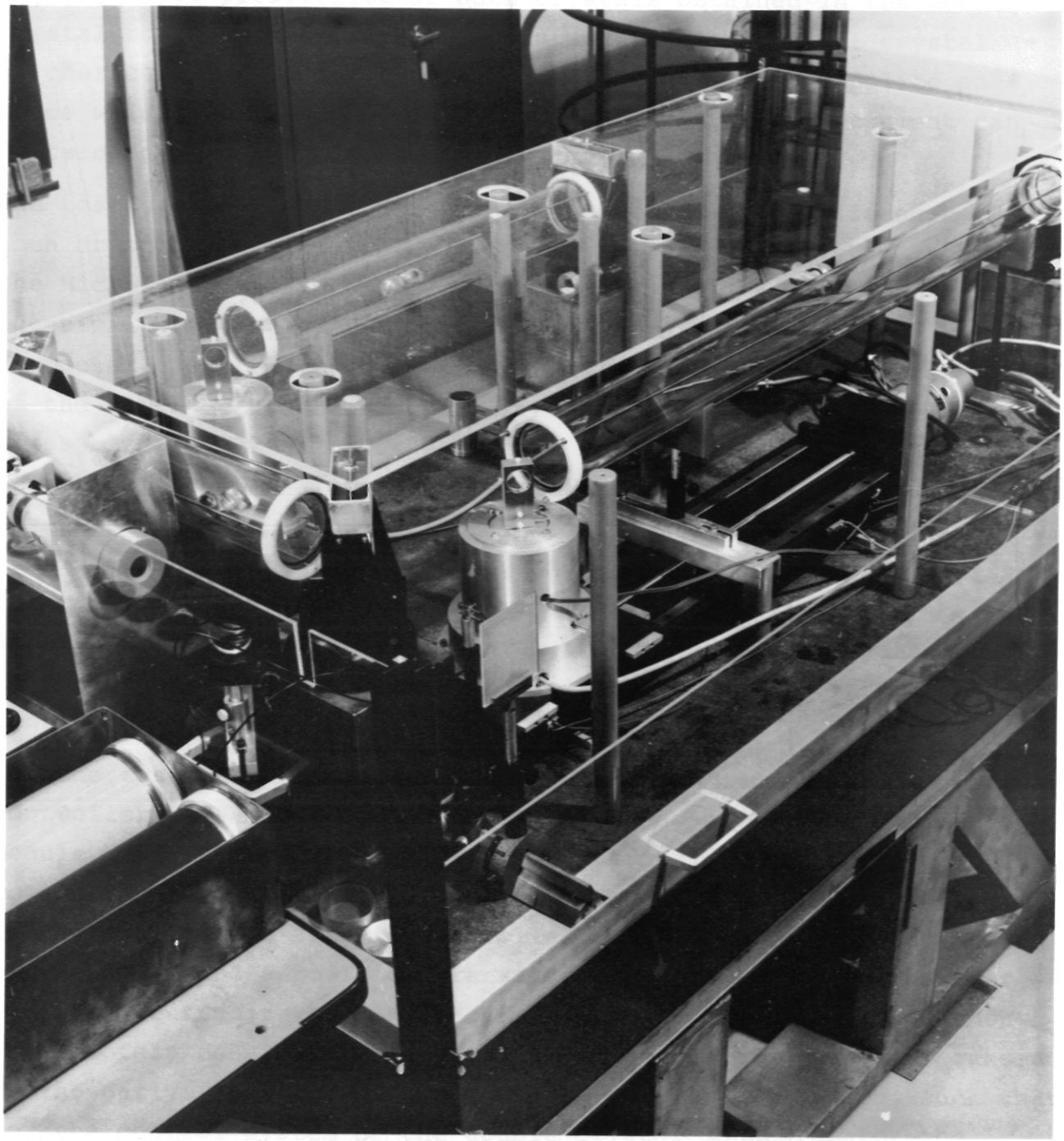

Fig. 10 The Michelson interferometer for tests of the linear displacement table (lower right) and of the parallelism of both crystal rotation units (to be seen left from centre). The He-Ne-laser is at the very left side.

After several changes it is now possible to control one longitudinal and one rotational axis in combined or separate motion (the longitudinal velocity reaching 500 mm/s, which is 75 % of the maximum speed of the displacement table) as well as two rotational axes.

The test of the crystal rotation tables showed that, with some restrictions, the required parallelism of 12 arc seconds can be marginally achieved. Sometimes, however, the observed jitter increased by a factor of two. The reason for this different behaviour is not yet understood. The other restriction concerns the acceleration and deceleration phase where deviations of more than 12 arc seconds frequently occur. Fig. 11 gives an example of a scan from 20^{o} to 10^{o} with the full speed of 30^{o} per second. The observed jitter is in the order of one half line width which corresponds to 12 arc seconds deviation in either direction.

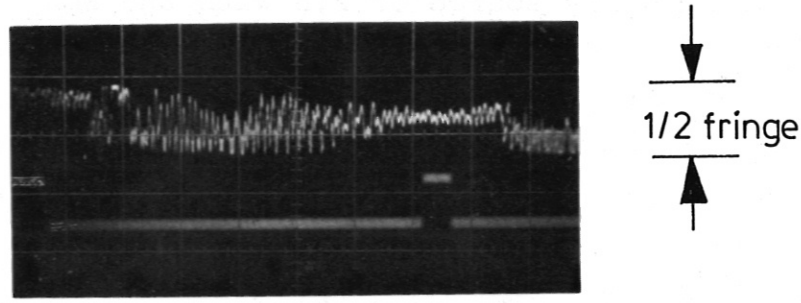

Fig. 11 Example of parallelism test of both crystal rotation units including the MANIA control system (time scale 100 ms/div.)

It seems likely that an increase in the position sampling frequency by a factor of four, as proposed by Contraves, should improve the accuracy considerably.

From these results and possible improvements it seems feasible that the double crystal monochromator can be reliably operated in nearly all modes of application except for cases of very narrow rocking curve width crystals at small Bragg angles. This limitation, however, does not seriously reduce the applicability of the envisaged double crystal monochromator.

3.2 Crystal Tests

The double crystal monochromator configuration built with crystals of relatively small rocking curve widths is very sensitive to crystal lattice imperfections/12,13,14,15,22/. If the deviations of the lattice orientation on the crystal surfaces are larger than the (locally determined) rocking curve widths the integral reflectivity of the double crystal device will substantially go down. Mainly natural crystals show these inhomogeneities /10,15,22/.

Since LiF (220) has a convenient lattice constant (2d = 2.848 Å) for diagnosing the hydrogen- and helium-like transitions of the wall constituent elements in the Bragg angle range from about 30° to 60° (see Fig. 4 on p. 6), this type of crystal was tested for several different samples.

At first cleaved LiF (220) crystals of 70 x 100 mm^2 surface area and 3 mm thickness, delivered by Quartz and Silice, were investigated using the 30 kW X-ray source of PTB with the $MoK_{\alpha 1}$ line at a wavelength of about 0.709 Å. The surface of the crystals was scanned in four different strips of 20 mm hight and 1.2 mm width (resulting from 0.3 mm width of the tungsten aperture) along the long side (100 mm) of the crystal. At every local position the angle Θ of maximum reflection was determined and plotted as deviation $\Theta - \bar{\Theta}$ from an average angle $\bar{\Theta}$.

An example of these measurements is plotted in Fig. 12 . The maximum reflection angle deviation varies by up to about 100 arc seconds, which is much more than the (local) rocking curve width, which is indicated as the error bar. The variation, however, is of long-scale character; there seem to exist areas of dimensions in the cm-range which are of high crystal quality.

In order to find out the reason for the strong variations, which might originate from $\Delta d/d$ effects or from tilting of the lattice elements, the crystal was reversed by 180°, and the same strip was measured (now with the complementary angle). As is obvious from Fig. 12

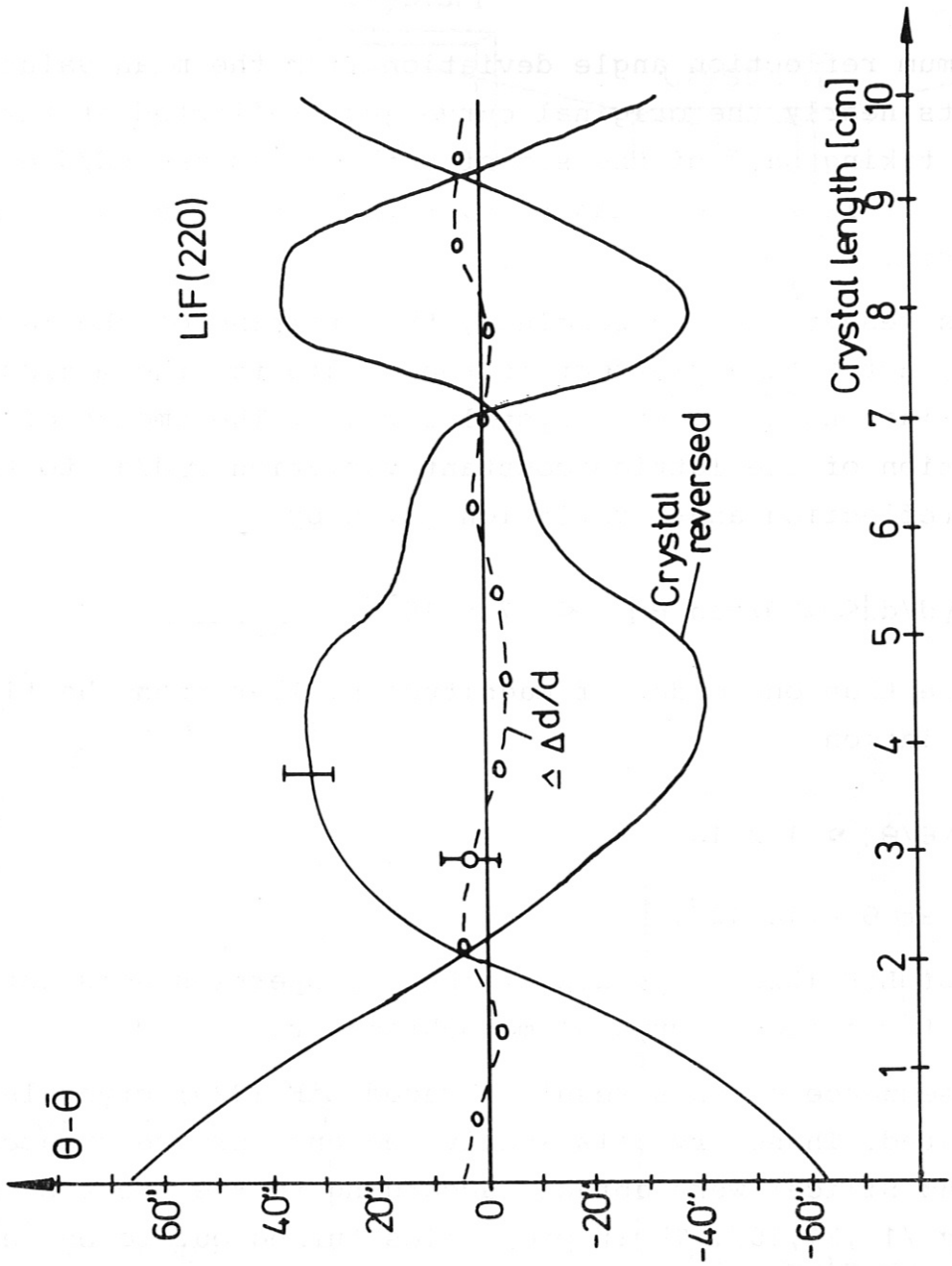

Fig. 12 Position of maximum reflection angle versus location on the crystal surface of LiF (220) together with that of reversed crystal

the maximum reflection angle deviation from the mean value $\bar{\theta}$ represents nearly the original curve just reflected at the abscissa. Hence if taking half of the sum of both curves the $\Delta d/d$-effect appears. It is smaller than 4" over the total length of the investigated strip.

From this result one can conclude, that tilting of the lattice elements, not the $\Delta d/d$-effect is the origin for the maximum reflection angle variations along the crystal surface. The amount of a possible contribution of the lattice constant variation $\Delta d/d$ to the observed maximum reflection angle variation given by

$$|\Delta d/d| \leq |\Delta\theta/\tan\theta| < 7.5 \cdot 10^{-5}$$

is by more than one order of magnitude smaller than the tilting angle variation

$$|\Delta\theta/\theta| \simeq 1.2 \cdot 10^{-3}$$

observed at $\theta = 14.42^{o}$.

Pairing of LiF (220) crystals of these properties does not seem feasible for a double crystal monochromator.

As a consequence of this result abraded LiF (220) crystals were investigated. These crystals (delivered and surface-treated by Quartz and Silice) were abraded according to the process developed at Saclay /11,21,10/. Their properties turned out to be very much more suitable for the use in the designed double crystal monochromator.

For these abraded LiF (220) crystals the double crystal device as sketched in the upper part of Fig. 13 could be applied, because of the much higher integral reflectivity of the abraded crystals. The spatial dependence (on the crystal surface) of both successive reflections was accomplished by moving a 2 kW X-ray source with its MoK_{α} line radiating) and the NaJ (Tl) detector (with 1.25 mmx30 mm

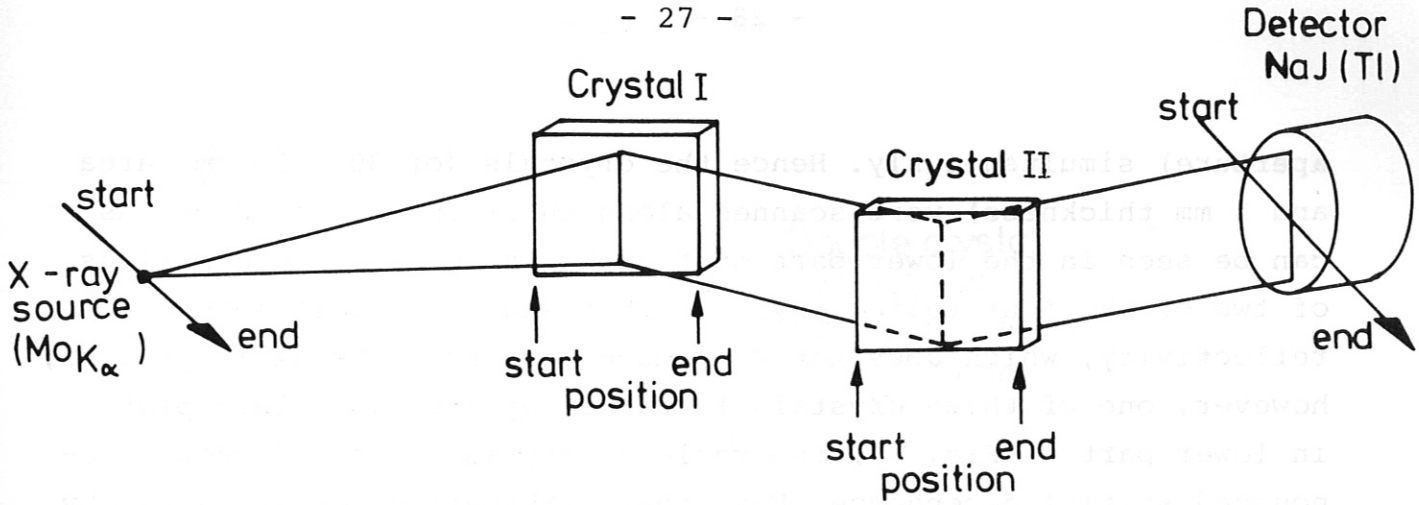

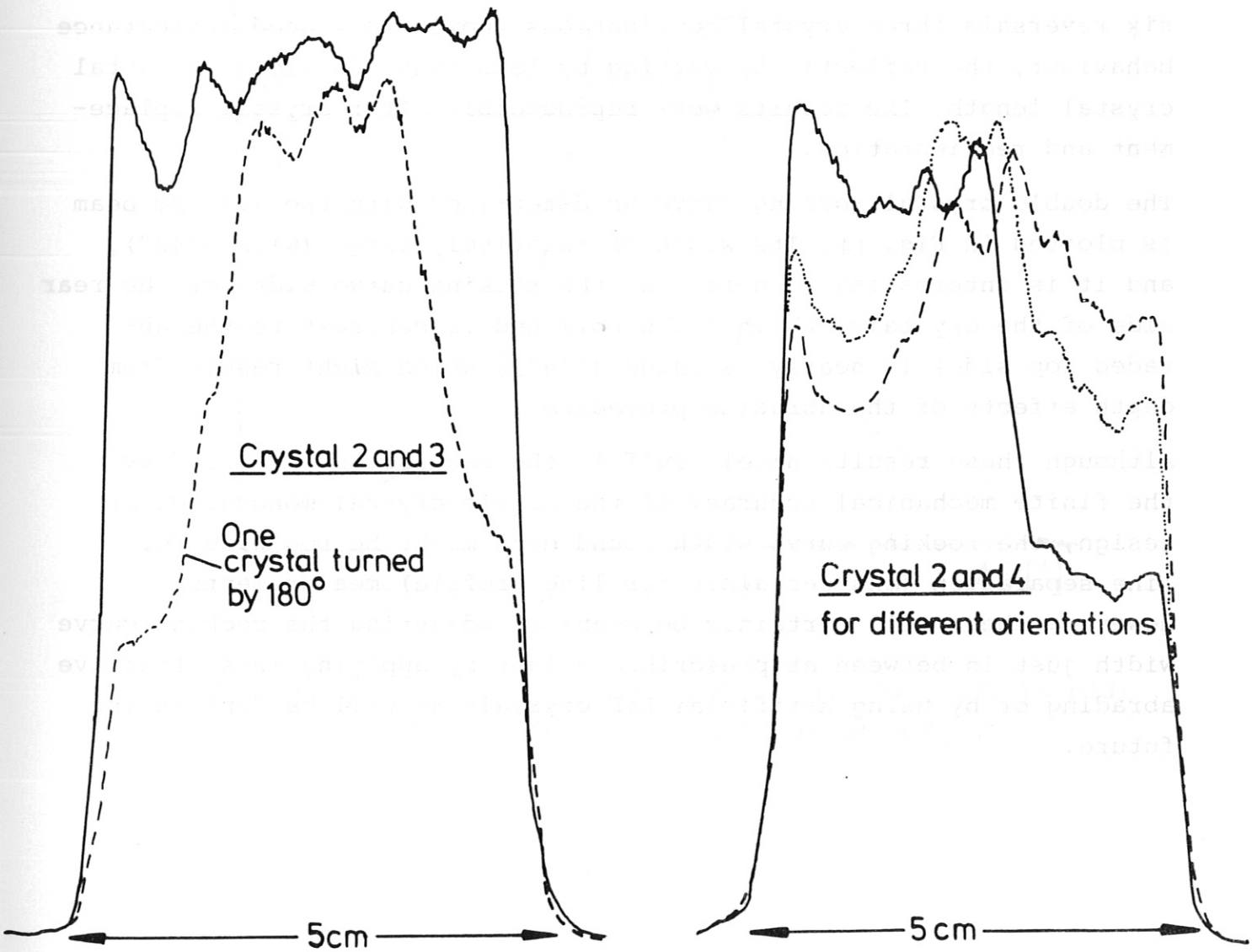

Fig. 13 Test of double crystal local reflectivity of abraded LiF (220) crystals with the arrangement sketched in the upper part. The scanning along the 5 cm long side of the crystal shows nearly spatially constant (high) reflectivity (solid line in left lower plot) for certain crystal combinations, while turning one of the crystals (dotted plot in left lower part) or other combinations (right lower part of figure) result in lower and spatially dependent reflectivity.

aperture) simultaneously. Hence the crystals (of 30 x 50 mm^2 area and 3 mm thickness) were scanned along their 50 mm dimension. As can be seen in the lower part of Fig. 13 there exist combinations of two of the four tested crystals that show a (local) integral reflectivity, which does not vary much over the crystal length. If, however, one of these crystals is turned by 180° (see left plot in lower part of Fig. 13) the reflectivity is worse and shows pronounced spatial dependence. For other combinations optimization by changes of relative orientation was tried without success, as is obvious from the right plot in the lower part of Fig. 13.

Among the four crystals being tested with its six combinations and six reversals three crystal combinations showed very good reflectance behaviour, the reflectivity varying by less than 10% along the total crystal length. The results were reproducible after crystal replacement and reorientation.

The double crystal rocking curve as determined with the 1.25 mm beam is plotted in Fig. 14. Its width is relatively large (with 2'40"), and it is interesting to note that the rocking curve width of the rear side of the crystals (which looks polished in contrast to the abraded top side) is nearly as large (2'6"), which might result from depth effects of the abrading procedure.

Although these results nicely fulfill the requirements imposed by the finite mechanical accuracy of the double crystal monochromator design, the rocking curve width found here might be too wide for line separation (and certainly for line profile) measurements. However, there will certainly be means of adjusting the rocking curve width just in between at prescribed values by applying less effective abrading or by using artificial LiF crystals as will be done in the future.

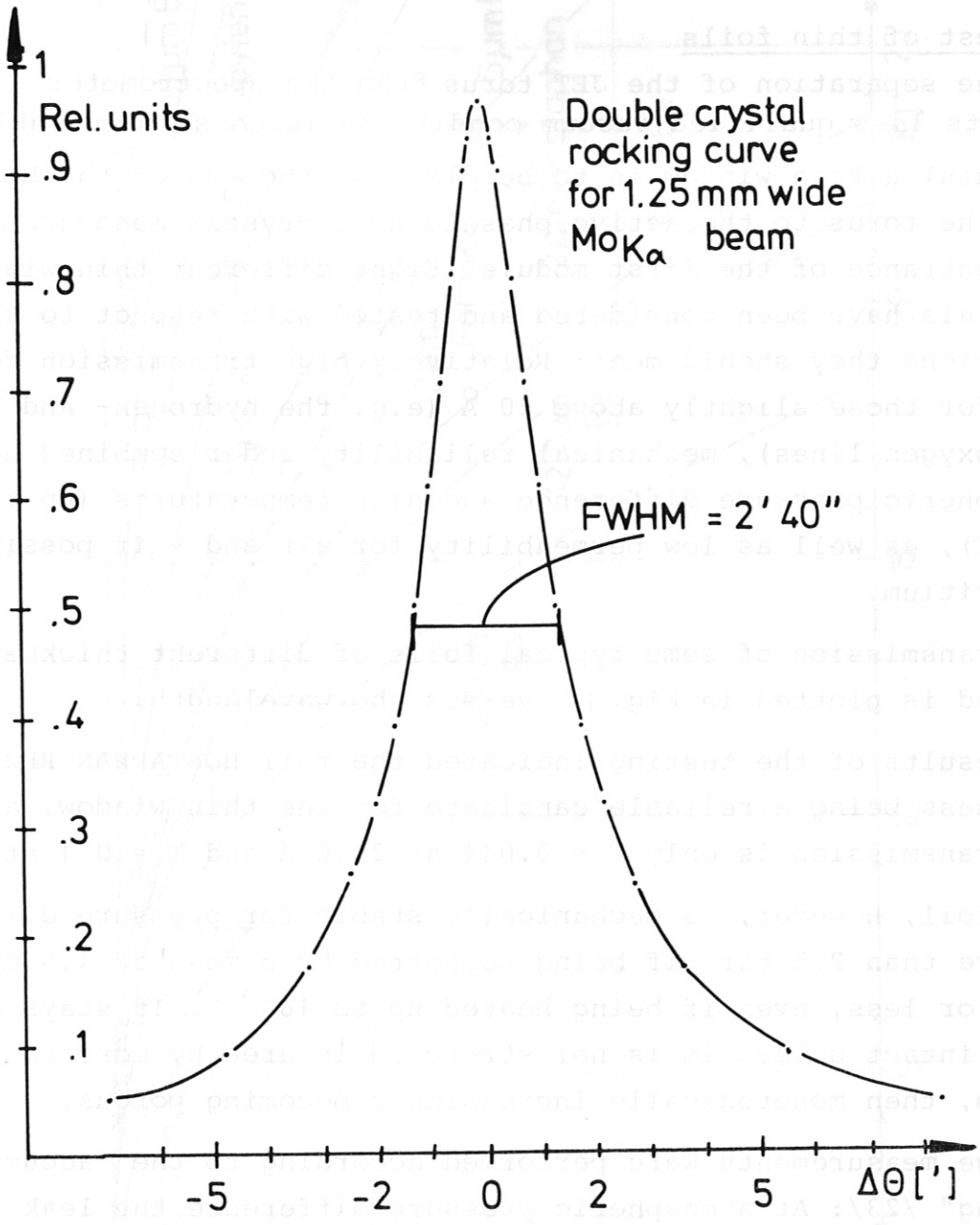

Fig. 14 Double crystal rocking curve (locally determined) for abraded LiF (220) crystals at MoK_{α} .

3.3 Test of thin foils

For the separation of the JET torus from the spectrometer with its less qualified vacuum conditions (because of movable elements) a thin window is to be placed at the end of the beam line from the torus to the active phase double crystal monochromator, at the entrance of the first module. Eight different thin window materials have been considered and tested with respect to the many conditions they should meet: Relatively high transmission for photons, also for those slightly above 20 Å (e.g. the hydrogen- and helium-like oxygen lines), mechanical reliability under combined action of atmospheric pressure difference and high temperatures (up to about 150° C), as well as low permeability for air and - if possible - for tritium.

The transmission of some typical foils of different thickness considered is plotted in Fig. 15 versus the wavelength.

The results of the testing indicated the foil HOSTAPHAN RE2 of 2 µm thickness being a reliable candidate for the thin window, although the transmission is only T = 0.044 at 21.6 Å and T = 0.1 at 19 Å.

This foil, however, is mechanically stable for pressure differences of more than 2.5 bar, if being supported by a mesh of 1.5 mm distance or less, even if being heated up to 180° C. It stays mechanically intact unless it is not stretched in area by more than a factor of two, then monotonically increasingly becoming porous.

Leakage measurements were performed according to the "accumulation testing" /23/: At atmospheric pressure difference the leak rate of an effective area of more than 2.5 cm^2 was

$$Q = V\, dp/dt = 30\ l \cdot 10^{-3}\ mbar\ /60\ s = 5 \cdot 10^{-4}\ mbar\ l/s,$$

which for an area of about 75 cm^2 and a pressure difference of 10^{-6} mbar will result in a leak rate of less than

$$Q = 1.5 \cdot 10^{-8}\ mbar\ l/s.$$

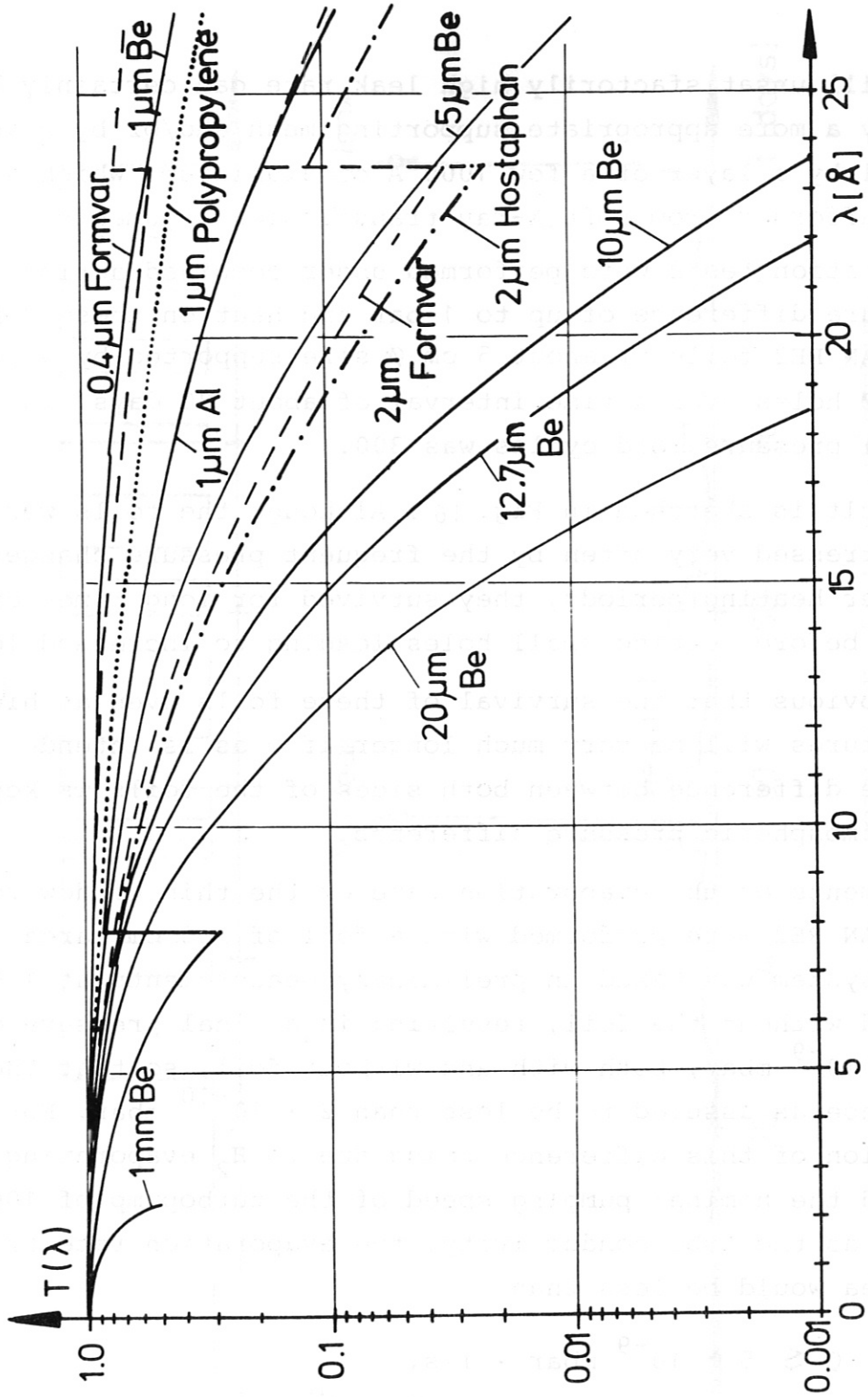

Fig. 15 The transmission of some typical thin foils with different thickness versus wavelength

This still unsatisfactorily high leak rate can certainly be reduced by a more appropriate supporting mesh and/or by covering the foil by a layer of a few 1000 Å of aluminium, which just can be afforded from soft X-ray transmission arguments.

Long- duration tests were performed under combined action of a pressure difference of up to 1 bar and heat on these 2 µm thick HOSTAPHAN RE2 foils of about 5 cm Ø size supported by a frame of 1.5 mm Ø holes over a time interval of about 80 days. The number of total pressure load cycles was 300.

The result is sketched in Fig. 16 . Although the foils were mechanically stressed very often by the frequent pressure changes during and after heating periods, they survived for long times of about 40 days before getting small holes leading to increased leak rate.

It is obvious that the survival of these foils even at higher temperatures will be very much longer if - as is intended - the pressure difference between both sides of the foils is kept much below atmospheric pressure difference.

Measurements of the evaporation rate of the thin window foil HOSTAPHAN RE2 were performed with a foil of 300 cm^2 area. The vacuum system was baked in preliminary measurements at 130^{o} C with and without the foil, resulting in a final pressure of $p < 4 \cdot 10^{-9}$ mbar, both with and without foil, so that the pressure difference is assumed to be less than $2 \cdot 10^{-10}$ mbar. For the assumption of this difference being due to H_2 evaporating from the foil and the nominal pumping speed of the turbopump of 100 l/s as well as the tube conductivity, the evaporation rate of a 75 cm^2 foil area would be less than

$$Q \lesssim 5 \cdot 10^{-9} \text{ mbar} \cdot \text{l/s}.$$

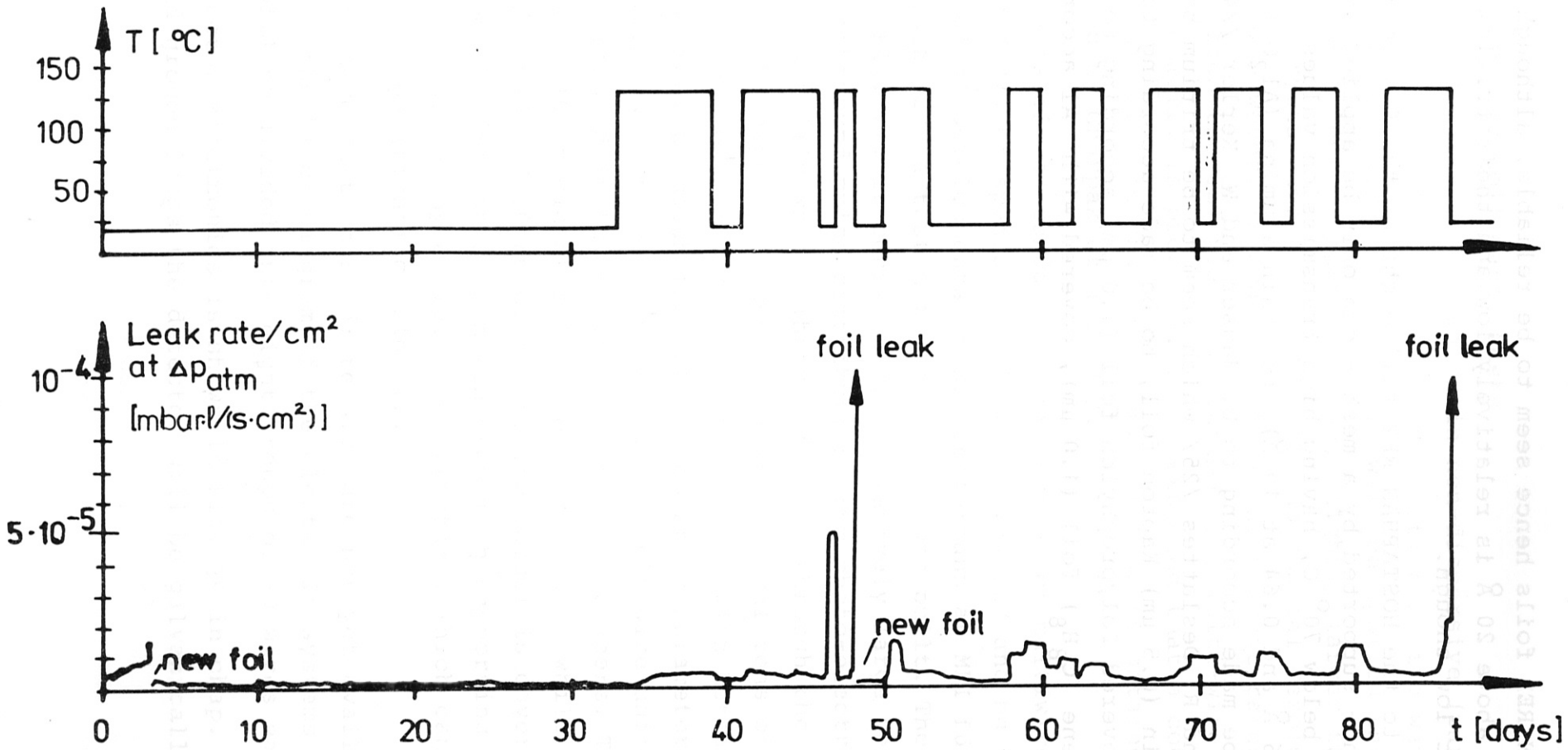

Fig. 16 Long duration tests of 2 µm thick HOSTAPHAN RE2 foils under combined action of heat and atmospheric pressure difference

The HOSTAPHAN RE2 foils hence seem to be reliable, although their transmission above 20 Å is relatively low and their tritium permeability not low enough.

Alternatives to the HOSTAPHAN RE2 foil might be the 0.4 µm Formvar-window, which - supported by a mesh - can only be applied at temperatures below 70° C, having high transmission values (0.56 at 21.6 Å and 0.64 at 19 Å), the thin alumina (Al_2O_3) - windows, to be made according to U. Hauser and W. Kerler /24/ and H. Johnson and R. Deslattes /25/ which seem to be tritium barriers /15/, the thin (0.5 µm) Kapton foil, to be made according to /26/, the Carbon-covered Polyprophylen foil (1.0 µm) according to /27/ or the Parylene (C_8H_8) foil (1.0 µm), covered with Al according to /4, 28/.

3.4 Detector and collimator tests

The double crystal monochromator in non-dispersive (parallel) mode has the advantage of fixed detector position during wavelength scanning. Since only plane crystals will be applied the sensitive area of the detectors must be large, slightly larger than the effective crystal area (70 x 86 mm^2). No spatial resolution is necessary. However, in order to obtain high count rates, which are expected from the JET plasma radiation /3/, multi-wire proportional counter geometry is proposed. It is expected that a counting rate of the order of more than 10^5/s per wire can be obtained, as demonstrated by Charpak et al. /29/.

On the basis of the fundamental properties of multiwire proportional counters /30/, of special developments /31,32/ and mainly on the technological developments of E. Pfeffermann at MPI für Extraterrestrische Physik /27/ a test detector device was built. The device is shown in Fig. 17. It consists of a relatively large vessel, which avoids background pulse contribution from photo-electron emission at nearby metallic walls. The gas flowing through the vessel can be changed with respect to pressure (from several tens of m Torr to more than one atmosphere and gas type (argon with Methane, Xenon,...) /30/, in order to match the optimum counting parameters for the chosen wavelength and counting rate range. The multiwire units consist of a frame oriented in the desired position by spacers. They carry about 80 wires of 10 µm diameter for the anode plane, while the cathode wires are made of 20 µm diameter. The vessel is covered by a 2 µm HOSTAPHAN RE2 foil on a thin tungsten mesh supporting grid which again is supported by a slot type structure, which can be seen in the top flange (right) of Fig. 17.

The tests have just started; results are not yet available. As described in the block diagram of the electronic systems the anode wires will be divided into eight groups of 10 wires each.

The detector electronics is shown in Fig. 35 in chap. 4.5. In order to avoid ground loops the detector will be galvanically decoupled

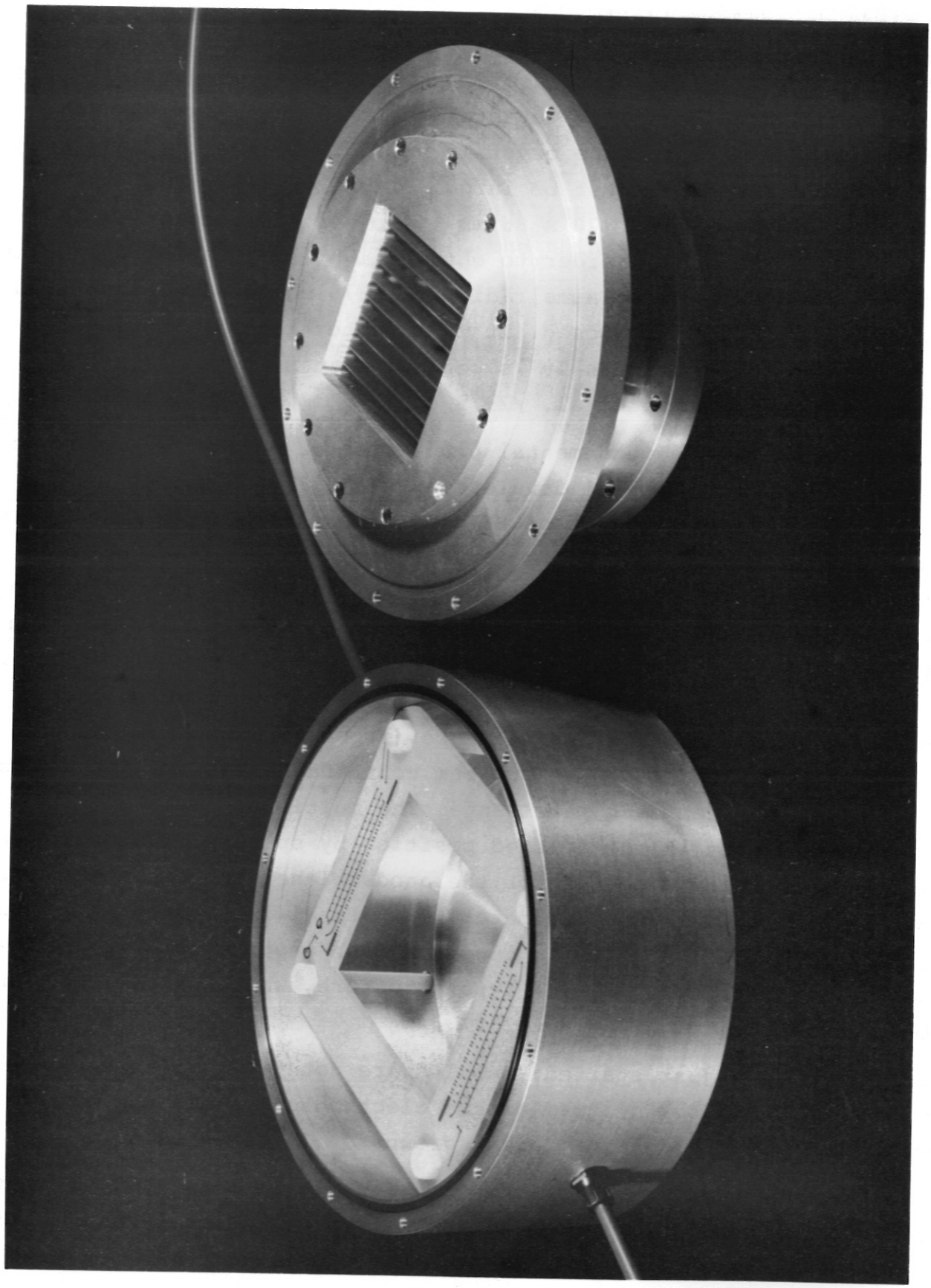

Fig. 17 Multiwire proportional counter test device

from the experiment. The detector wires are connected in 8 groups of 10 wires, each group having a separate preamplifier, mounted close to the detector. Each amplifier chain contains a pulse shaping main amplifier and a window discriminator. The output pulses of the 8 channels are summed up and then counted by a latching scaler. The scaler contents is transferred (together with real-position information from the positioning system) to a memory at load pulses generated by a programmable pulse generator.

The collimator is necessary for beam acceptance limitation for enabling spectral line separation and the separation of the spectral lines from satellites, the resolution being in the order of 600, or - for the case of line profile measurements for ion temperature evaluation by Doppler profile - in the order of 5000.

For the coarse collimator a model Soller collimator made of 49 lamellae of Cu-Be alloy of 0.1 mm thickness was tested. The transmission was measured as function of the angular position $\Delta\varphi$, as plotted in Fig. 18, using the $Cu_{K\alpha}$ radiation of the X-ray calibration source. The FWHM of the angular acceptance is roughly equal to the width as expected from the geometrical dimensions. Also the transmission was found to be in the order of the expected value.

This model collimator had smaller cross section than desired for the monochromator in question. It will be possible to reach the necessary resolution also for the large beam cross section of 70 x 87 mm^2.

For the active phase double crystal monochromator in question, however, even the "natural" spectral resolution /3/, which from the geometrical parameters turns out to be about 370, is sufficient to separate triplett- and singulett helium-like Ni- and Fe-spectral lines. It is just low enough not to narrow the full Doppler profile. However, for this application the crystals should have a resolution of $\lambda/\Delta\lambda \gtrsim 400$, because otherwise line separation would not be possible.

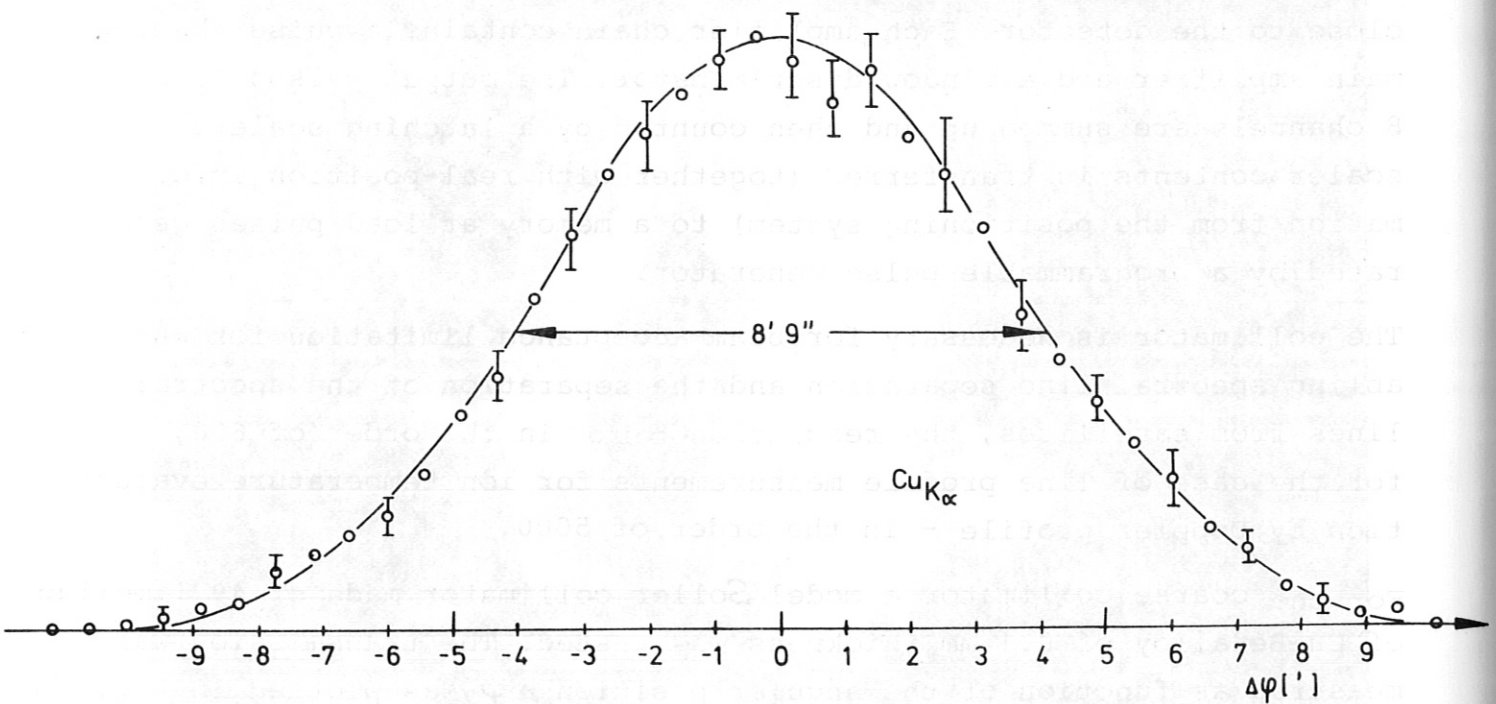

Fig. 18 Transmission of Soller collimator versus angle

For line profile measurements (at temperatures of about 5 keV) the collimator resolution should be in the range of 4000 to 5000, and the crystal choice should be limited to those with $\lambda / \Delta\lambda \simeq 10^4$, which corresponds to rocking curve widths in the range of 20 arc seconds.

This small acceptance collimator, however, deserves much more attention /33/. For this application a combination of a coarse Soller collimator and a fine grid collimator (following /34,35/) would be the best, if it is assured that the blades and grid wires are not commensurate /33/.

4. Engineering Design

4.1 General design and shielding

The general monochromator configuration was described in 2.2. Here we present some details of the beam dimensions, the shielding configuration of the monochromator and the crystal support, while in 4.2 the design drawings are described.

The beam outer dimensions at the different locations from the connection (A) at the horizontal port No. 6 through the concrete wall (C,D) and the monochromator housing entrance (E) to the effective crystal size (F) are plotted in Fig. 19. They should be realized as minimum inner dimensions of the beam line.

The design of the monochromator shielding is plotted in Fig. 20. The concept is similar to that described in /3/. Although the dimensions have slightly been increased due to larger outer dimensions of the monochromator modules, the shielding properties should be roughly the same as given in /3/. This shielding house is completed by the concrete collar of 0.6 m thickness and 1.8 m by 1.8 m area around the beam line, as schematically drawn in Fig. 6 (page 13).

The shielding house should be made according to Fig.20 . It should locate the epoxi resin concrete plate(on which the monochromator is placed and adjusted)such that its upper surface is 575 mm below the torus midplane (in which the beam centre is emerging from the plasma).

The shielding house should have a top concrete plate which can be removed for installation or major repair operation of the monochromator device. Moreover it should give access for small repair or minor operations like crystal changes, e.g. through manholes in the top concrete plate, which lead into each of the two module chambers. The plugs are to be carried by a small crane. Each of the chambers must be accessible for crystal change or small repair operation.

The shielding is made to fulfill the safety condition of less than 30 mrem per year for permanent stay at a distance of 5 to 6 m from the beam exit location, which can easily be met.

port size (A) 184 × 122 mm

crystal size 70 × 100 mm

F in 60° position 70 × 86,6 mm

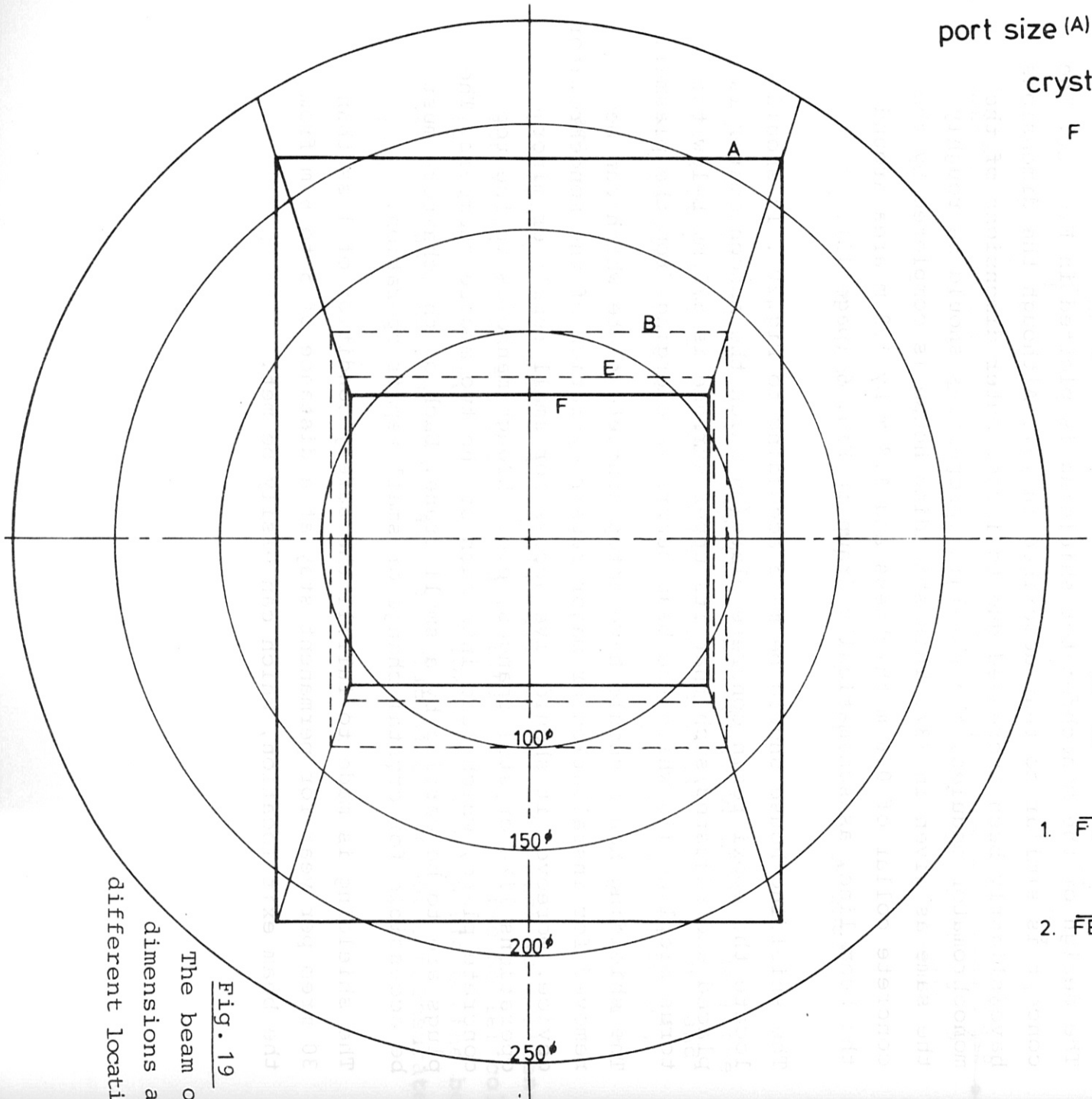

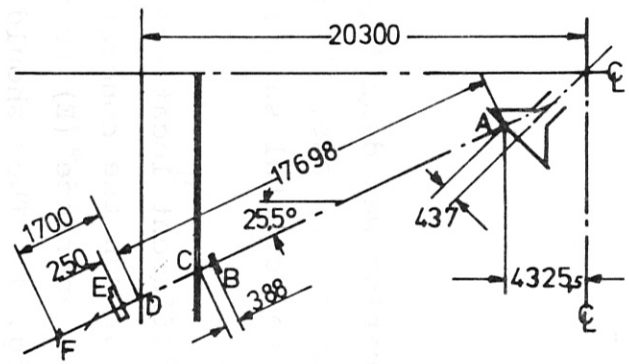

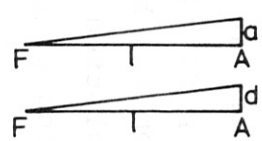

$\sin \alpha_{vert.} = \frac{a}{l} = \frac{92-35}{19400} = 0{,}002938$

$\sin \alpha_{hor.} = \frac{d}{l} = \frac{61-43{,}3}{19400} = 0{,}000912$

1. $\overline{FE}$ = 1450 mm

$a_1 = 35 + \tan \alpha_{vert.} \times \overline{FE} = 39{,}3$ mm

$d_1 = 43{,}3 + \tan \alpha_{hor.} \times \overline{FE} = 44{,}6$ mm

2. $\overline{FB}$ = 5190 mm

a_2 = 50,2 mm

d_2 = 48 mm

M 1:1

Fig. 19 The beam outer dimensions at different locations

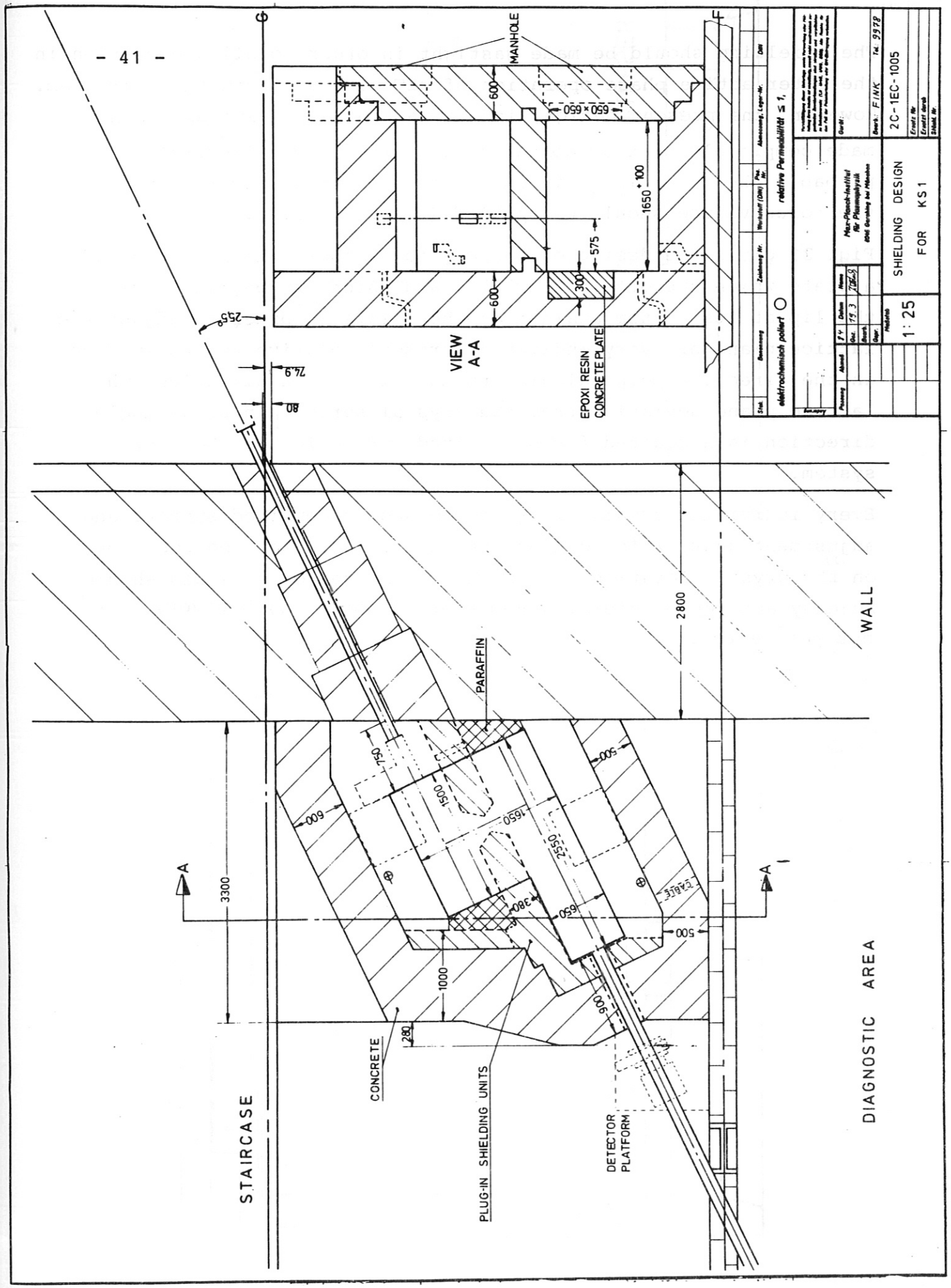

Fig. 20 Double crystal monochromator shielding design

The shielding should be made gastight in order to allow operation in the later active phase operation of JET with application of tritium. However, the present design, including the vacuum system, is not made completely tritium compatible. In this mode of operation probably the thin Al_2O_3 windows to separate the spectrometer from the torus volume should be applied (see chap. 3.3).

Fig. 21 gives the design of the crystal holder, which is made of a plate which supports the crystal and which can be tilted via the lip at its bottom against another plate in order to adjust the lattice plane of every individual crystal relative to its surface in the direction perpendicular to the dispersion direction. The lattice plane deviation from the crystal surface in Bragg angle direction is accounted for by a fixed correction in the control system.

Every individual crystal is fixed to such a combined support and adjustment unit, which can be attached at well defined position on the crystal rotation tables. Hence changes of crystals should be easy and reproducible. These crystal supports, however, are not yet tested.

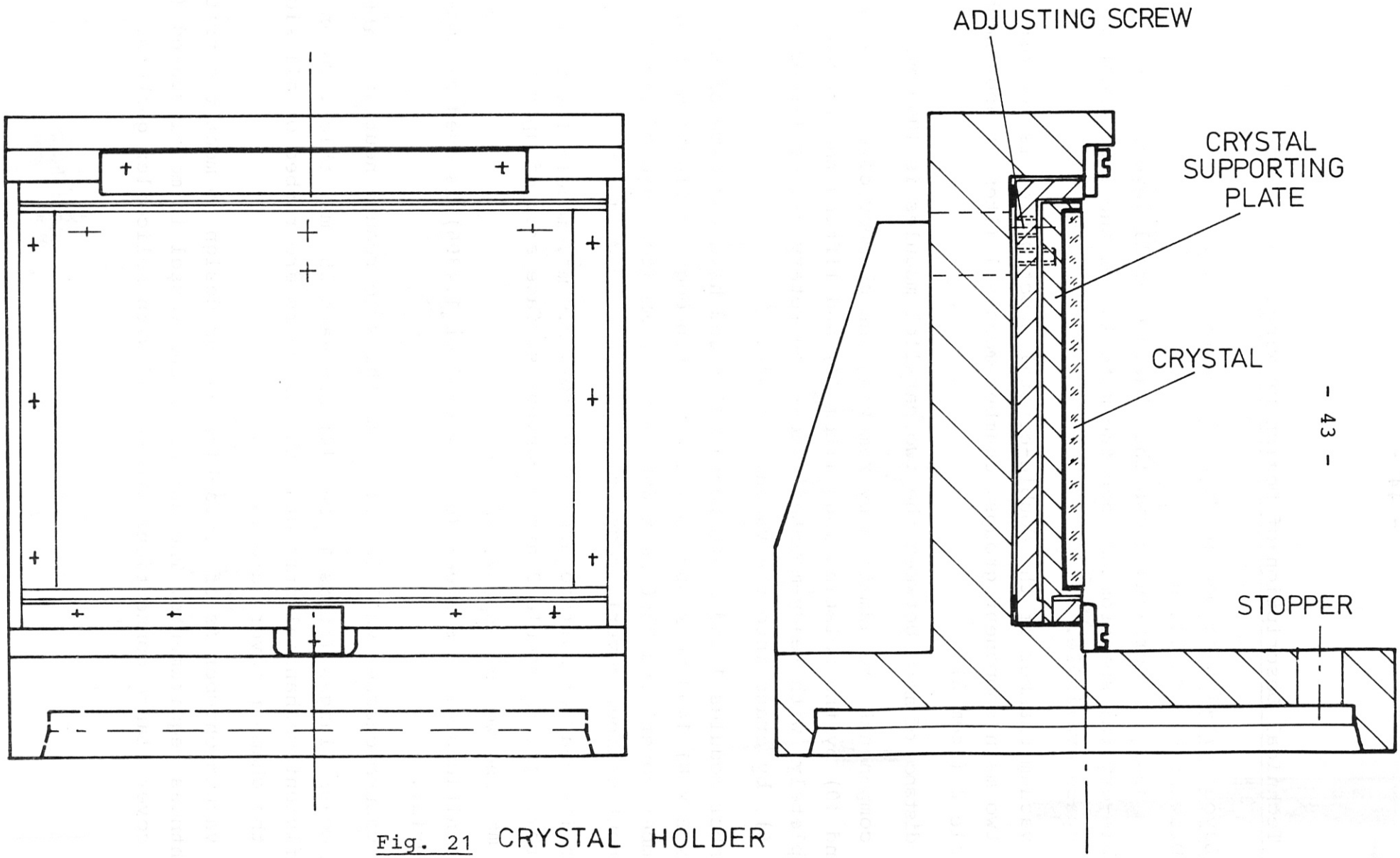

Fig. 21 CRYSTAL HOLDER

M 1:1

4.2 Technical Description of Design Drawings

1. Layout drawing of Double-Crystal Spectrometer

Drawing No. PH 500 020

The design drawing shows the basic overall layout of the double-crystal spectrometer and the matching of the instrument to the space available.

The vacuum chamber of the double-crystal spectrometer is composed of the two main component groups, chamber module 1 (item 1) and chamber module 2 (item 2).

The distance of axes between the two parallel modules is 1000 mm.

The components are admitted by removing the chamber covers (items 9 and 10) by the hoisting lugs (item 11) and lifting the tracks completely, with ready-mounted linear and rotary drives (items 5 and 6), by crane into the vacuum chamber.

Chamber modules 1 and 2 are rectangular and have the dimensions (L x B x H) 1450 mm x 600 mm x 650 mm (top edge of flange without chamber cover) and 2500 mm x 600 mm x 650 mm (top edge of flange without chamber cover), respectively.

With its chamber surface area of approx. 2.9 m^2, module 1 weighs approx. 350 kg module 2 has a chamber surface area of approx. 5.1 m^2 and weighs approx. 600 kg.

Austenitic stainless steel (e.g. 1.4301 or 1.4306) is used as chamber material.

The vacuum chamber wall is only 5 mm thick to reduce neutron scattering.

The cover flanges (items 13 and 14) are each 25 mm thick. To ensure sufficient mechanical strength, the chambers are ribbed on all sides and the chamber covers are vaulted.

The vacuum chamber is of ultra-high vacuum design to meet the tritium tightness requirements. The entire vacuum vessel is metal-sealed (CF). The cover flange connections are sealed with Helicoflex gaskets.

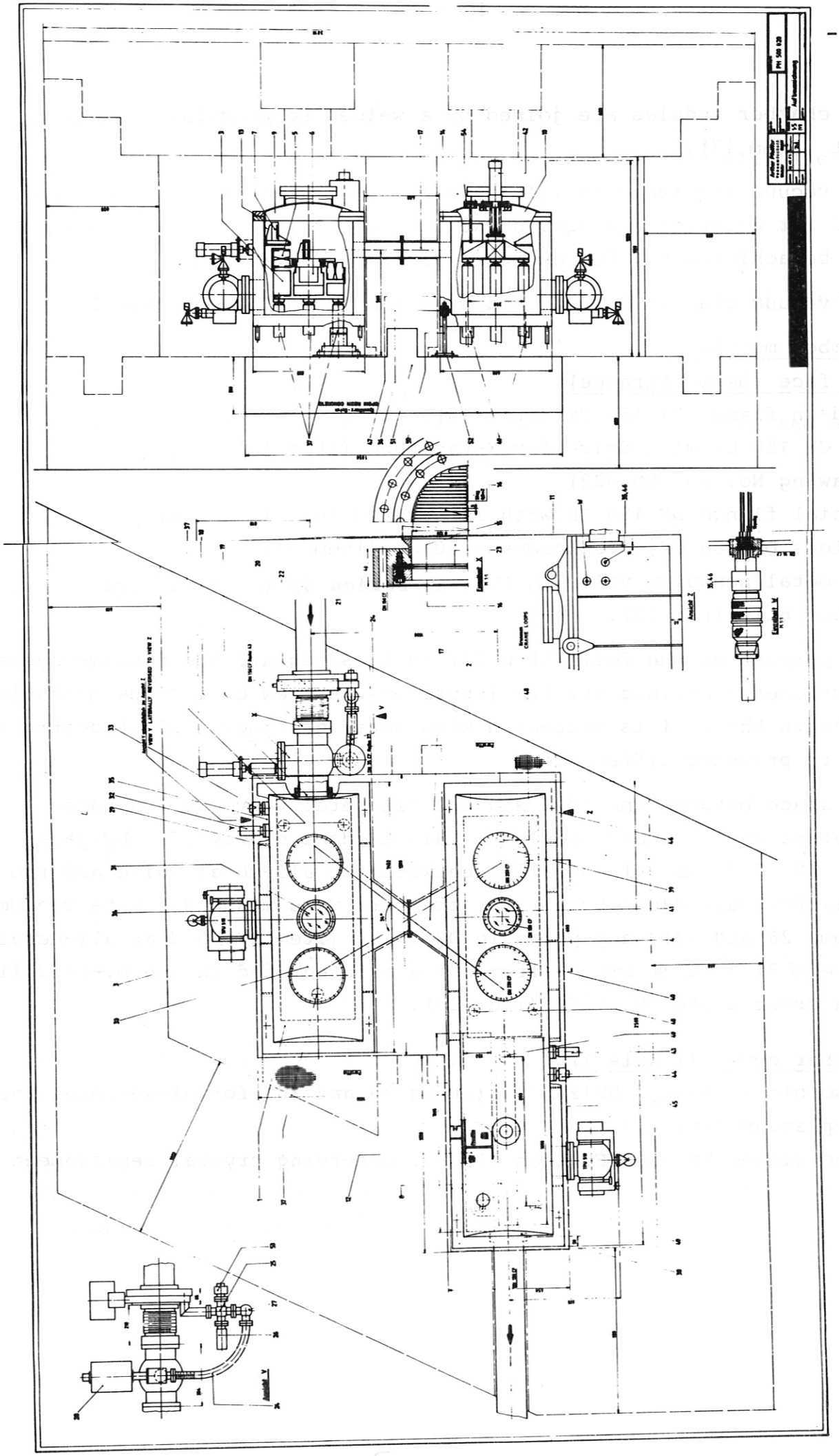

Fig.22 Layout of double crystal monochromator

The chamber modules are joined by a welded rectangular connecting duct (item 17).

The vacuum requirements (ultimate pressure less than 1 x 10^{-6} mbar) call for a surface quality of N8 DIN ISO 1302 (R_a = 3.2 µm), which can be achieved by, for example, glass bead blasting.

The vacuum chamber is provided with the following components:

Chamber module 1

End face (beam entrance)

Weld-in flange CN 150 CF (item 18)
Tee CN 150 CF with drive for X-ray tube (item 19)
(drawing No. PH 500 022)
Special flange DN 150 CF with integrated foil (item 20)
Bellows DN 150 CF, displacement 50 mm (item 21)
All-metal pendulum valve DN 150 VAT **series** 43 (JET-standard component) (item 22).

The purpose of the foil (item 23) is to safeguard the double-crystal spectrometer against tritium incursion. In view of its low mechanical strength the foil is protected with metal gratings against destruction due to pressure differences.

The space between the foil and the all-metal valve is evacuated together with chamber module 1. This is done by way of a by-pass line DN 35 (item 24) installed between the all-metal valve and the foil. Pressure gauge points for the fore vacuum and ultimate vacuum (items 26 and 53), a pipe angle DN 35 CF (item 27) and an all-metal valve DN 35 CF VAT series 37 (item 28) are integrated in the by-pass line on a cross-piece DN 35 CF (item 25).

Chamber cover (module 1)

+ Two blank flanges DN 250 CF (items 29 and 30) for glove-boxes for replacing crystals
+ One window DN 150 CF (item 31) for observing crystal replacement

Chamber side-wall (module 1)

+ Two vacuum gauge tubes each for the fore vacuum and ultimate vacuum DN 35 CF (items 32 and 33)
+ One flange DN 150 CF for tritium-compatible turbomolecular pump (item 34)
+ Three weld-in flanges DN 16 CF for current lead-throughs (item 35)
  Four lugs for chamber suspension (item 36)

Chamber base (module 1)

+ Three weld-in flanges DN 100 CF (item 37) for admitting the adjustable bearing supports for the cast track

Chamber module 2 comprises the following components:

End face (beam exit)

+ One weld-in flange DN 150 CF (item 38)

Chamber cover

+ Two blank flanges DN 250 CF (items 39 and 40)
  for glove-boxes for crystal replacement
+ One window DN 150 CF (item 41) for observing crystal replacement
+ One motion feed-through for collimator (item 42)
  drawing No. PH 500 023
+ One blank flange DN 35 CF with anti-torque rod for collimator

Chamber side-wall (module 2)

+ Two vacuum gauge tubes for ultimate vacuum DN 35 CF (item 4)
+ One flange DN 150 CF for tritium-compatible turbomolecular pump (item 45)
+ Three weld-in flanges DN 16 CF for current lead-throughs (item 46)
+ Four lugs for chamber suspension (item 47)

Chamber base (module 2)

+ Three weld-in flanges DN 100 CF (item 48) for admitting the adjustable bearing supports for the cast track

+ Three weld-in flanges DN 100 CF (item 49) for admitting the adjustable bearing supports for the collimator.

The vacuum chambers are suspended from a total of eight mounting pillars (item 50, four per chamber module), each of which is bolted to four support plates (item 52) integral-cast in an epoxy resin concrete plate with an accuracy of ± 2 mm relative to one another. The individual vacuum chambers are positioned by crane and then connected together by lip welding.

The tracks are lowered from above into the individual modules. They each rest on three support points located in the chamber. The tracks can be adjusted with bellows. The mechanical system of the instrument is thus independent of the chamber and hence largely unaffected by forces.

The tracks are adjusted on the atmosphere side, this also being possible in the evacuated state of the chamber. The tracks are designed to allow adjustment in any plane required. All settings can be locked (drawing No. PH 500 024).

2. Cross-section of module 1

Drawing No. PH 500 021

Cross-section of tracks

Drawing No. PH 500 025

Drawing No. PH 500 021 shows a cross-section of chamber module 1 (item 1) with the components required for operating the instrument.

Drawing No. PH 500 025 affords a side view (cross-section) of the tracks. The cross-sectional view at the top indicates the line of sight.

Cross-section of module 1

Drawing No. PH 500 021

In view of the high level of mechanical accuracy required of the instrument the track (item 2) plays a special role. To meet the conditions specified, the tracks have to afford a parallelism of 2 µm (for a length of 1 m). Sagging of the tracks in the longitudinal direction ought not to exceed a value of 3 µm.

The tracks are made of high-grade spheroidal graphite cast iron (GGG 60) because of its high form stability and excellent oscillating damping properties. To ensure UHV compatibility, the tracks are subjected to surface treatment after mechanical processing. The outer dimensions (L x B x H) of the tracks are 1080 x 410 x 285 mm (with crystal, item 3, 320 mm).

Without the carriage (item 4), crystal and stainless-steel rails, the tracks weigh approx. 180 kg.

The carriage runs on chromium-plated stainless-steel rails which are mounted on the ground guideways of the cast tracks.

The sapphire or ruby ball bearings (item 6) are spaced in a cage (item 7) made of silver-plated aluminium F52. The design of the carriage guideway is such that a stainless-steel rail (item 9) affords the carriage a degree of freedom in the transverse direction.

The longitudinal motion of the carriages is accomplished by means of a total of 20 double inductor combs (item 10, ten per module) fitted

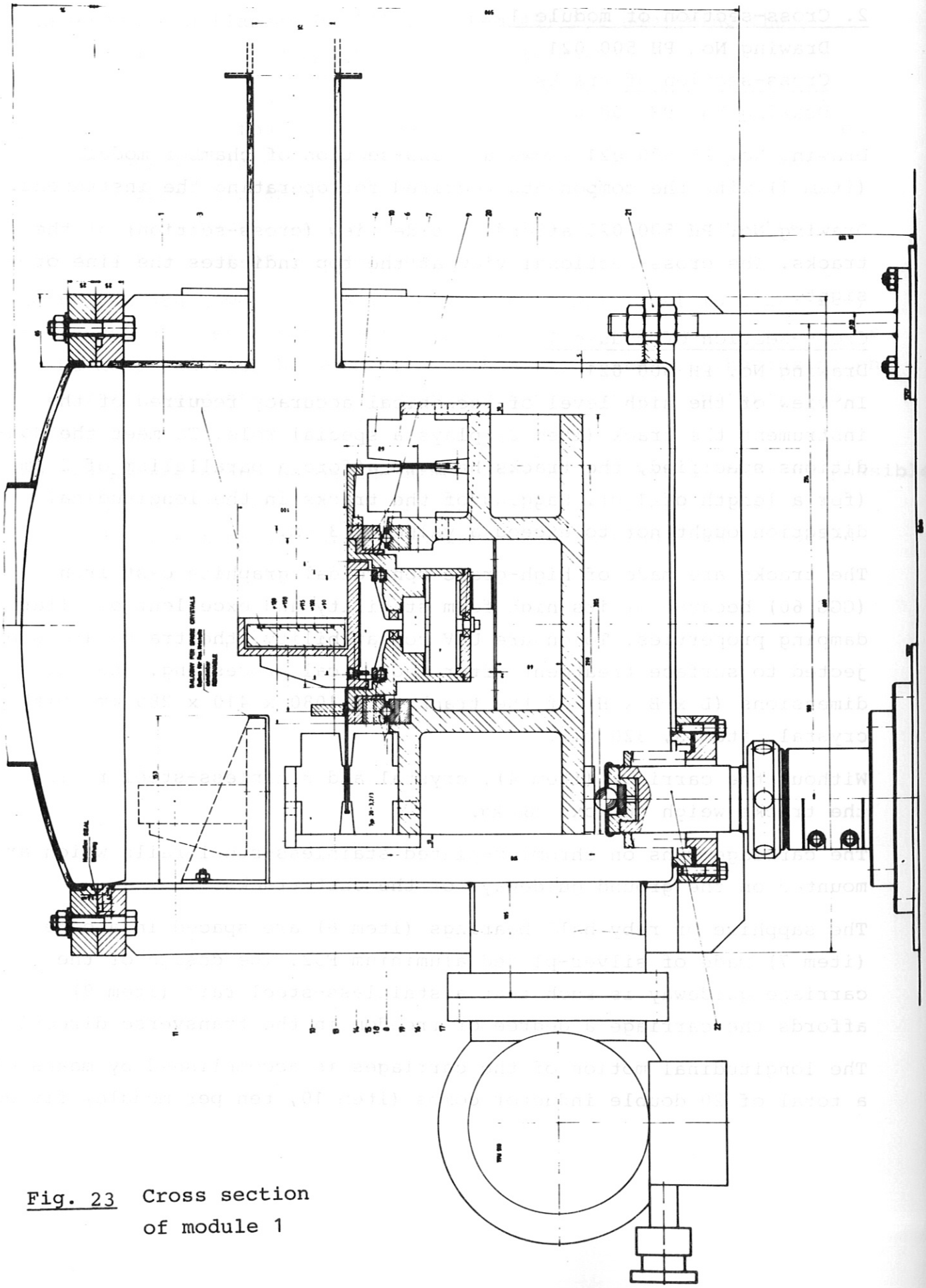

Fig. 23 Cross section of module 1

to the tracks. The displacement of a carriage is 760 mm. This length is passed through 8 times (4 forward and backward motions) in approx. 10 seconds.

The carriage dimensions are (L x B x H) 300 mm x 185 mm x 210 mm (including crystal and rotary drive). The maximum permissible tolerance of the carriage guideway is 7.2 µm in the longitudinal direction and 4.4 µm in the transverse direction.

The acceleration and deceleration phases of a carriage are each 0.1 second. The turning points of the oscillating motion of the carriage on the track are achieved with a repetition accuracy of ± 1 mm. The mechanically non-coupled motions of the two carriages run synchronously, with the deviation in position not exceeding 2 mm.

The forces of the linear motor act on the carriages in such a way that the generation of tilting moments is avoided. This is done by arranging the double inductor combs so that the drive forces are exerted as close as possible to the centre of mass of the carriage.

The inductor combs are insulated with kapton to make the linear motor vacuum-compatible (working pressure approx. 1×10^{-6} mbar).

The linear drive is done with a fully controlled thyristor with electronic reversal. Both linear motors are actuated by a drive controller.

Each carriage is topped with a complete swivel mount. Each swivel mount is composed of the crystal holder (item 13) including the crystal, a central mount (item 14), the turntable (item 15), the torque motor (item 16), and the multipole resolver (item 17).

The mass of the crystal, including the holder is assumed to be 2 kg, moment of mass inertia to be $2.5 \cdot 10^{-4}$ Nm^2.

The swivel mount covers an angular range from 30° to 64° within one second. The angle can be measured with a resolution of 2^{19} in relation to the full circle. The maximum deviation of the two crystal surfaces from the parallel setting is max. 6 seconds of arc.

The crystals mounted in the holder are set up on the central mount and adjusted. To replace the crystal, the central mount is removed and a new reserve crystal (item 11) is mounted on the turntable free of play and torque. The turntable and central mount are finished to an accuracy of 10 µm in their contact dimensions (100 mm in diam.). Three mounting threads and a set pin are provided for fastening.

The turntable is provided with three bearings: an axial bearing (item 18) which supports the entire turntable, a radial bearing (item 19) for centring, and at the lower end of the shaft an angular contact ball bearing (item 20) which takes up both axial and radial loads. The angular contact ball bearing is prestressed to compensate the bearing clearance.
The maximum permissible vertical angular deviation of the crystals is 5".
The rotary drive is done with a torque motor, the angle of rotation being determined with a digital resolver. The torque motors are operated by way of servo amplifiers which provide four-quadrant setting of the angle of rotation. All servo amplifiers are controlled from a common central unit, the set point of the linear motion of a carriage serving as reference value for all other quantities. The positional values are scanned and reset within 1.4 ms.

The control system is shown in the attached block diagram.

The chamber suspension is already explained under point 1 of the Technical Description features as item 21.

Item 22 shows one of three different track setting possibilities that were explained in detail under point 5 of the Technical Description.

Cross-section of tracks

Drawing No. PH 500 025

To investigate a certain wavelength, the crystal has to be fixed in a given position. The carriage is fixed in a prescribed position by actuating a mechanical brake rail (items 1-4) which is opened and

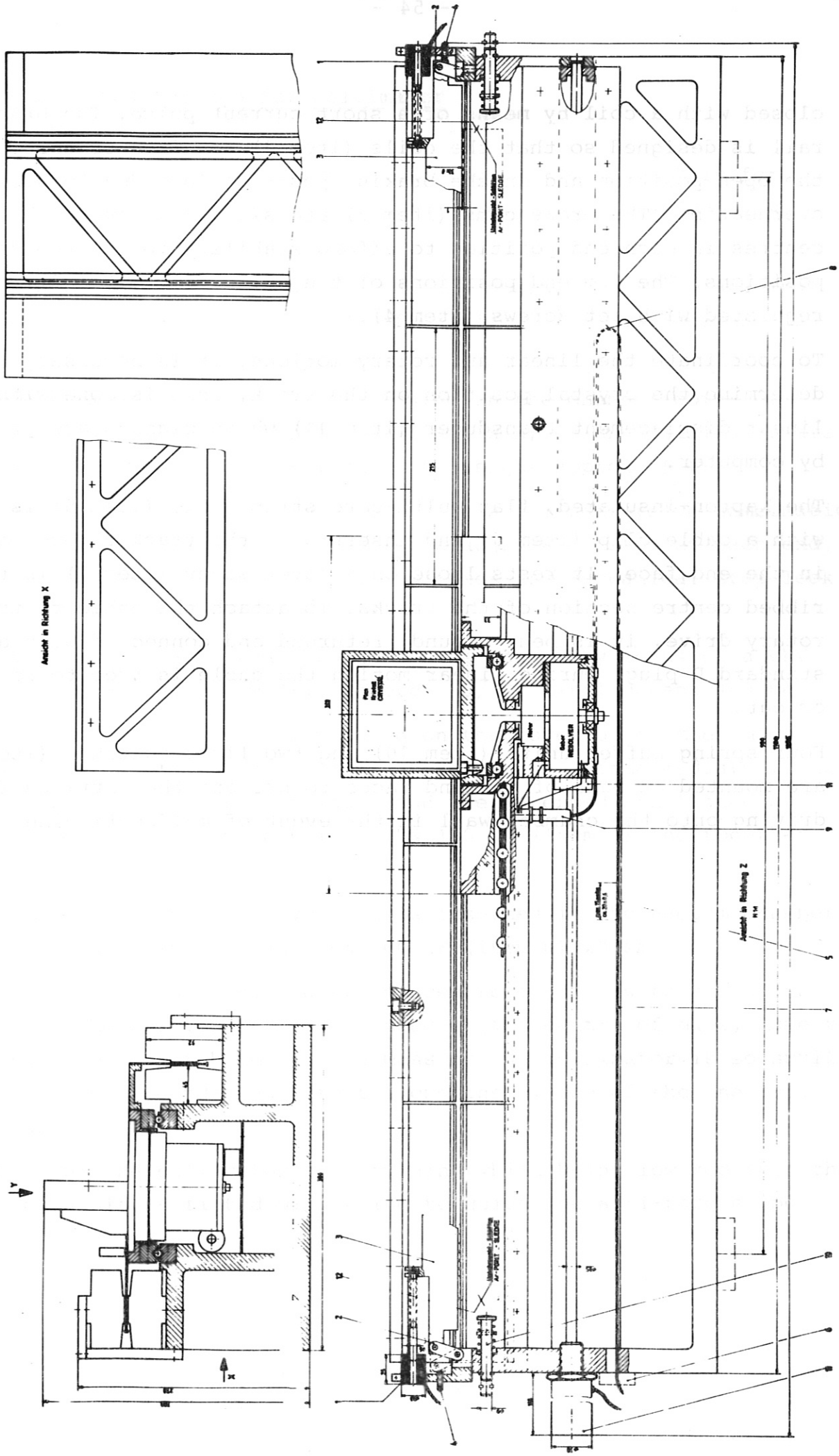

Fig. 24 Cross section of tracks

closed with a coil by means of a short current pulse. The brake rail is designed so that the coils (item 1) are free of current in the open position and in the braking position in order to avoid overheating. The brake cams (item 2) are swivelled beyond the dead centres in each end position to afford stability in the two end positions. The two end positions of the brake rail (item 3) are regulated with set screws (item 4).

To coordinate the linear and rotary motions, it is necessary to determine the crystal position on the track. This is done with a linear displacement transducer (item 11) whose signals are processed by computer.

The kapton-insulated, flat multi-core strip cable (item 5) is secured with a cable clip (item 6) and inserted in the track through a slit in the end face. It rests loose on a cover sheet (item 7) in the ribbed centre section of the tracks. To attach the cable to the rotary drive, it is bent around, returned and connected with a 15-pin standard D-plug. During linear motion the cable is free to roll up or out.

Four spring buffer units (item 10) and two limit switches (item 12) are mounted at each of the end faces to prevent the carriage from driving onto the chamber wall in the event of malfunctioning.

3. Motion feed-through for collimator

Drawing No. PH 500 023

The motion feed-through shown in drawing No. PH 500 023 is for shifting a collimator (item 1) into or out of the beam path as required.

The collimator is shown in both the top position (LHS of drawing) and in the bottom position (RHS of drawing). The displacement is 100 mm.

The collimator feed-through is located in the chamber cover of chamber module 2. The dimensions (L x B x H) of the collimator are approx. 1000 mm x 100 mm x 100 mm; it weighs approx. 5 kg.

The drive is pneumatic and is done with a cylinder-valve combination (item 2), piston diameter 50 mm, with adjustable stop at each end, non-return throttle valve, limit switches and mechanical stop lock at one end.

The linear motion is fed through to the vacuum by means of a UHV diaphragm bellows (item 3), diameter 58/39, displacement 100 mm.

The motion feed-through is mounted on the cover of chamber module 2 by means of a pneumatic cylinder attached to an intermediate flange (item 4). The pneumatic cylinder and the intermediate flange are bolted to a special blank flange DN 100 CF (item 5) and together comprise the drive unit.

For space reasons the drive unit is inserted in the vacuum chamber on a special weld-in flange DN 100 CF (item 6) 20 mm.

The collimator is connected at its centre of mass with the drive unit. As the collimator is suspended at its centre of mass, moments are ruled out. Furthermore, the mass of the collimator is so small that it can be conducted direct along the piston of the pneumatic cylinder.

To prevent the collimator from turning while being lowered into the beam path, it is fitted with a lug to guide the anti-torque rod

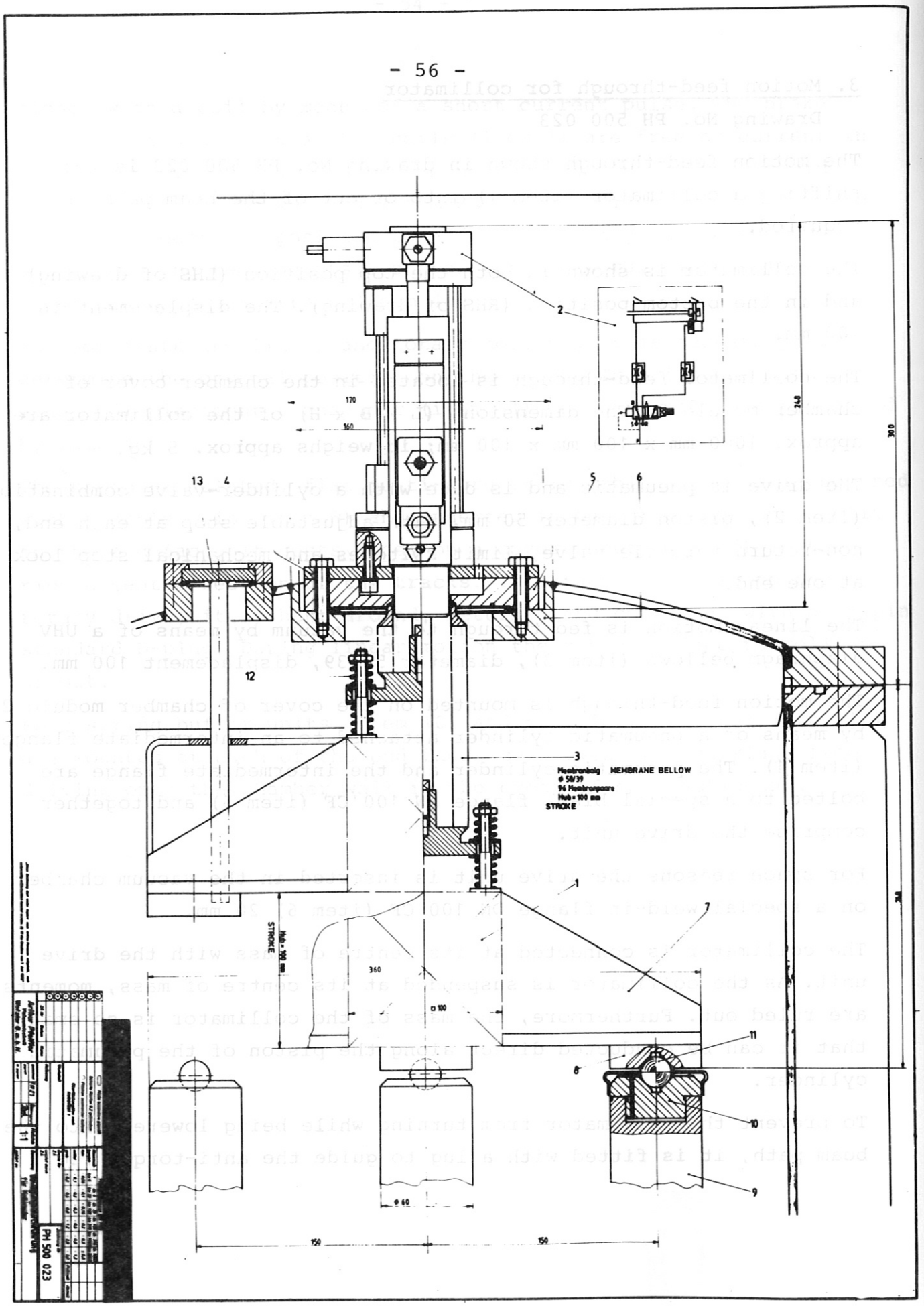

Fig. 25 Motion feed-through for collimator

(item 13). The guide lug is provided with a slit and the anti-torque rod is welded to a rotatable blank flange DN 35 CF allowing the anti-torque rod to be fitted to the collimator position.

Exact positioning of the collimator is done by means of a three-point base. By means of two consoles (item 7) and a bearing plate (item 8) the collimator is lowered on three uprights (item 9) to rest on three sapphire ball bearings (item 11) cradled in surface hardened bushings (item 10).

The uprights are admitted to the vacuum by way of diaphragm bellows and allow adjustment outside the vacuum in all directions. The adjustment possibilities are illustrated and described in detail in drawing No. PH 500 024 and under point 1.5 of the Technical Description, respectively.

To ensure the smoothest possible lowering and lifting of the collimator, a spring system composed of four compression springs (item 12) is to be placed between the collimator and the motion feed-through. The spring system is designed so that the collimator, when extended, is always pushed into the three-point base under slight pressure, thus ensuring proper fixation of the collimator.

4. Tee with drive for X-ray tube

Drawing No. PH 500 022

The motion feed-through shown in drawing No. PH 500 022 is for shifting an X-ray tube into or out of the beam path as required.

The drawing shows the X-ray tube in the retracted position.

The X-ray tube is integrated in a tee DN 150 CF (item 1). A flange CN 35 CF for attaching the by-pass valve is provided on the side opposite the drive.

The drive is pneumatic and is done with a cylinder-valve combination (item 5), piston diameter 50 mm, with adjustable stops at each end, non-return throttle valve and mechanical stop lock at one end.

The vacuum is sealed by way of a UHV diaphragm bellows (item 3).

The drive with the motion feed-through and current feed-throughs (item 7) are mounted on a blank flange (item 2) DN 150 CF to allow removal of the complete unit.

The X-ray tube is positioned exactly in the beam path by means of spacer bolts (tiem 9) and nuts (item 10).

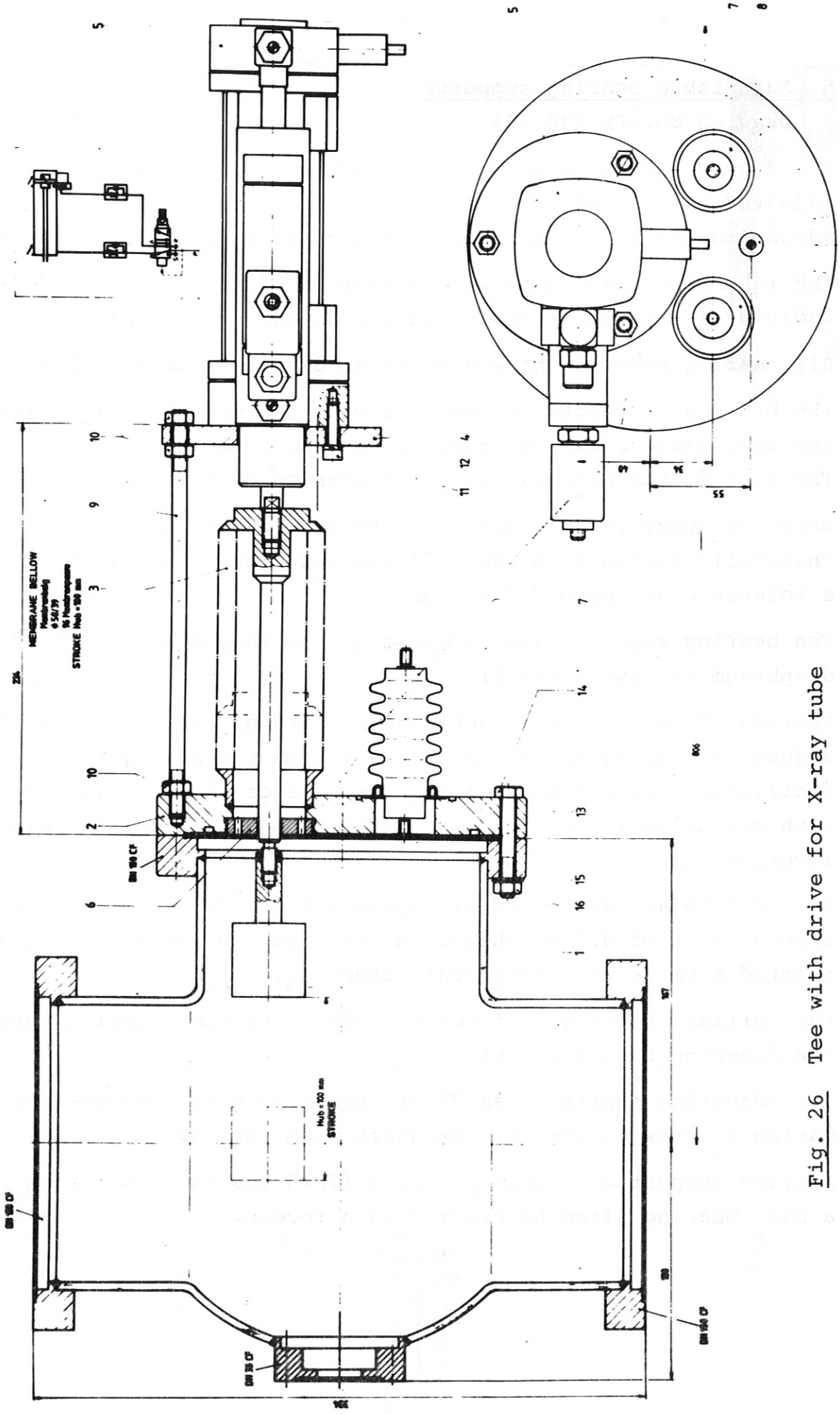

Fig. 26 Tee with drive for X-ray tube

5. Adjustable bearing supports

Drawing No. PH 500 024

The drawing shows how the tracks are adjusted. (The collimator is adjusted on the same principle, the only difference being the longer adjusting shafts (item 7) and the different spacing between the bearings.

The schematic drawing shows the degrees of freedom possible for the individual bearing supports and the actual spacing between the bearings.

All bearing supports have a vertical displacement of ± 5 mm.

The bearing supports are secured with the mounting plate (item 2) on the base plates (item 4) cast in the epoxy resin concrete plate (item 3). The base plates are cast with a precision of ± 2 mm.

Once the epoxy resin concrete plate has set the base plates are mechanically finished so that all the mounting holes can be bored with a tolerance of approx. ± 0.1 mm.

The bearing supports are admitted to the vacuum chamber by way of diaphragm bellows (item 5).

Vertical displacement is achieved by turning the copper-beryllium adjusting ring (item 1), which has a fine thread M60 x 0.5. To facilitate vertical adjustment, the edge of the ring is provided with six holes (15 mm in diam.) to accommodate a rod acting as a levering arm.

In order to achieve vertical adjustment of, for example, 1 µm at the thread pitch of 0.5 mm chosen, a levering arm 500 mm long has to be shifted 6 mm in the peripheral direction.

The vertical setting is fixed by tightening the clamping screws in the clamping ring (item 6).

The adjusting shafts (item 7) are provided with a groove for accommodating a screw to prevent the shaft from turning.

Bearing support 1 is designed as a fixed bearing. The track rests on a ball bearing (item 8) cradled in a recess.

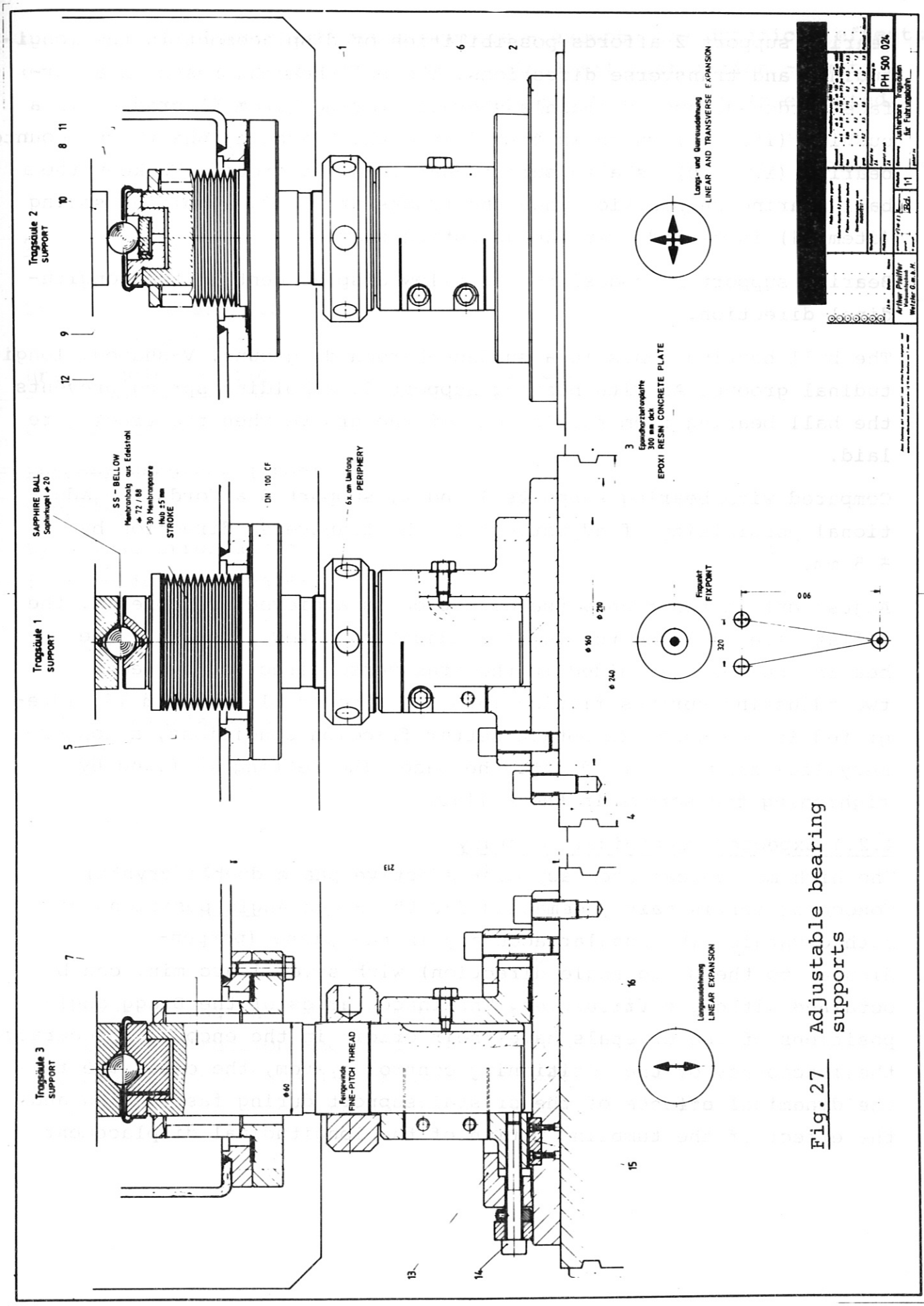

Fig. 27 Adjustable bearing supports

Bearing support 2 affords possibilities of displacement in the longitudinal and transverse directions. The ball bearing rests on a surface-hardened, ground stainless-steel bearing (item 8) cradled in a bushing (item 12) which is fitted into the adjusting shaft. The counter bearing (item 10) is also surface-hardened and ground. To keep the ball bearing in position when the tracks are laid, a holding spring (item 11) is fitted over the adjusting shaft.

Bearing support 3 is designed to allow displacement in the longitudinal direction.

The ball bearing rests in a surface-hardened, ground, V-shaped, longitudinal groove. As with bearing support 2, a holding spring prevents the ball bearing from rolling out of the groove when the tracks are laid.

Compared with bearing supports 1 and 2, support 3 affords the additional possibility of adjustment in the transverse direction by ± 5 mm.

Adjustment in the transverse direction is achieved by loosening the collar (item 13) and turning the adjusting screw (item 14). The bearing support is guided in the transverse direction by means of two adjusting springs fitting into the grooved block (item 15) integrated in the base. To obtain better friction conditions, a copper-beryllium ring is fitted into the base. The setting is fixed by tightening the screws in the collar.

4.2.1 Expected mechanical accuracy

The high mechanical accuracy of the active phase double crystal monochromator is mainly demanded for the Bragg angle positions of both crystals. The angular accuracy in the plane (perpendicular to the Bragg angle direction) with several arc min. can be obtained without difficulties. The inaccuracies of the Bragg angle positions of the crystals have their origin in the encoder inaccuracy, the inaccuracy of the positioning control system, the error due to the dynamical effects of the crystal support during fast motion and the effect of the tumbling motion of the longitudinal displacement

units. For most of these error sources - except the dynamical effects of the crystal support due to the longitudinal fast motion - tests were performed (see sect. 3.1). As described earlier it is expected that the observed inaccuracies can appreciably be reduced. The expected inaccuracies are given in the following table:

Table: Inaccuracies

Error source and its contribution to the Bragg angle position	arc sec
Calibration error:	
Encoder accuracy (Itec)	± 3
Coupling	± 0.5
Dynamical error during fast motion (estimate)	± 2
Position control system inaccuracy (Contraves)	± 2.5
Tumbling motion of longitudinal displacement unit and non-parallelism of tables and collimator misalignment	(± 5)+
Sum	± 8

+ (can be eliminated by calibration)

One crystal together with the collimator defines the soft X-ray acceptance direction and wavelength within this accuracy. Hence the crystal must have a rocking curve width of 20 arc seconds or more. Since the error sums of both crystals might add up (to ± 16

arc seconds in deviation from parallel orientation) the other crystal should be even wider in rocking curve width.

However, line profile measurements would not be excluded by these inaccuracies. In this case the "dynamical error during fast motion" (see table) would not occur. Moreover, the "control system inaccuracy" can be eliminated by measuring the actual positions. Hence only the calibration error of one crystal relative to the collimator (i.e. $\pm$ 3.5 arc seconds) is determining the total accuracy, if one assumes that the other crystal is large enough in its rocking curve width.

4.2.2 Expected monochromator performance

The expected performance of the active phase double crystal monochromator is characterized by the count rate for an impurity spectral line at a certain impurity concentration. As carried out in /3/, the count rate is given by

$$\dot{N} = I \cdot T \cdot S \cdot \frac{h_c}{b} \cdot \eta \ ,$$

where I is the line intensity, T the monochromator transmission (including the geometrical and foil transmission as well as the product of the crystal integral reflectivity R and half the peak reflectivity P(o)/2), S the source area, h_c the crystal height, b the distance of the crystal from the source and η the detector efficiency.

For the He-like Ni XXVII line at λ = 1.59 Å with the transition $1s^1S\text{-}2p^1P$ the intensity is

$$I = 5.2 \cdot 10^{15} \cdot n_{Ni}/n_e \ [\text{photons} \cdot \text{cm}^{-2} \cdot \text{s}^{-1} \cdot \text{ster}^{-1}]$$

where n_{Ni}/n_e is the (relative) impurity concentration of nickel in the JET plasma of typically 100 cm emission length, an electron density of $3 \cdot 10^{13}$ cm^{-3} and a temperature of T_o = 5 keV.

With $T \simeq 8 \cdot 10^{-6}$, $S \simeq 80$ cm^2, h_c = 7 cm, $b \simeq 2000$ cm and $\eta \simeq 0.5$ the count rate is in the order of

$$\dot{N} \simeq 6 \cdot 10^{9} \cdot n_{Ni}/n_e \ [s^{-1}] \ ,$$

which indicates that nickel impurity concentrations can be determined by absolute line intensity measurements even at impurity concentrations much less than $n_{Ni}/n_e = 10^{-5}$.

Similar estimates can be made for other impurity species. For quantitative impurity concentration evaluation the above mentioned calibration has to be performed.

4.3 Positioning control

4.3.1 Positioning elements

For the linear motion a linear induction motor system by DEMAG has been chosen. This system is expected to achieve the required high positioning speed with less angular deviations than the tested device with spindle drive. For position feedback a magnetostrictive position sensor will be used. This system has been chosen because of its small dimensions. The output of this sensor will be converted to 2-phase incremental signals for the position control system and to up-down counting pulses for the real-position recording. For the rotational axes TORQUE motors and CADAM 19 multipole resolvers have been proposed, again because of their small dimensions. The resolvers, however, have two drawbacks: high sensitivity to acceleration and to magnetic fields. New informations about small optical 19 bit encoders from Itec indicate that it may be possible to replace the multipole resolvers by less critical optical devices. The encoder output also will be supplied as 2-phase incremental signals for the position control system and as up-down counting pulses for the real-position recording.

4.3.2 Position control system

The main tasks to be performed by the position control system are the following:

- Rotation of 2 axes by 30^{o} in 1 s with a synchronism of better than 12 arc seconds.
- Nonlinear function (inverse tangent) between the rotation and the motion of the linear axes.
- Handling of the acceleration and deceleration phases.
- Handling of end-switch and reference position signals.
- Remote programming of motion cycles.

Owing to the high real-time requirements and complex tasks to be performed a sophisticated position control system will be necessary. The MANIA control system used for the preliminary tests turned out to be not reliable enough for automatic operation. We now favour the

Contraves system proposed by Pfeiffer. Owing to their experience with military applications Contraves is expected to produce a more reliable solution. A block diagram of the Pfeiffer-Contraves system is given in Fig. 28. The computorized controller has a high position sampling rate of 1 kHz. The 4 axes are controlled by feedback loops via servo amplifiers for the rotational axes and thyristor power controllers for the linear axes.

The nominal values of one linear motion serve as command values for the 4 axes. The motion programmes of the control system are generated by the Simatic interface and loaded to the position controller.

4.3.3 Connection to CODAS

The connection to CODAS is shown in Fig. 35 (see section 4.5). The desired nominal values (limits of Bragg angle scan, constant offset between crystals, scan speed) are transmitted by a 16 bit LSD data line. Additional commands and feedback signals control the data transfer of this line. Other LSD signals are used to define the desired mode of operation (normal scan, line scan, fixed position, crystal exchange, crystal alignment) and provide information about the status of the positioning system (ready, in position, error). The nominal values and commands are translated into motion programmes by the Simatic interface and loaded into the position control system.
The spectrometer scan is started by a CAMAC timer.
During the scan the real position values are stored in a CAMAC memory. For this purpose separate up and down counting lines of each position transducer are connected to 8 inputs of a CAMAC latching scaler. At each load pulse the contents of the scalers (together with the counted detector pulses) is transferred to the memory. The pulse delay during load circuit avoids the loss of position pulses during load. For a sampling frequency of 1 kHz and a measuring period of 10 s 90 KWords have to be stored.

Fig.28 POSITIONING CONTROL FOR DOUBLE-CRYSTAL SPECTROMETER

4.4 Vacuum control

The schematic diagrams of the vacuum system are shown in Figs. 29 and 30 . The vacuum system will be controlled by a Simatic control system in connection with two Edwards controllers (Figs. 31 and 32). The beamline and spectrometer section can be pumped and vented separately. Details of the pumping and venting sequences can be taken from the flow chart Fig. 34 . The symbolic representation of time loops used in this vacuum flow chart are explained in Fig. 33 .

4.4.1 Connection to CODAS

The connection to CODAS is shown in Fig. 35. The vacuum valves measured by the Edwards controllers are passed on to the inputs of a 16-channel CAMAC ADC via analog outputs. Control and feedback signals between CODAS and the Simatic control system are exchanged via LSD. In addition status signals of all vacuum elements are connected to LSD inputs in order to generate a mimic diagram of the vacuum system in the control room.

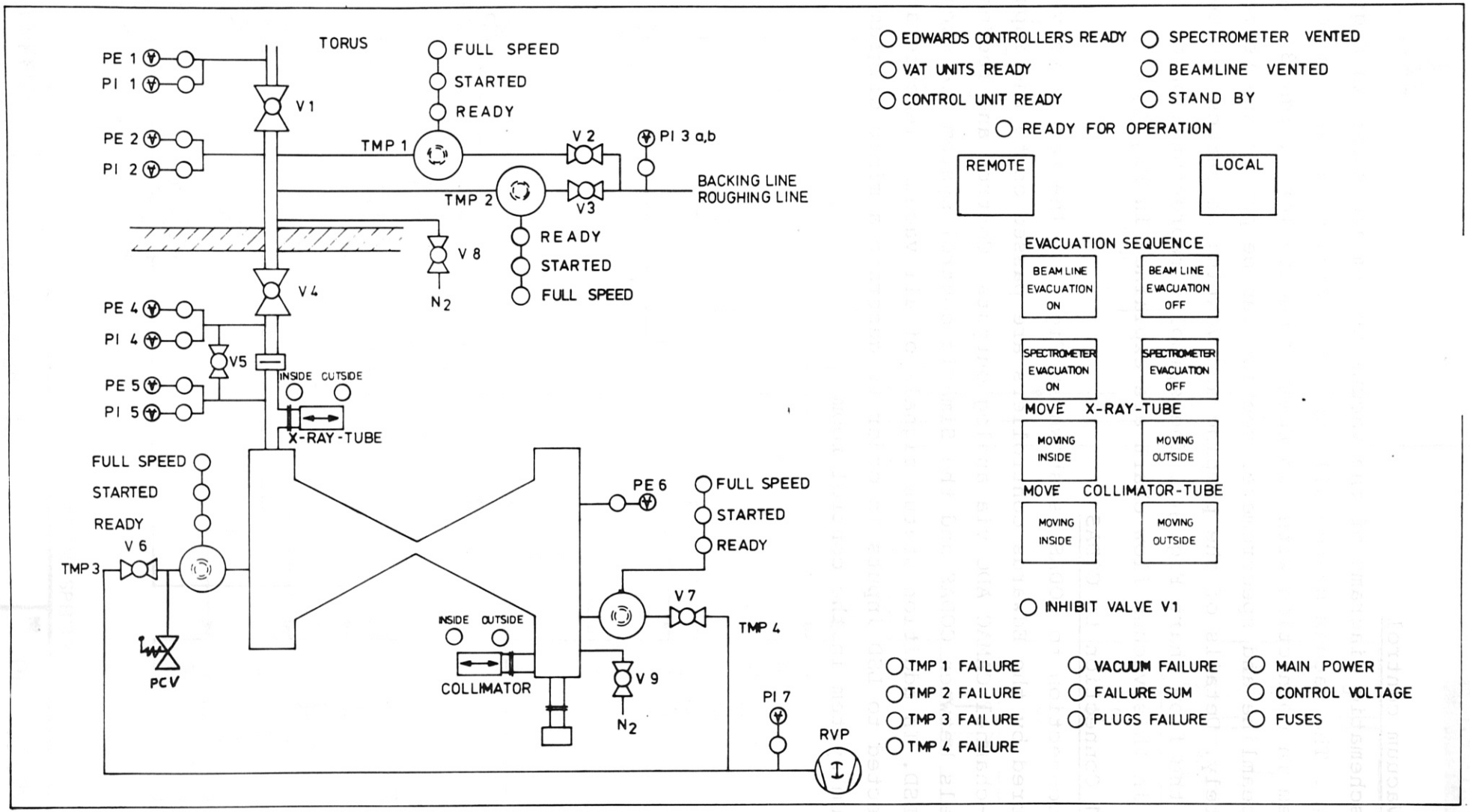

Fig. 29 Vacuum system

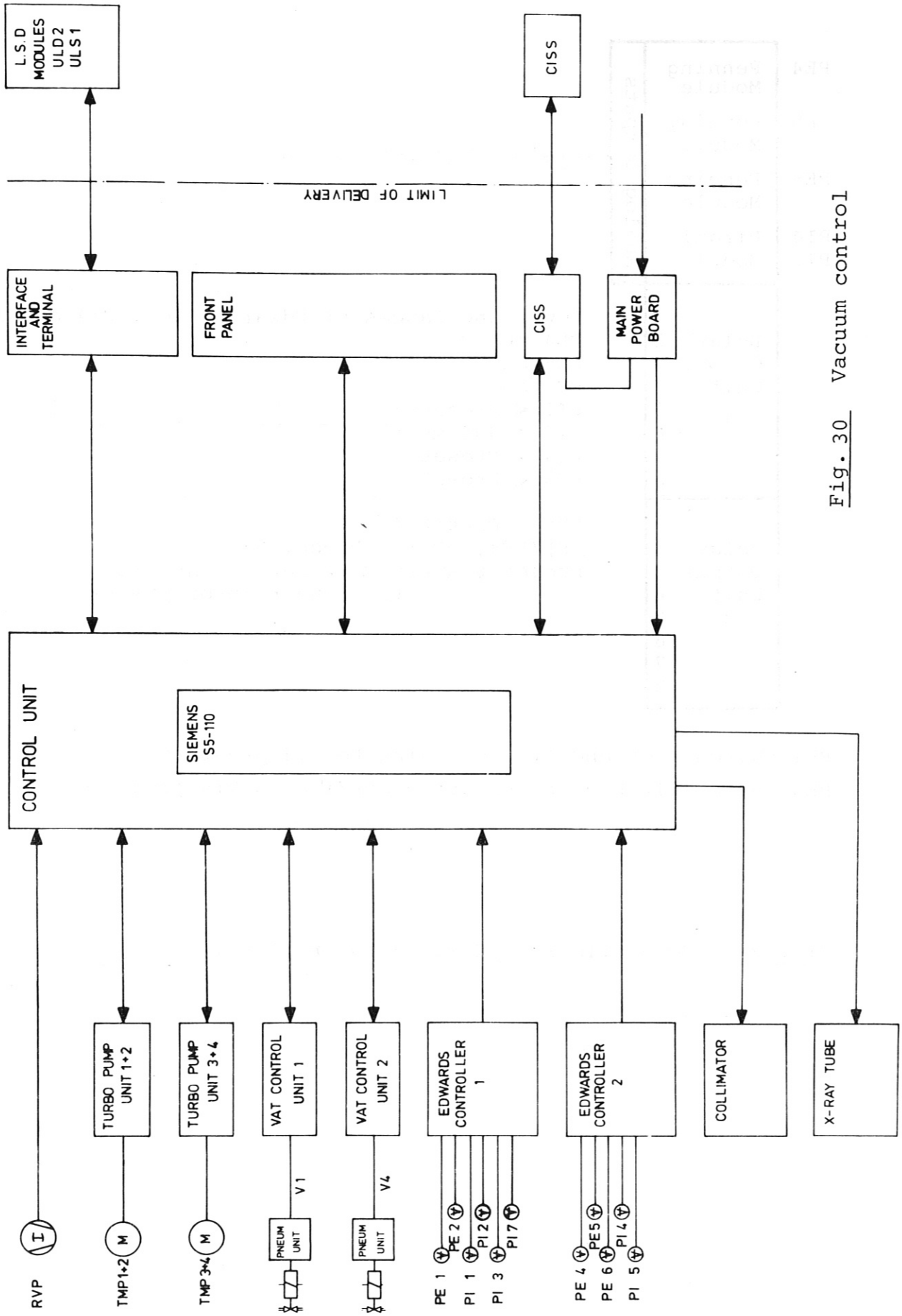

Fig. 30 Vacuum control

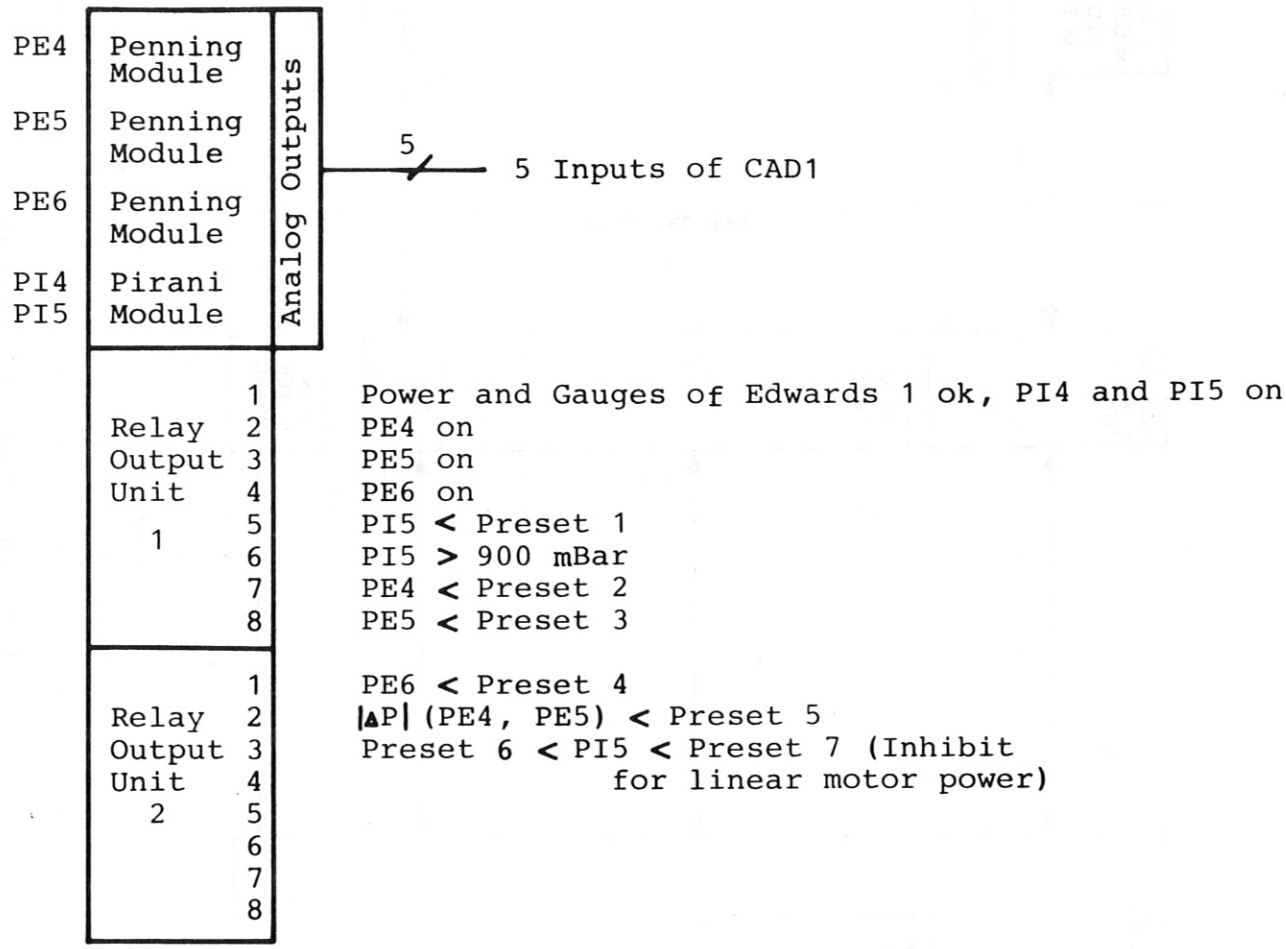

PE4 switched on and off according to PI4 pressure

PE5 and 6 switched on and off according to PI5 pressure

Fig. 31 Connections of Edwards controller 1

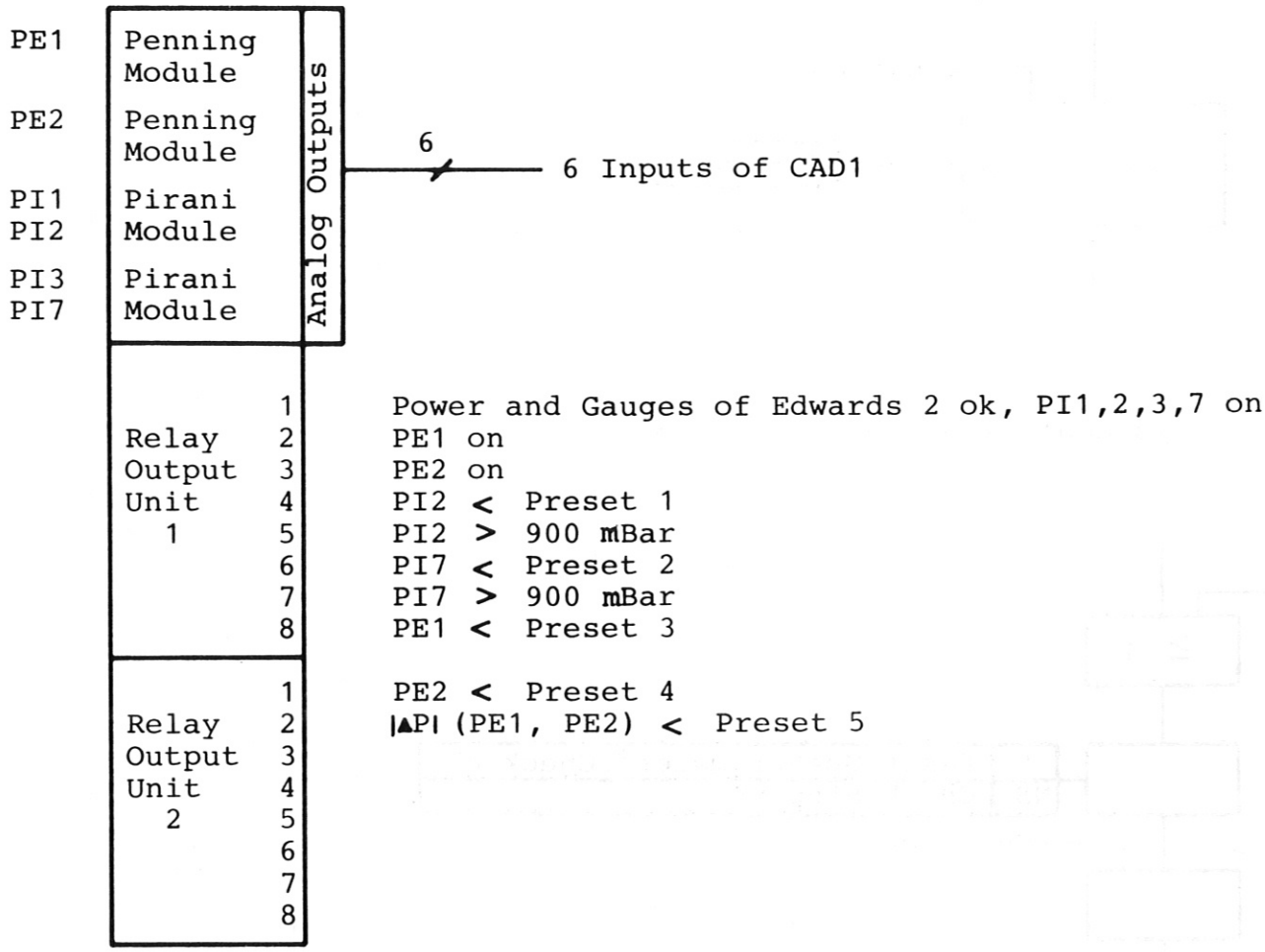

PE1 switched on and off according to PI1 pressure
PE2 switched on and off according to PI2 pressure.

Fig. 32 Connections of Edwards controller 2

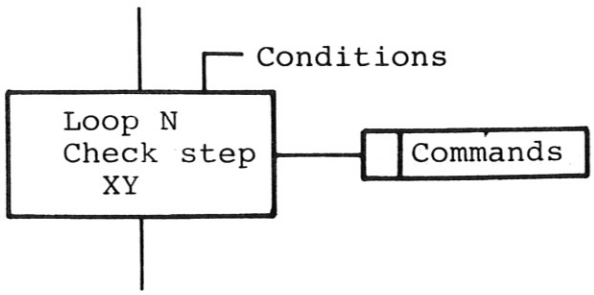

is equivalent to:

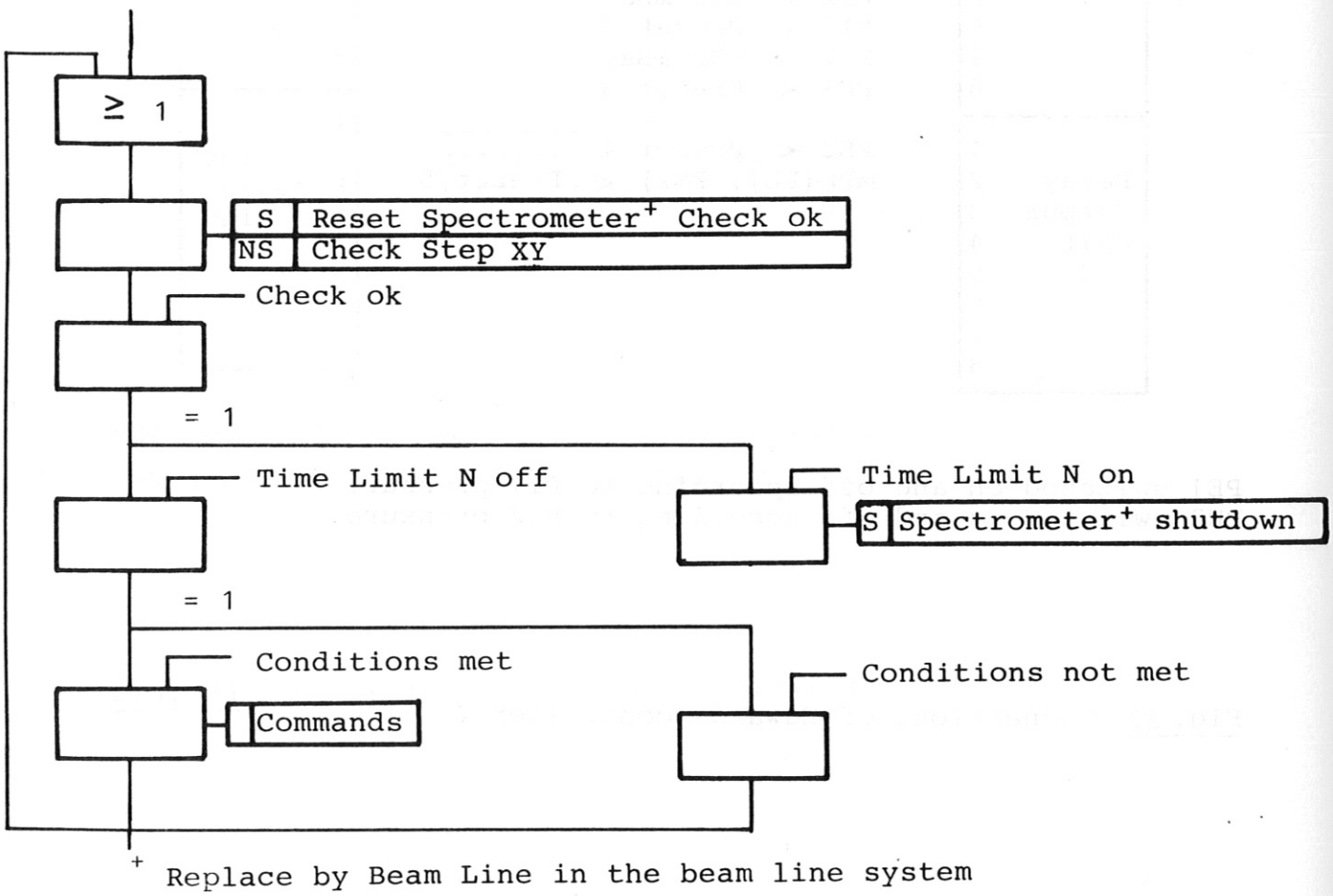

+ Replace by Beam Line in the beam line system

Fig. 33 Explanation of the symbolic representation of time loops used in the vacuum flow chart

1. Select mode of operation

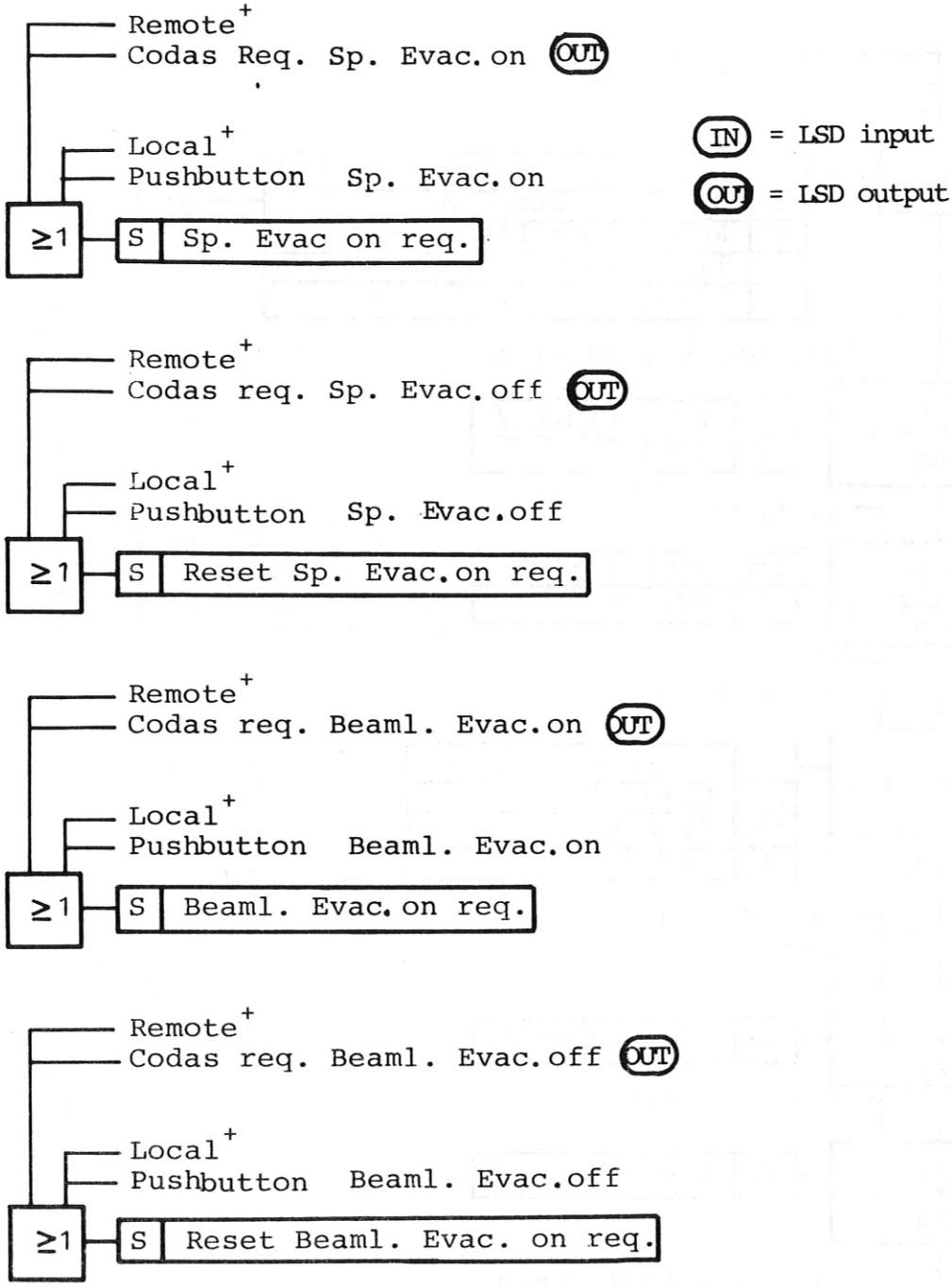

+ Local-Remote interlock according to Codas interface specifications (4 LSD inputs, 2 LSD outputs)

Fig. 34 /1 Flow chart of vacuum control system

2. Spectrometer evacuation

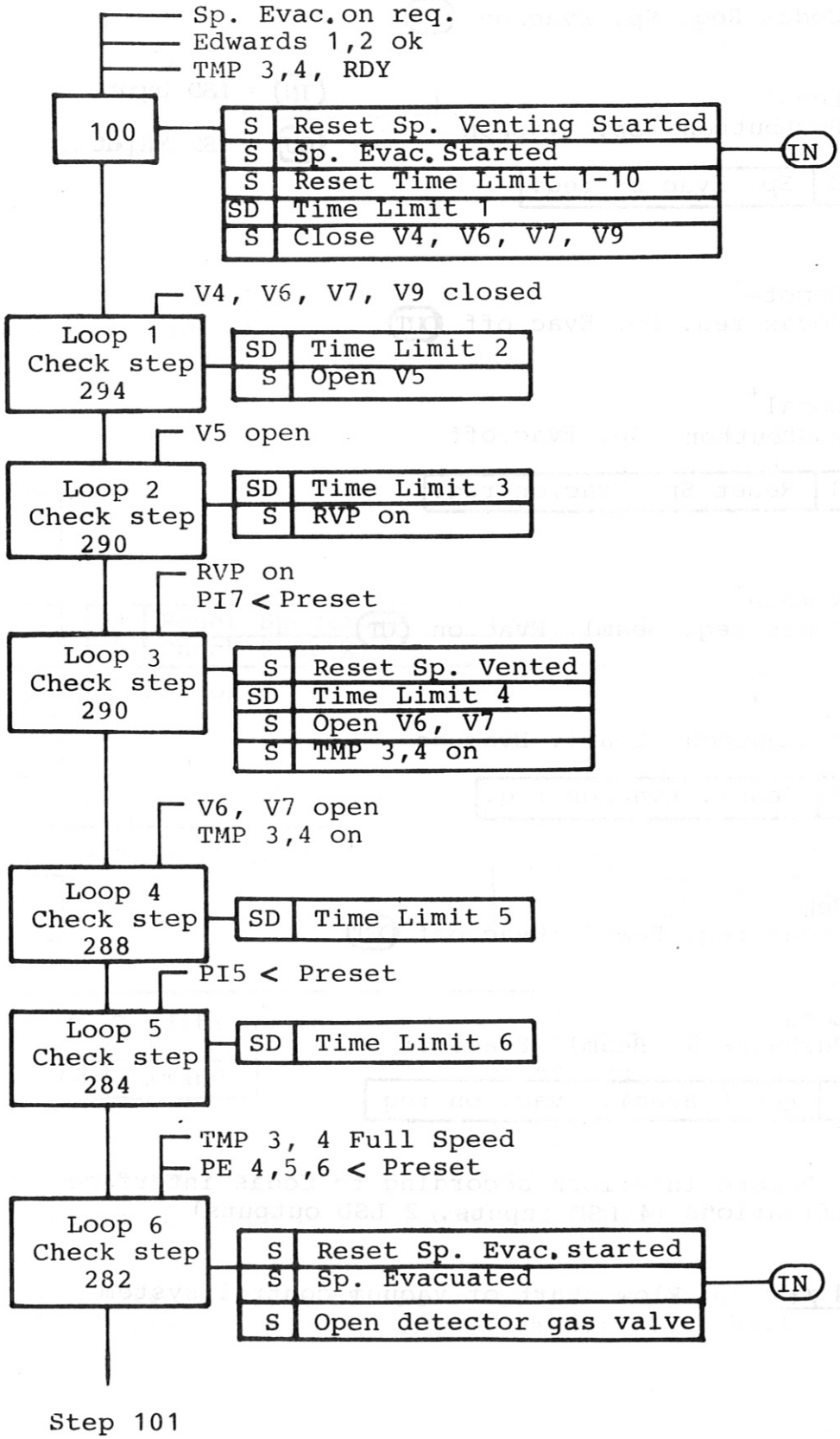

Fig. 34 /2

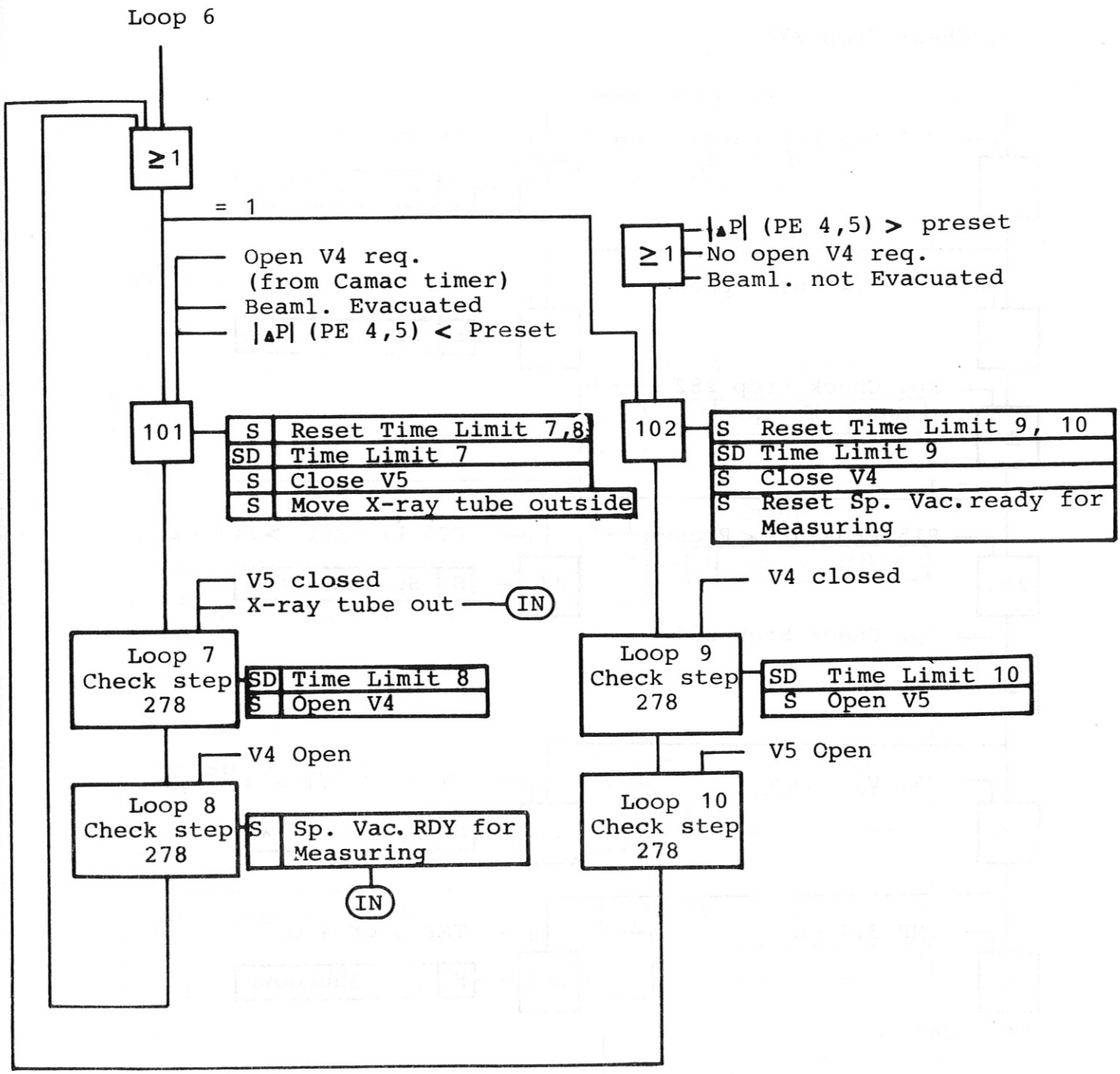
Loop 6
≥1
= 1
Open V4 req.
(from Camac timer)
Beaml. Evacuated
|ΔP| (PE 4,5) < Preset
≥1
|ΔP| (PE 4,5) > preset
No open V4 req.
Beaml. not Evacuated
101
S Reset Time Limit 7,8
SD Time Limit 7
S Close V5
S Move X-ray tube outside
102
S Reset Time Limit 9, 10
SD Time Limit 9
S Close V4
S Reset Sp. Vac. ready for Measuring
V5 closed
X-ray tube out
IN
V4 closed
Loop 7
Check step
278
SD Time Limit 8
S Open V4
Loop 9
Check step
278
SD Time Limit 10
S Open V5
V4 Open
V5 Open
Loop 8
Check step
278
S Sp. Vac. RDY for Measuring
IN
Loop 10
Check step
278

Fig. 34 /3

3. Spectrometer check

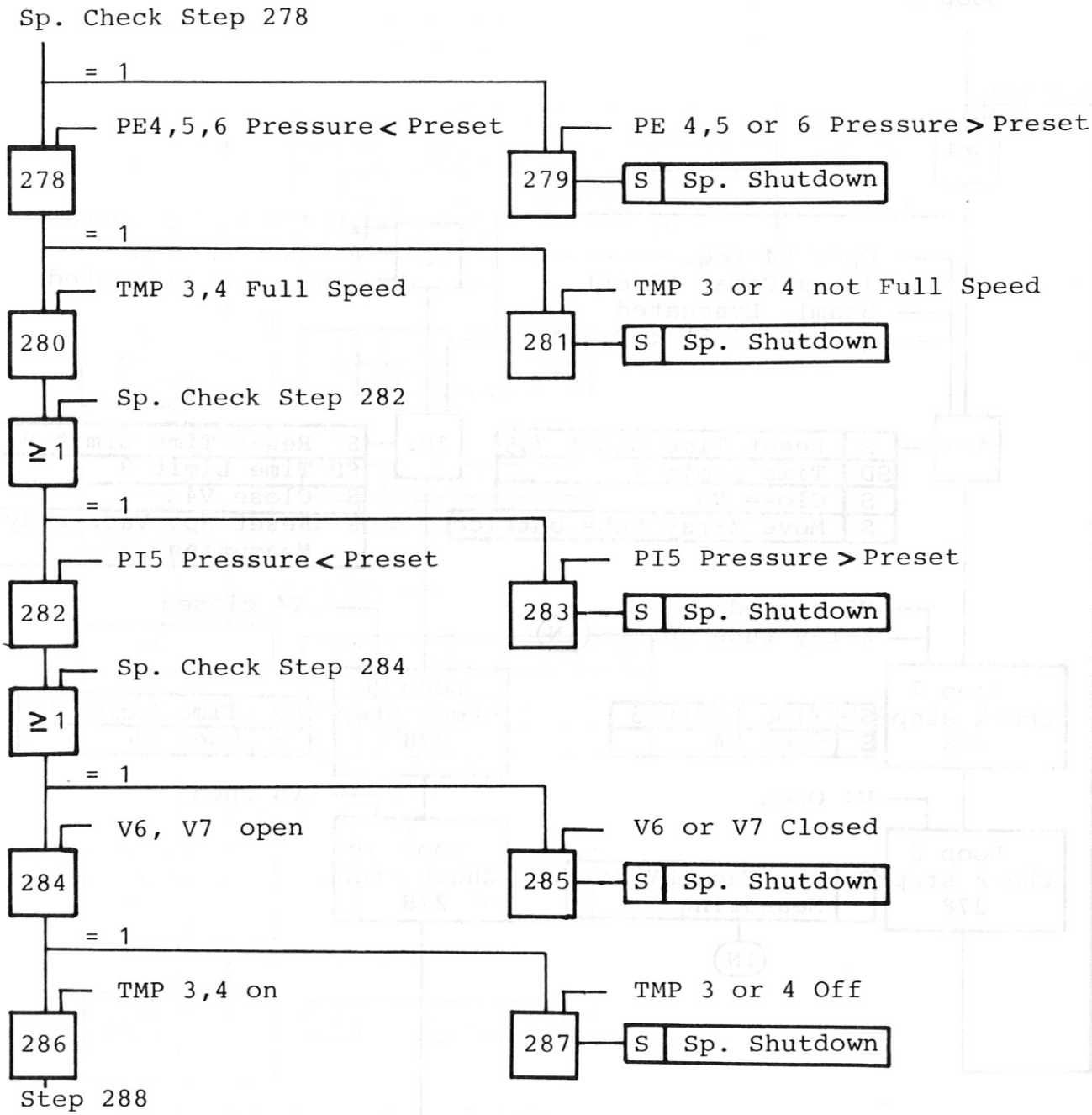

Fig. 34 /4

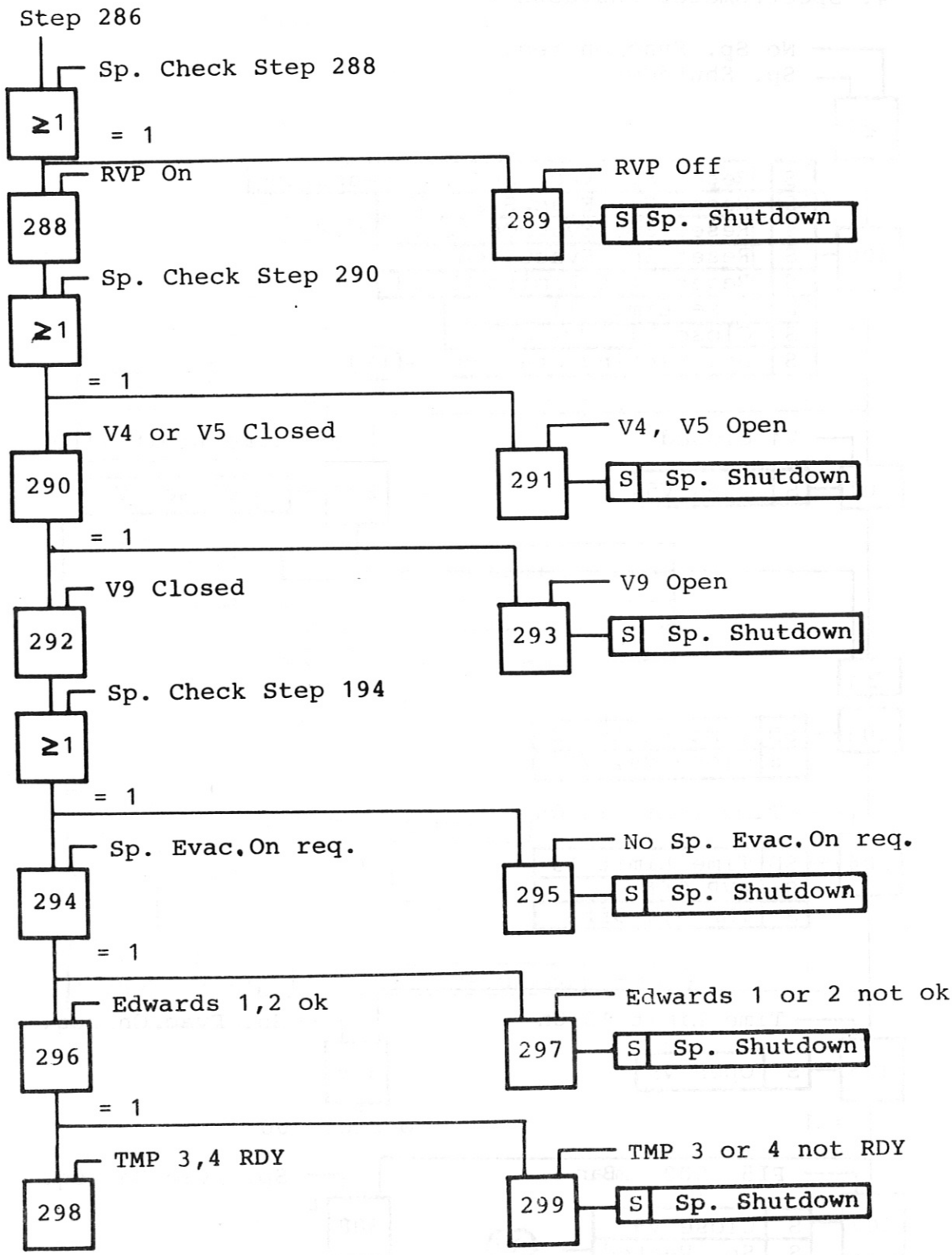
Step 286
Sp. Check Step 288
≥1
= 1
RVP On
288
RVP Off
289
S Sp. Shutdown
Sp. Check Step 290
≥1
= 1
V4 or V5 Closed
290
V4, V5 Open
291
S Sp. Shutdown
= 1
V9 Closed
292
V9 Open
293
S Sp. Shutdown
Sp. Check Step 194
≥1
= 1
Sp. Evac.On req.
294
No Sp. Evac.On req.
295
S Sp. Shutdown
= 1
Edwards 1,2 ok
296
Edwards 1 or 2 not ok
297
S Sp. Shutdown
= 1
TMP 3,4 RDY
298
TMP 3 or 4 not RDY
299
S Sp. Shutdown

Fig. 34 /5

4. Spectrometer Shutdown

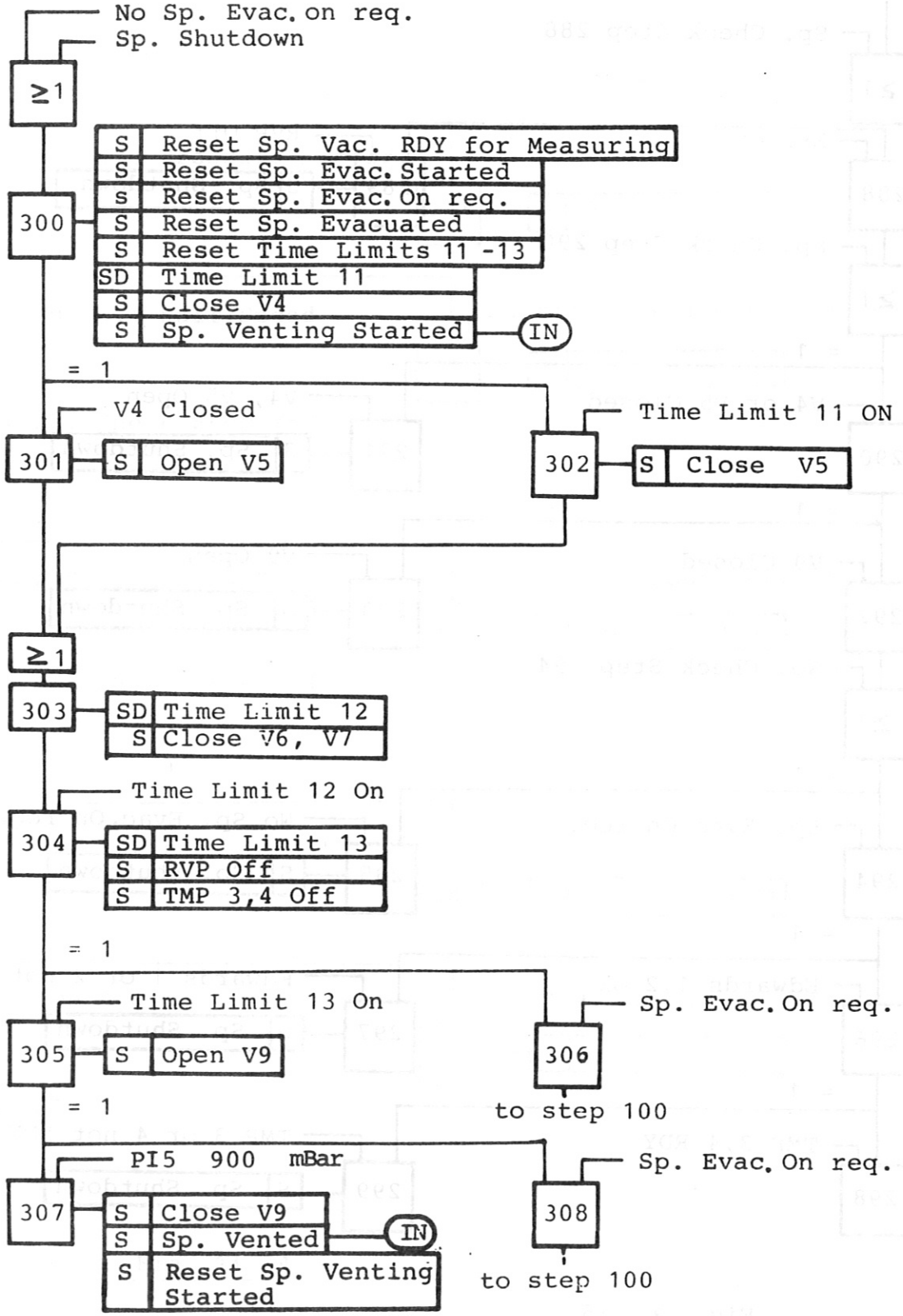

Fig. 34 /6

5. Beamline Evacuation

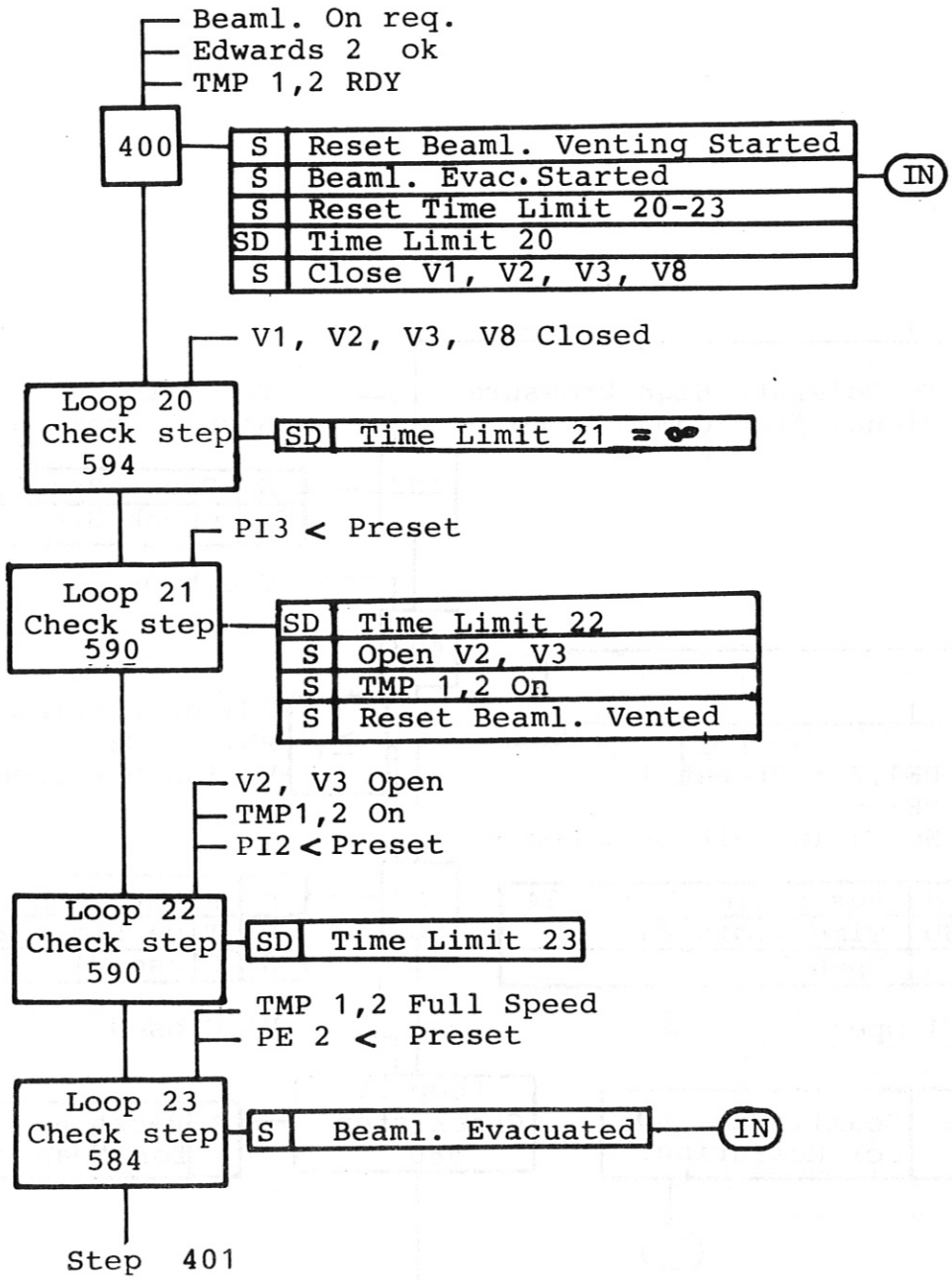

Fig. 34 /7

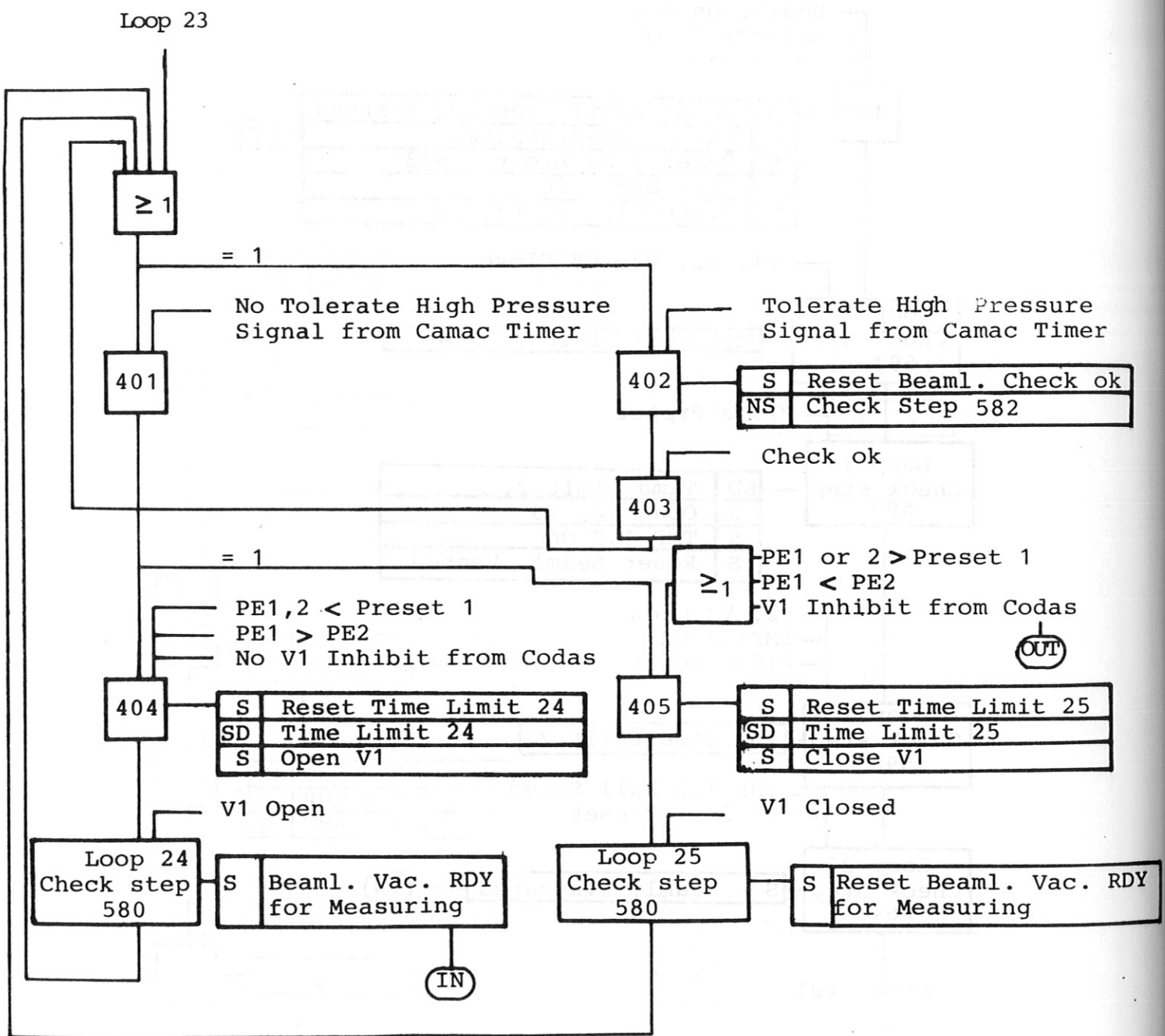
Loop 23
≥ 1
= 1
No Tolerate High Pressure Signal from Camac Timer
401
Tolerate High Pressure Signal from Camac Timer
402
S Reset Beaml. Check ok
NS Check Step 582
Check ok
403
= 1
≥1
PE1 or 2 > Preset 1
PE1 < PE2
V1 Inhibit from Codas
OUT
PE1,2 < Preset 1
PE1 > PE2
No V1 Inhibit from Codas
404
S Reset Time Limit 24
SD Time Limit 24
S Open V1
405
S Reset Time Limit 25
SD Time Limit 25
S Close V1
V1 Open
V1 Closed
Loop 24 Check step 580
S Beaml. Vac. RDY for Measuring
IN
Loop 25 Check step 580
S Reset Beaml. Vac. RDY for Measuring

Fig. 34 /8

6. Beamline Check

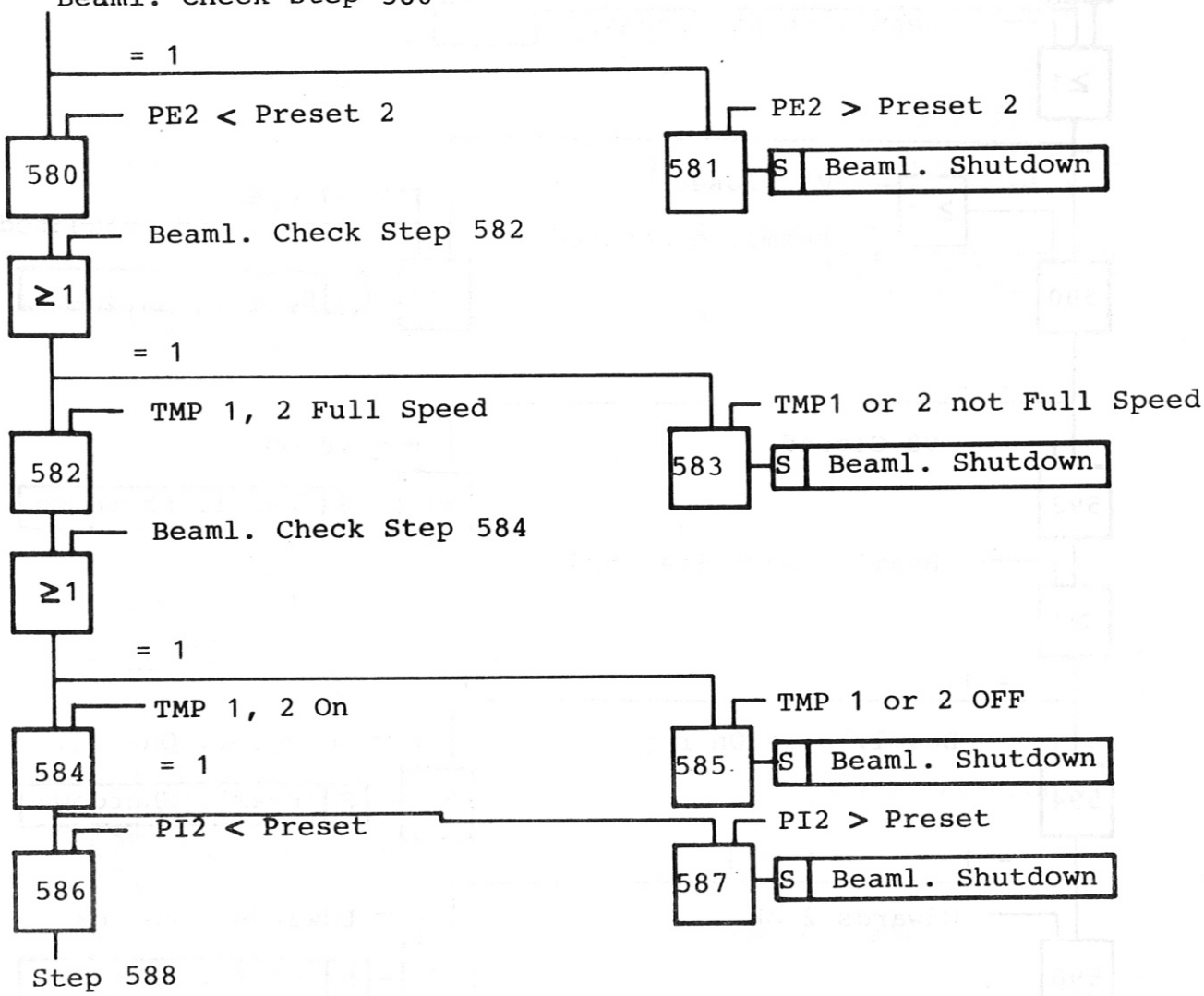

Fig. 34 /9

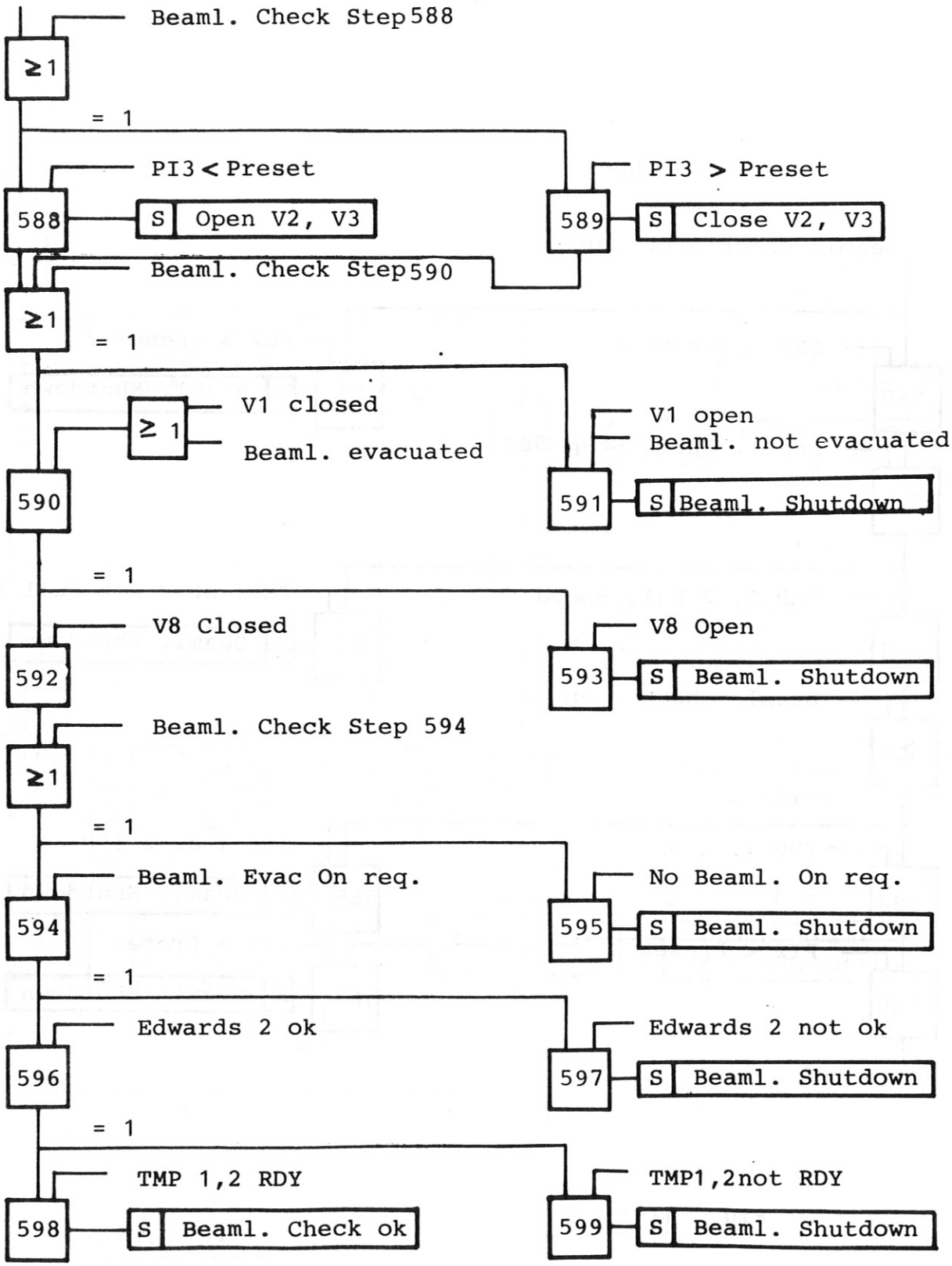
Step 586
Beaml. Check Step 588
≥1
= 1
PI3 < Preset
588
S Open V2, V3
PI3 > Preset
589
S Close V2, V3
Beaml. Check Step 590
≥1
= 1
≥ 1
V1 closed
Beaml. evacuated
590
V1 open
Beaml. not evacuated
591
S Beaml. Shutdown
= 1
V8 Closed
592
V8 Open
593
S Beaml. Shutdown
Beaml. Check Step 594
≥1
= 1
Beaml. Evac On req.
594
No Beaml. On req.
595
S Beaml. Shutdown
= 1
Edwards 2 ok
596
Edwards 2 not ok
597
S Beaml. Shutdown
= 1
TMP 1,2 RDY
598
S Beaml. Check ok
TMP1,2not RDY
599
S Beaml. Shutdown

Fig. 34 /10

7. Beamline Shutdown

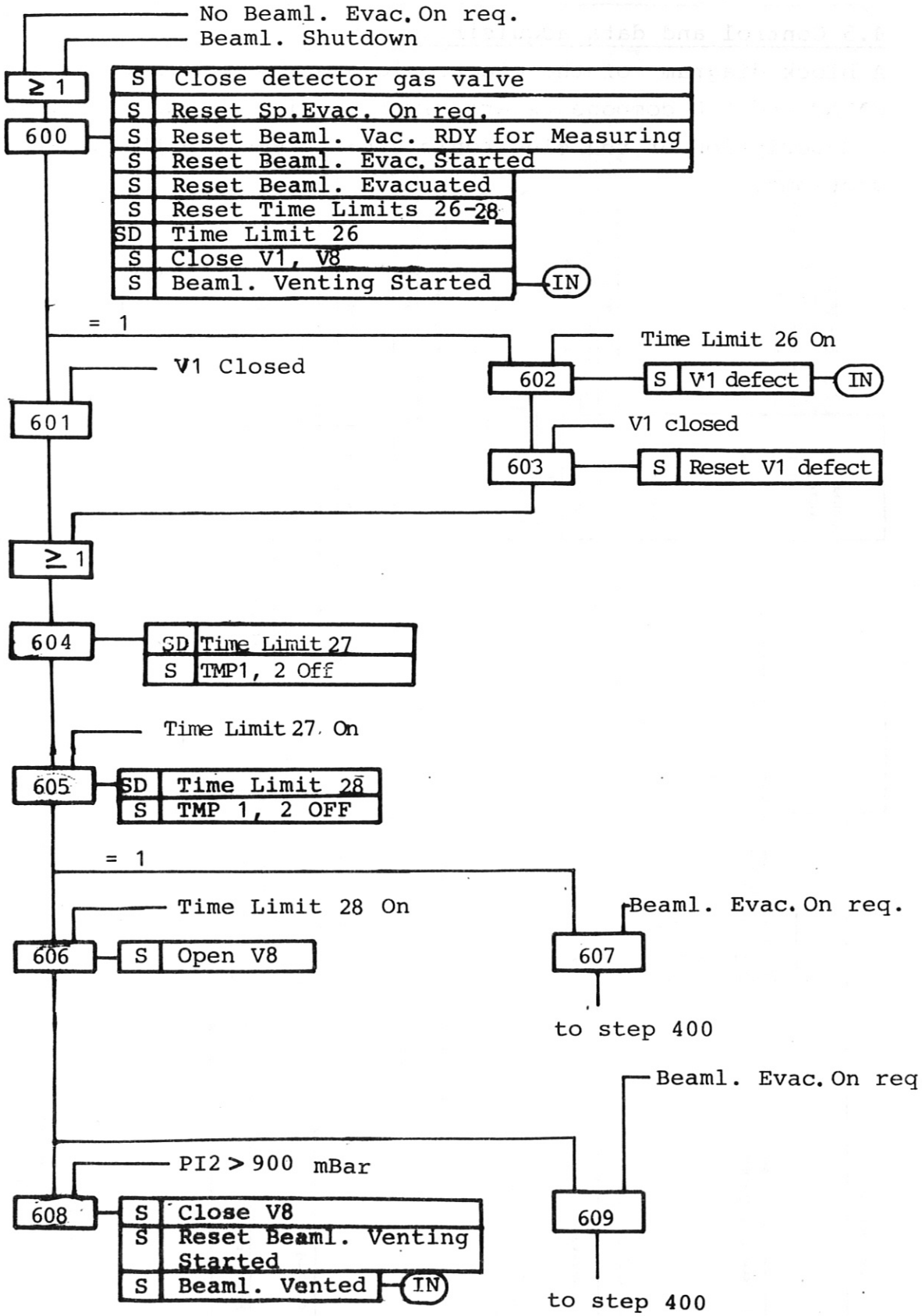

Fig. 34 /11

4.5 Control and data acquisition

A block diagram of the electronic systems and lists of the CAMAC and LSD components are given in Fig. 35 to 37 . For a description of the electronic sub-systems see the preceding sections.

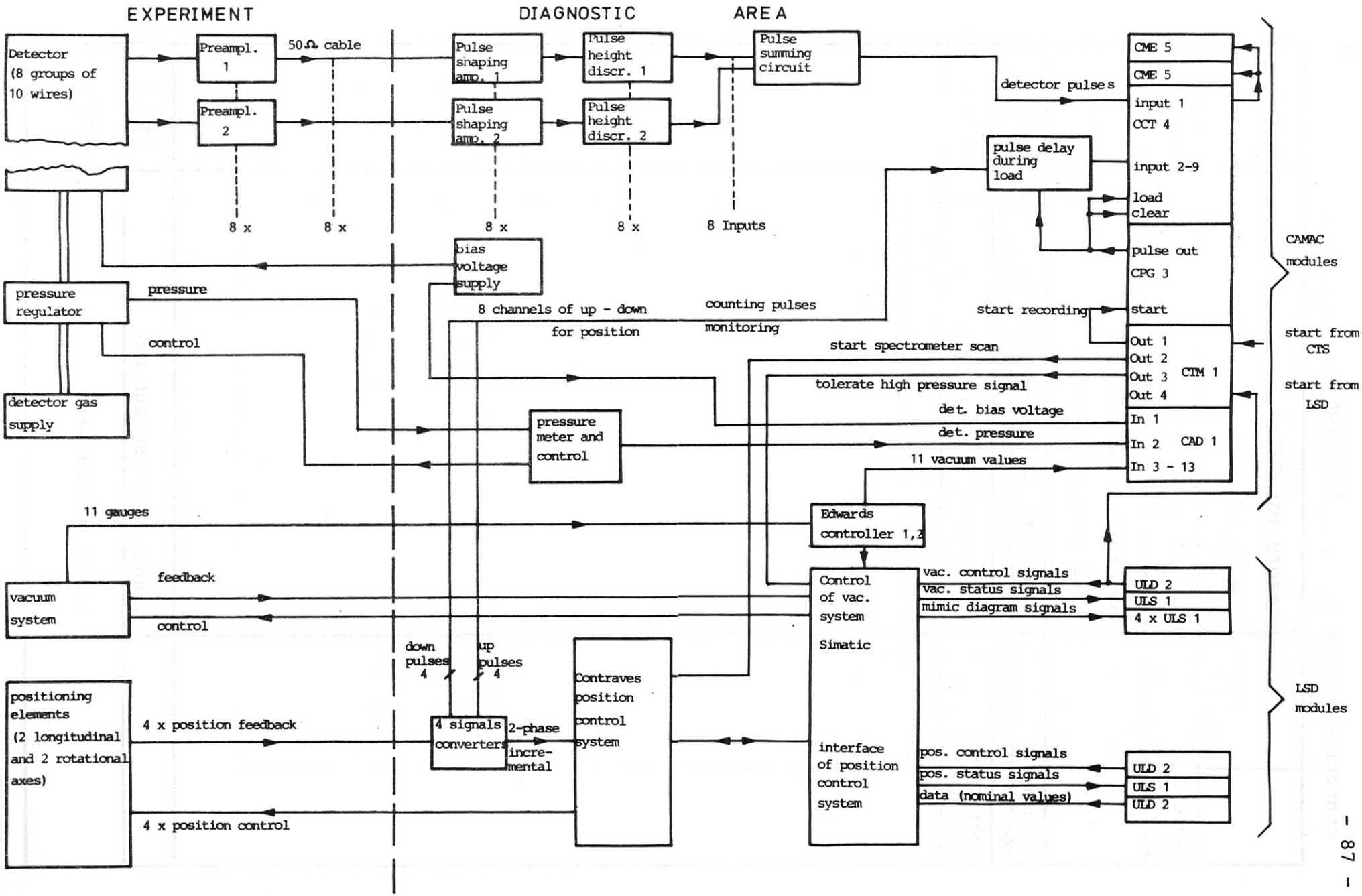

Fig. 35 Block diagram of the electronic systems

connected system	function	
	memory for CCT 4 (≈ 90 KWords)	CME 5
		CME 5
detector, positioning system	measure detector pulses, real positions	CCT 4
	generate a sequence of load pulses for CCT 4	CPG 3
vacuum and positioning system	timing of data acquisition, vacuum and positioning system	CTM 1
detector, vacuum system	monitor 13 analog values	CAD 1
	control of LSD subrack	CLS 2
	crate controller	CCC 2
		CCB 1

Fig. 36 Complement of CAMAC crate

vacuum control signals	ULD 2
vacuum status signals	ULS 1
mimic diagram signals	ULS 1
	ULS 1
	ULS 1
	ULS 1
position control signals	ULD 2
position status signals	ULS 1
nominal position values	ULD 2
connector card	ULC 1
Power supply	UPS 1

Fig. 37 Complement of LSD subrack

Acknowledgements

The authors acknowledge the continuous interest and help of Drs. W. Engelhardt, E. Källne, M. Kaufmann and G. Magyar. They thank C. Höss, Dr. K. Evans, Dr. G. Rupprecht,E.Pfeffermann,G.Schmitt and H. Hopper for support and help with the tests. They are especially indepted to Frau Chr. Röder, A. Nicol and S. Ertl for the preparation of this report.

References

/1/ C. Breton, C. DeMichelis, M. Finkenthal, M. Mattioli, "Ionization Equilibrium of Selected Elements from Neon to Tungsten of Interest in Tokamak Plasma Research", EUR-CEA-FC-948 (1978)

/2/ H.W. Drawin, "Plasma Impurities and Cooling", Atomic and Molecular Data for Fusion, IAEA-199, p. 217 (1977)

/3/ W. Engelhardt, J. Fink, G. Fußmann, H. Krause, H.-B. Schilling, U. Schumacher, MPI für Plasmaphysik Report IPP 1/212, IPP III/81 (March 1982)

/4/ S. von Goeler, M. Bitter, S. Cohen, D. Eames, K. Hill, D. Hillis, R. Hulse, G. Lenner, D. Manos, Ph. Roney, W. Roney, N. Sauthof, S. Sesnic, W. Stodiek, F. Tenney, J. Timberlake, Proc. Diagnostics for Fusion Reactor Conditions, Vol. I, EUR 8351-I EN (Varenna 1982), p. 109-127

/5/ B.C. Fawcett, Atomic Data and Nuclear Data Tables 30, 1-26 (1984)

/6/ A.J. Burek, Space Science Instrumentation 2, 53 (1976)

/7/ Z. Hussain, E. Umbach, D.A. Shirley, J. Stöhr, J. Feldhaus, Nucl. Instr. and Meth. 195, 115 (1982)

/8/ K. Kohra, M. Audo, T. Matsushita, H. Hashizume, Nucl. Instr. and Meth. 152, 161 (1978)

/9/ J.H. Beaumont and M. Hart, J. Phys. E:Scient. Instr. 7, 823 (1974)

/10/ B. Yaakobi, A.J. Burek, Laboratory of Laser Energetics Report No. 139, University of Rochester (January 1983)

/11/ M. Cantin, L. Koch-Miramond, B. Mougin, R. Roccia, Proc. Workshop on X-ray Astronomy in the 1980's, NASA Technical Memorandum 83848, p. 523 (Nov. 1981)

/12/ D.B. Brown, M. Fatemi, L.S. Birks, J. Appl. Phys. 45, 1555 (1974)

/13/ J.A. Bearden, A. Hening, Rev. Sci. Instr. 36, 334 (1965)

/14/ R. Bartiromo, R. Gianella, private communication

/15/ R.D. Deslattes, private communication

/16/ E. Lell, N.J. Kreidl, J.R. Hensler, in Progress in Ceramic Science, Vol. 4 (J.E. Burke, ed.), p. 3 (1966), Pergamon Press, Oxford

/17/ R. Jenkins, X-ray Spectr. 1, 23 (1972)

/18/ J. Stöhr, V. Rehn, I. Lindau, R.Z. Bachrach, Nucl. Instr. and Meth. 152, 43 (1978)

/19/ N.G. Alexandropoulos, G.G. Cohen, Appl. Spectroscopy 28, 155 (1974)

/20/ G. Materlik, private communication

/21/ L. Koch-Miramond, private communication

/22/ U. Bonse, I. Hartmann, Z.f.Kristallographie 156, 265 (1981)

/23/ A. Roth, Vacuum Technology, North-Holland Publishing Company 1976, p. 435

/24/ U. Hauser, W. Kerler, Rev. Sci.Instr. 29, 380 (1958)

/25/ H. Johnson, R. Deslattes, Rev. Sci.Instr. 36, 1310 (1965)

/26/ D. Christ, Dr. Rudolph and Prof. Schmal, private communication

/27/ E.Pfeffermann, U. Briel, Adv. Space Res. 2, 255 (1983)

/28/ F. Briggs, R. Lighthill, Report Sandia SC-RR-7105707, Albuquerque/USA (1971)

/29/ G. Charpak, R. Bouclier, T. Bressani, J. Favier, C. Zupancic, Nucl. Instr. Meth. 62, 262 (1968)

/30/ F. Sauli, "Principles of operation of Multiwire Proportional and Drift Chambers", Report CERN 77-09, Geneva 1977

/31/ R.A. Boie, J. Fischer, Y. Inagaki, F.C. Merritt, V. Radeka, L.D. Rogers, D.M. Xi, Nucl. Instr. Meth. 201, 93 (1982)

/32/ J. Källne, E. Källne, L.G. Acentio, C.L. Morris, A.C. Thompson, Nucl. Instr. Meth. 203, 415 (1982)

/33/ R.L. Blake, private communication

/34/ H. Bradt et al., Space Sci. Rev. 8, 471 (1968)

/35/ D.L. McKenzie, P.B. Landecker, J.H. Underwood, Space Science Instrumentation 2, 125 (1976)

List of drawings (handed over to JET)

Drawing No.	
PH 500 020	Layout drawing
PH 500 021	Cross-section of module I
PH 500 025	Cross-section of track
PH 500 023	Motion feed-through for collimator
PH 500 022	Tee with drive for X-ray tube
PH 500 024	Adjustable bearing supports for track
PH 500 027	Positioning control for double-crystal spectrometer
PH 500 028	Vacuum system
PH 500 030	Front panel vacuum system
PH 500 029	Block diagram